Quantum Monte Carlo study of van der Waals systems

Yassmin Hassn A Asiri

Department of Physics

Lancaster University

This thesis is submitted for the degree of

Doctor of Philosophy

December, 2022

Dedicated to the memory of my grandfather.

Abstract

In this thesis, we develop a new method to account for the vibrational renormalisation of electronic structure by both thermal and quantum lattice vibrational effects. Atomic configurations are randomly sampled based on quasiharmonic phonon calculations within density functional theory, and the excitation energy at each configuration is evaluated using fixed-node diffusion quantum Monte Carlo. We demonstrate that the developed technique is efficient and has the potential to be applied to a wide range of materials. We report the zero-point renormalisation of the band gap for benzene, monolayer and bulk hBN, bulk Si and C-diamond. The proposed approach within quantum Monte Carlo is found to be sufficient to capture the quantum effect of zero-point motion and improve the agreement with experiment gap results. We also investigate the temperature-dependent renormalisation of the direct band gap of benzene, bulk Si, and C-diamond arising from harmonic vibrational effects within density functional theory. We study an impurity of a single hole in ideal, dilute weakly doped 2D homogeneous electron gas modelling a van der Waals heterostructure of a $MoSe_2$ monolayer embedded in flakes of hBN. This allows us to investigate the effect of a finite concentration of charge carriers that interact via a periodic Keldysh interaction on the formation of a negative trion. The quantum Monte Carlo results of relaxation energies and pair correlation functions at a range of low densities are reported. Our results indicate that the screening effects of the surrounding electron gas on the formation of a negative trion are weak. We perform ab initio calculations of the defect formation energy for silicon substitution and Stone–Wales defects in monolayer graphene and the atomisation energy of bulk silicon, with the aim of benchmarking the accuracy of the widely used density functional theory method in these types of calculations. Our results show that the density functional theory significantly underestimates the defect formation energy and overestimates the atomisation energy of bulk silicon.

Declaration

This thesis describes work carried out between October 2018 and October 2022 in the Condensed Matter group at the Department of Physics, Lancaster University under the supervision of Dr. N. D. Drummond. The following section of this thesis are included in work that has been published or to be submitted:

Chapter 2,3: Y.Asiri and N. D. Drummond, "Vibrational renormalisation of quantum Monte Carlo band gaps via random sampling of normal coordinates," in preparation.

Chapter 4: Y.Asiri and N. D. Drummond, "Quantum Monte Carlo study of trion formation in weakly doped monolayer $MoSe_2$ encapsulated by hBN," in preparation.

Chapter 5: D. M. Thomas, Y. Asiri, and N. D. Drummond, "Point defect formation energies in graphene from diffusion quantum Monte Carlo and density functional theory," *Phys. Rev. B,* vol. 105, p. 184114, May 2022.

I declare that this thesis is my own work, and has not been submitted in substantially the same form for the award of a higher degree elsewhere. This thesis does not exceed the word limit of 80,000 words.

Yassmin Hassn A Asiri

Lancaster, October 2022

Acknowledgements

I would first like to thank my supervisor Neil Drummond for all his advice and support during my PhD. I am sincerely grateful to him for all of the guidance and support that he has given me. I would also like to thank David Thomas, Ryan Hunt, and the rest of the Condensed Matter theory group for their collaborations and discussions.

In addition, I would like to thank my loving and caring husband, Ahmed Almusaeudi, for all his support and endless love. My thanks also go to my family especially my parents for their encouragement and support throughout my life, without which I would not be where I am today.

This work has been financially supported by the Saudi Arabian Cultural Bureau (SACB) and King Khalid University. Computational facilities have been provided by the Lancaster High End Computing (HEC) cluster, the ARCHER UK National Supercomputing Service, and by the Cambridge Service for Data Driven Discovery (CSD3).

Contents

List of Figures

List of Tables

Chapter 1

Introduction

1.1 Electronic structure calculations

1.1.1 Many-particle Schrödinger equation

In the last few decades, many theoretical studies using first-principles (*ab initio*) methods have enhanced our understanding of the various physical properties of a broad range of quantum systems and the qualitative and quantitative behaviour of electrons in condensed matter. In order to study the electronic structure properties of materials it is important to solve accurately the many-body Schrödinger equation. However, finding an exact solution to the Schrödinger equation remains the greatest challenge for electronic-structure methods that grow exponentially with the system size. Although an exact solution to the Schrödinger equation is only available for the smallest system sizes, there are a wide range of approximate methods useful for examining systems with a larger number of electrons. All results and equations are expressed in Hartree atomic units ($\hbar = |e| = m_e = 4\pi\epsilon = 1$) unless otherwise specified.

In a non-relativistic quantum system, the dynamics of the particles are governed by the time-dependent Schrödinger equation, which is given by

$$i\frac{\partial}{\partial t}\Psi(\{\mathbf{r}_i\},\{\mathbf{R}_I\},t) = \hat{H}\Psi(\{\mathbf{r}_i\},\{\mathbf{R}_I\},t), \tag{1.1}$$

where the wave function $\Psi(\{\mathbf{r}_i\},\{\mathbf{R}_I\},t)$ contains all the information specifying the state of the system; $\mathbf{r}_i$ is the coordinate of electron i and $\mathbf{R}_I$ is the coordinate of

nucleus I. The wave function must be antisymmetric in the coordinates of the same-spin electrons to satisfy the Pauli exclusion principle.

The non-relativistic Hamiltonian $\hat{H}$ for a system containing N electrons and M nuclei is given by,

$$\begin{aligned} \hat{H} &= \hat{T}_e + \hat{T}_p + \hat{V}_{ep} + \hat{V}_{ee} + \hat{V}_{pp} \\ &= -\frac{1}{2}\sum_{i=1}^{N}\nabla_i^2 - \frac{1}{2}\sum_{I=1}^{M}\frac{\nabla_I^2}{m_I} - \sum_{i=1}^{N}\sum_{I=1}^{M}\frac{Z_I}{r_{iI}} + \sum_{i<j}^{N}\frac{1}{r_{ij}} + \sum_{I<J}^{M}\frac{Z_I Z_J}{r_{IJ}}\,, \end{aligned} \tag{1.2}$$

where Z and m are the atomic number and the nuclear mass, respectively, and r is the separation, where i, j and I, J refer to electrons and nuclei, respectively. The first two terms are the electron and nuclear kinetic energies respectively; the third term is the electron–nucleus interaction; and the two remaining terms represent the electron–electron and nucleus–nucleus interactions. Equations (1.1) and (1.2) have a large number of degrees of freedom. Hence, solving the Schrödinger equation exactly for any realistic system is generally impossible, and to tackle this problem approximations are needed. Various numerical approaches for solving the Schrödinger equation have been developed, and an overview of some of them is presented in Sec. 1.2

1.1.2 Born-Oppenheimer approximation

The adiabatic or Born-Oppenheimer (BO) approximation [7] allows simplification of the many-body Schrödinger equation. As nuclear masses are substantially heavier than electron masses, the nuclei are relatively slow, thereby allowing decoupling of the electronic motion from the nuclear motion. Thus, the wave function can be written as a product of an electronic and a nuclear wave function. Since the electrons move instantaneously in response to the nuclei, the electronic eigenfunction can be written parametrically in terms of the nuclear position, and the time-dependence of the electronic wave function can be ignored. Under these assumptions, the wave function of a stationary state can be obtained by solving the non-relativistic time-independent electronic Schrödinger equation, which is given by

$$\hat{H}_{\text{el}}\Psi_n(\mathbf{R}) = E_n(\mathbf{R})\Psi_n(\mathbf{R}) \tag{1.3}$$

where E_n and $\Psi_n(\mathbf{R})$ are the energy eigenvalues and eigenfunctions, respectively, of the electronic Hamiltonian $\hat{H}_{\text{el}}$. The $3N$-dimensional vector $\mathbf{R} = (\mathbf{r}_1, \mathbf{r}_2, ..., \mathbf{r}_N)$ denotes the coordinates of all the electrons. The ground-state is a stationary state with the lowest energy that can be determined via the variational principle, by minimising the total energy with respect to all possible variations in $\Psi(\mathbf{R})$. Therefore, the electrons remain in their instantaneous ground-state for any ionic configuration [8], and we only consider the energy associated with the electronic ground-state. The non-relativistic BO Hamiltonian for the electronic degrees of freedom is

$$\hat{H}_{\text{el}} = -\frac{1}{2}\sum_{i=1}^{N}\nabla_i^2 + \frac{1}{2}\sum_{i\neq j}^{N}\frac{1}{r_{ij}} - \sum_{i=1}^{N}\sum_{I=1}^{M}\frac{Z_I}{r_{iI}} + E_I\,, \tag{1.4}$$

where E_I is the nucleus–nucleus interaction term that contributes to the total energy of the system as a constant offset. A complete quantum description of the nuclei motion can be included by solving the Schrödinger equation for the nuclei, which is an important many-body problem. The fundamental form of the nuclear Hamiltonian can be written as

$$\hat{H}_{\text{vib}} = \sum_{R_l,\kappa} -\frac{1}{2m_\kappa}\nabla_{l\kappa}^2 + E_n(\mathbf{R}), \tag{1.5}$$

where κ denotes the different atoms within a primitive unite cell, m_κ is the mass of atom κ, $\mathbf{R}_l$ denotes the position vectors of the unit cell and $E_n(\mathbf{R})$ is known as the 'BO energy surface'. More details are given in Chapter 2.

1.2 Electronic structure methods

1.2.1 Hartree-Fock (HF) theory

The HF approximation [9, 10] is an important starting point for many modern methods of performing electronic structure calculations. The HF theory was developed to approximately solve the electronic Schrödinger equation Eq. (1.3).

For an N-electron system, the many-electron wave function is an antisymmetric function under particle exchange formed by a single determinant made up of any choice of single-electron spin orbital ϕ_i known as a 'Slater determinant'. The function

is denoted as

$$\Psi_S(\mathbf{X}) = \frac{1}{\sqrt{N!}} \begin{vmatrix} \phi_1(\mathbf{x}_1) & \phi_1(\mathbf{x}_2) & \dots & \phi_1(\mathbf{x}_N) \\ \phi_2(\mathbf{x}_1) & \phi_2(\mathbf{x}_2) & \dots & \phi_2(\mathbf{x}_N) \\ \vdots & \vdots & \ddots & \vdots \\ \phi_N(\mathbf{x}_1) & \phi_N(\mathbf{x}_2) & \dots & \phi_N(\mathbf{x}_N) \end{vmatrix}, \tag{1.6}$$

where $\mathbf{X} = (\mathbf{x}_1, \mathbf{x}_2, ..., \mathbf{x}_N)$, $\mathbf{x}_i = \{\mathbf{r}_i, \sigma_i\}$ denotes the spatial-spin coordinates of electron i and $(N!)^{-1/2}$ is a normalisation factor. The antisymmetric property ensures that the Slater determinant vanishes when two same-spin electrons coincide and that the Pauli exclusion principle will be satisfied. It also implies that each electron moves independently in an effective potential that feels the average effect of other electrons via the repulsive Coulomb interactions and the exchange interaction. The exchange interaction effects arise due to the antisymmetric form of the wave function. This description does not account for any correlation between electrons that will result in electrons avoiding each other, which is often referred to as the 'independent particle theory' or 'mean-field theory'. Within the variational principle, one can obtain a numerical approximation of Eq. (1.3) by minimising the HF energy with respect to changes in the orbitals' parameters, as follows:

$$\langle \Psi_S | \hat{H} | \Psi_S \rangle \geq E_0, \tag{1.7}$$

where E_0 is the exact ground-state energy. The derived HF equations are eigenvalue equations that can be solved using initial orbitals with the constraint that the single-electron spin orbitals remain orthonormal, $\langle \phi_i | \phi_j \rangle = \delta_{ij}$, and then refined iteratively until self-consistency is reached. Because of this, it is called the 'self-consistent field (SCF) method'.

1.2.2 Beyond Hartree-Fock

In general, the HF theory accounts for the exchange effects of the antisymmetric wave function but overlooks the electronic correlations resulting from the electron–electron Coulomb interaction. Due to the absence of electronic correlation effects, the HF method significantly overestimates the gap between the occupied and unoccupied states. Although correlation effects account for a small fraction of the total energy, they are important. Electronic correlation effects can be included

by using post–HF methods in quantum chemistry. These methods construct a more complicated many-electron wave function using a linear combination of determinants, thus forming the so-called 'multi-determinant wave function'. This provides significant further variational freedom in the wave function for a given system size and can recover a large fraction of the correlation energy [9, 10]. However, the main problem with such expansions is that the number of required determinants grows very rapidly with the system size, making it difficult to achieve comparable accuracy in different systems and in different system sizes. For example, the CISD (configuration interaction singles and doubles excited method), scales with system size as $O(N^6)$ [11], where N is the particle number. Similarly, the coupled cluster with single, double and perturbative triples (CCSD(T)) method is an accurate method but computationally expensive.

1.2.3 Density functional theory

The density functional theory [12, 13] (DFT) is a theory that pertains to correlated many-body systems. DFT allows replacement of the complicated N-electron wave function and the associated Schrödinger equation with the much simpler electron density $n(\mathbf{r})$ and its associated calculational scheme. It was first proposed by Hohenberg and Kohn (1964), [14] who stated that all properties of a many-body system are uniquely determined as functionals of the ground-state electronic density $n_0(\mathbf{r})$ that is uniquely defined by the external potential v_{ext}. For a know $n_0(\mathbf{r})$, the Hamiltonian and hence the wave functions and ultimately all properties of the system are uniquely determined by $n_0(\mathbf{r})$.

The Hamiltonian of the interacting electron system in an external potential v_{ext} in which the electrons move

$$\begin{aligned} \hat{H} &= -\frac{1}{2}\sum_i \nabla_i^2 + \sum_i v_{\text{ext}}(\mathbf{r}_i) + \frac{1}{2}\sum_{i\neq j}\frac{1}{r_{ij}}\,, \\ &= \hat{T} + \hat{V}_{\text{ext}} + \hat{V}_{ee} \end{aligned} \tag{1.8}$$

The unique ground-state wave function ψ that has a global minimum value of energy E is determined by solving the Schrödinger equation with this Hamiltonian. Within the variational principle, the ground-state energy can be obtained by minimising the total energy of the system $E[n(\mathbf{r})]$ with respect to variations in the density function

$n(\mathbf{r})$ under the constraint that the number of electrons be kept fixed, as follows:

$$\int n(\mathbf{r})d\mathbf{r} = N. \tag{1.9}$$

For a given external potential determined by $n(\mathbf{r})$, the total energy as a function of $n(\mathbf{r})$ is

$$\begin{aligned} E_{\mathrm{HK}}[n(\mathbf{r})] &= \langle\psi|\hat{T} + \hat{V}_{ee}|\psi\rangle + \langle\psi|\hat{V}_{\mathrm{ext}}|\psi\rangle \\ &= F_{\mathrm{HK}}[n(\mathbf{r})] + \int v_{ext}(\mathbf{r})\, n(\mathbf{r})d^3\mathbf{r}, \end{aligned} \tag{1.10}$$

where ψ is the ground-state wave function uniquely determined by ground-state charge density $n(\mathbf{r})$ via the external potential determined by $n(\mathbf{r})$. $F_{\mathrm{HK}}[n(\mathbf{r})]$ is a universal function of the density, which includes all internal energies, namely, kinetic and potential energies. If the obtained density function $n(\mathbf{r})$ is exact, the evaluated energy E is the exact ground-state energy. However, there are two main problems. First, $F_{\mathrm{HK}}[n(\mathbf{r})]$ is universal to all systems, and its exact form is unknown. Second, there are no known formulas for calculating the wave function directly from the density.

1.2.3.1 Kohn-Sham equations

The Kohn-Sham (KS) scheme [15] provides a practical way of implementing the density-functional theory, which has become the basis of many of the current methods of treating electrons in real systems. The basic idea of the KS formalism is to replace the complicated interacting many-body system that obeys the Hamiltonian Eq. (1.2) with a simpler non-interacting auxiliary system with N independent single-particle equations that can be solved more easily, with the same ground state density as the exact system.

Due to their non-interacting nature, the independent-particle wave functions can be expressed as a Slater determinant of a set of single-particle orbitals $\phi_i(\mathbf{r})$, which are defined in Eq. (1.6). In this formula, the electronic density is written in terms of N orthonormal orbitals:

$$n = \sum_{i}^{N} |\phi_i(\mathbf{r})|^2 . \tag{1.11}$$

The independent-particle kinetic energy T_s is given as a functional of the orbitals as follows:

$$T_s[n(\mathbf{r})] = -\frac{1}{2}\sum_{i=1}^{N}\langle\phi_i|\nabla_i^2|\phi_i\rangle\ . \tag{1.12}$$

The long-range Hartree energy or the electrostatic potential energy is

$$E_{\mathrm{H}}[n(\mathbf{r})] = \frac{1}{2}\int\int\frac{n(\mathbf{r})n(\mathbf{r}')}{|\mathbf{r}-\mathbf{r}'|}d\mathbf{r}d\mathbf{r}', \tag{1.13}$$

The KS energy functional E_{KS} is defined by rewriting the Hohenberg-Kohn expression for the ground-state energy functional as

$$E_{\mathrm{KS}}[n(\mathbf{r})] = T_s[n(\mathbf{r})] + E_{\mathrm{H}}[n(\mathbf{r})] + \int V_{\mathrm{ext}}(\mathbf{r})n(\mathbf{r})d\mathbf{r} + E_{\mathrm{XC}}[n(\mathbf{r})], \tag{1.14}$$

where V_{ext} is the external potential due to the nuclei and any other external fields and the exchange-correlation energy $E_{\mathrm{XC}}[n(\mathbf{r})]$ includes all the many-body exchange and correlation interaction effects and is explicitly modelled as a density functional. The KS auxiliary system for the ground state can be solved by minimising the energy in Eq. (1.14) with respect to the orbitals ϕ_i that define the density $n(\mathbf{r})$. This leads to the following set of single-electron equations called the KS Schrödinger equations:

$$\hat{H}_{\mathrm{KS}}\phi_i(\mathbf{r}) = \epsilon_i\phi_i(\mathbf{r}), \tag{1.15}$$

where ϵ_i denotes the eigenvalues and $\hat{H}_{\mathrm{KS}}$ is the effective Hamiltonian computed as

$$\hat{H}_{\mathrm{KS}} = -\frac{1}{2}\nabla^2 + V_{\mathrm{KS}}(\mathbf{r}), \tag{1.16}$$

with an effective potential V_{KS} also known as a 'self-consistent field' that is obtained using the variation of the energy functional Eq. (1.14) with respect to $n(\mathbf{r})$ under the condition in Eq. (1.9).

$$\begin{aligned} V_{\mathrm{KS}}(\mathbf{r}) &= V_{\mathrm{ext}}(\mathbf{r}) + \frac{\delta E_{\mathrm{H}}}{\delta n(\mathbf{r})} + \frac{\delta E_{\mathrm{XC}}}{\delta n(\mathbf{r})} \\ &= V_{\mathrm{ext}}(\mathbf{r}) + V_{\mathrm{H}}(\mathbf{r}) + V_{\mathrm{XC}}(\mathbf{r}) \end{aligned} \tag{1.17}$$

The KS potential V_{KS}, given by Eq. (1.17), depends on the electron density $n(\mathbf{r})$, but $n(\mathbf{r})$ depends on the KS eigenstates $\phi_i(\mathbf{r})$. Therefore, Eq. (1.15) with a potential Eq. (1.17) must be solved self-consistently with the resulting density. Once the DFT computations have reached convergence, the KS many-body wave function can be constructed as a compact single Slater determinant of KS single-particle orbitals, as shown in Eq. (1.6).

1.2.3.2 Local-density approximation and beyond

The most challenging part of DFT is constructing functionals that correctly describe the exchange and correlation effects. The exact form of $E_{\mathrm{XC}}[n(\mathbf{r})]$ can be reasonably approximated as a density functional. The simplest (non-trivial) approximation is local-density approximation (LDA), proposed by Kohn and Sham [15]. In this approximation, the general inhomogeneous electron system is considered locally homogeneous and has the same exchange-correlation (XC) energy as an equivalent volume of a homogeneous electron gas (HEG) with the same density. The LDA exchange-correlation functional reads:

$$E_{\mathrm{XC}}^{LDA}[n(\mathbf{r})] = \int n(\mathbf{r})\epsilon_{\mathrm{XC}}^{LDA}[n(\mathbf{r})]\, d^3\mathbf{r}, \tag{1.18}$$

where $\epsilon_{\mathrm{XC}}^{LDA}$ is the XC energy per electron of HEG at density n. This functional has yielded impressively good results for a wide variety of materials, especially for weakly correlated materials, such as simple metals and semiconductors [16]. However, it fails in many situations due to its inability to describe non-local exchange and correlation effects in van der Waals systems, inhomogeneities of density in weak inter-molecular bonds, strong local correlation in strongly correlated systems, and band gap energies [10].

Attempts to improve the LDA functional have been somewhat successful. Generalised gradient approximations (GGA), such as the PBE (Perdew-Burke-Ernzerhof) functional [17], are currently the most popular functionals that introduce the non-locality of density. In this class of approximation, the XC functional involves an expansion of the electron density in terms of the gradient that describes the spatial inhomogeneity of the density. More accurate available approximations are the hybrid functionals such as B3LYP (Becke, 3-parameter, Lee-Yang-Parr) [18, 19]. The XC functionals are built as a combination of the exact exchange term from Hartree-Fock theory and a density functional.

Unfortunately, the DFT method with local and semi-local exchange-correlation functionals fails to describe the nonlocal, weak interatomic van der Waals (vdW) interactions. The vdW interactions are caused by the electrostatic interaction of atomic dipolar fluctuations, which tend to the classical dipole-dipole interaction $(1/r^6)$ at long-range distances. These interactions play a crucial role in determining

the structure, stability and function of a vast range of materials. Therefore, an accurate description of vdW interactions is necessary for advancing our knowledge of several areas of chemistry, biology and condensed matter. Improvements for the GGA and hybrid DFT exchange-correlation functionals have been proposed to approximately describe the long-range vdW interaction [20, 21]. Using the Tkatchenko-Scheffler (TS) vdW technique [22], which computes the vdW energy corrections from the ground-state electron density of a molecule or solid and reference values for the free atoms, an accurate determination of long-range vdW interaction may be obtained. Further development of the TS-vdW scheme was achieved by including the long-range screening effects of vdW interactions using pairwise self-consistent-screening energy [23]. In general, having access to reliable benchmark data for vdW bonded systems is essential for the development of vdW correction techniques for DFT. Such benchmark data can be gathered via QMC methods.

1.2.4 Quantum Monte Carlo methods

Quantum Monte Carlo (QMC) simulation is a powerful stochastic electronic-structure technique that is capable of providing a direct and highly accurate treatment of electron correlation and of stochastically solving the many-body Schrödinger equation. Its establishment opened the possibility of dealing with larger systems with several hundreds of electrons. QMC methods can be applied to a wide variety of systems and are capable of accurately evaluating many properties. Several types of QMC methods have been applied to problems in solid-state physics in recent years, but in this thesis, for continuum models of electrons in solids, we use variational quantum Monte Carlo (VMC) and diffusion quantum Monte Carlo (DMC) [24, 25]. Both VMC and DMC are variational methods, as the evaluated energy is an upper bounds on the exact ground–state energy. The VMC and DMC methods have the advantage of having a zero–variance feature: whenever the trial wave function is the exact eigenstate the statistical fluctuations in the estimated energy reduce to zero and the evaluated energy is the true eigenvalue. Another attractive feature is that the fixed-node DMC method is not affected by finite basis set errors and depends only on the nodal surface of the trial wave function [26].

These methods are intrinsically parallel without loss of efficiency and scale as the third power of the system size $O(N^3)$, which is highly favourable in contrast to other correlated wave-function methods [24]. The CASINO software package [25] was used for all QMC calculations reported in this thesis.

1.2.4.1 Monte Carlo integration

Monte Carlo (MC) integration is a more efficient method of evaluating the high-dimensional integrals encountered in realistic electronic structure calculations than conventional quadrature methods such as Simpson's rule. The estimated error in the evaluation of high d-dimensional integral using Simpson's rule poorly scales with integer dimensionality as $M^{-4/d}$, where M is the number of sampling points within the integration region. In contrast, the estimated errors in MC integration show the scaling of $M^{-1/2}$. Consider a definite integral of the form

$$I = \int_{\Omega} g(\mathbf{R}) d\mathbf{R}, \tag{1.19}$$

where $\mathbf{R}$ is a multi-dimensional vector, Ω is the region of configuration space in which we are interested and $g(\mathbf{R})$ is a non-trivial multidimensional function.

In general, suppose we have a defined function $\omega(\mathbf{R}) \approx |g(\mathbf{R})|$ in region Ω and a positive normalised function $P(\mathbf{R})$,

$$P(\mathbf{R}) = \frac{w(\mathbf{R})}{\int w(\mathbf{R})\, d\mathbf{R}}\,, \tag{1.20}$$

where $P(\mathbf{R})$ is a probability density function. The MC integration of Eq. (1.19) is then carried out by decomposing $g(\mathbf{R})$ into a product of two functions,

$$I = \int_{\Omega} g(\mathbf{R}) d\mathbf{R} = \int f(\mathbf{R}) P(\mathbf{R}) d\mathbf{R}, \tag{1.21}$$

where $f(\mathbf{R})$ is the real function that can be evaluated in Ω. This method is called the importance sampling transformation method because $f(\mathbf{R})$ is averaged over a set of sampling points that are chosen by probability $P(\mathbf{R})$. Therefore, the integral I can be evaluated by the average $f(\mathbf{R})$ over a large but finite M uncorrelated random vectors $\mathbf{R}_i$ distributed according to $P(\mathbf{R})$ as

$$I \approx \frac{1}{M} \sum_{i=1}^{M} f(\mathbf{R}_i) = \langle f \rangle. \tag{1.22}$$

The rewriting of the integral I in the form of Eq. (1.22) substantially reduces the fluctuations in $f(\mathbf{R}) = g(\mathbf{R})/P(\mathbf{R})$ compared to those initially contained in $g(\mathbf{R})$, which increases the efficiency of the MC integration by sampling more frequently from the region where the integrand is large. The standard error bar of the estimate value I is $\pm\frac{\sigma}{\sqrt{M}}$, and the variance is

$$\begin{aligned}\sigma^2 &= \int P(\mathbf{R})(f(\mathbf{R}_i) - \bar{f})^2 d\mathbf{R} \\ &\approx \frac{1}{M-1}\sum_{i=1}^{M}(f(\mathbf{R}_i) - \langle f\rangle)^2. \end{aligned} \tag{1.23}$$

Here, $\bar{f}$ denotes the mean value of the function f.

Importance sampling allows for a significant reduction in the number of stochastic steps required to achieve a certain level of accuracy by sampling configurations from a well–defined probability distribution $P(\mathbf{R})$. However, for the non-trivial $P(\mathbf{R})$, the normalisations of these multidimensional probability densities may not be known and are so complicated that they cannot be sampled directly. These obstacles can be overcome by utilising the Metropolis algorithm.

1.2.4.2 Metropolis algorithm

The importance sampling MC scheme using the Metropolis algorithm [27, 28] is an acceptance–rejection method that allows for sampling from an unnormalised probability density function without knowledge of the normalisation constant. In this method, a set of random walkers is efficiently generated with a particular choice of transition probability T. The transition probability satisfies the principle of detailed balance in configuration space such that the probability of moving in a given direction has the same probability as in the opposite direction, as shown below:

$$T(\mathbf{R}' \leftarrow \mathbf{R})P(\mathbf{R})A(\mathbf{R}' \leftarrow \mathbf{R}) = T(\mathbf{R} \leftarrow \mathbf{R}')P(\mathbf{R}')A(\mathbf{R} \leftarrow \mathbf{R}'). \tag{1.24}$$

where $A(\mathbf{R} \leftarrow \mathbf{R}')$ is the acceptance probability of a move from $\mathbf{R}'$ to $\mathbf{R}$. This approach generates a sequence of sampling points according to the following steps:

1. Generate a walker at a random position $\mathbf{R}'$.

2. Propose a trial move from $\mathbf{R}'$ to $\mathbf{R}$ with the transition probability density $T(\mathbf{R} \leftarrow \mathbf{R}')$.

3. Accept the move to the new configuration $\mathbf{R}$ with the following the probability:

$$A(\mathbf{R} \leftarrow \mathbf{R}') = \min\left\{1, \frac{T(\mathbf{R}' \leftarrow \mathbf{R})P(\mathbf{R})}{T(\mathbf{R} \leftarrow \mathbf{R}')P(\mathbf{R}')}\right\}. \tag{1.25}$$

   If the trial move is accepted, the new position $\mathbf{R}$ becomes the next point on the walk; otherwise, $\mathbf{R}'$ becomes the next point on the walk. Most trial moves in regions with lower probability are rejected, and a sufficiently long equilibration is needed.

4. Repeat step (2) onward until the required number of samples has been collected.

A common choice of T is a Gaussian with an appropriate width and mean centred on the current position of the walker. Although the Metropolis algorithm correctly samples the target distribution $P(\mathbf{R})$, the consecutive configurations are serially correlated. The serial correlation of the sampled configurations complicates the calculation of the statistical error bars on the estimated value. This issue can be addressed using the reblocking analysis, see Sec. 1.2.9.1.

In practice, all initial configurations generated before attaining equilibrium must be deleted since they are dependent on the starting point. The duration of the equilibration time can be determined from the number of steps necessary to verify that all transient effects of the initial distribution have vanished. Therefore, the root-mean-square (RMS) distance diffused by a particle in a period T of an imaginary time must be greater than the longest relevant length in the system. The RMS distance diffused is given by

$$RMS = \sqrt{2dDAN_{\text{move}}\tau}, \tag{1.26}$$

where d is the dimensionality, $D = 1/(2m)$ is the diffusion constant for a particle of mass m, A is the acceptance rate (around 1 in DMC and 1/2 in VMC) [25], N_{move} is the number of steps, and τ is the width of the move proposal probability density. Once the equilibrium is attained, the configurations are distributed according to the desired probability $P(\mathbf{R})$, and the detailed balance condition Eq. (1.24) is satisfied. Therefore, $P(\mathbf{R})$ is a stationary point of the Metropolis algorithm and the proposal transition probability T is ergodic, in which any point in the configuration space can be reached from another point in a finite number of moves, the algorithm will converge exponentially rapidly to that stationary point.

1.2.5 Variational Monte Carlo method

The variational Monte Carlo (VMC) method is a simple and elegant QMC algorithm. It is based on the incorporation of the variational principle and the Monte Carlo integration scheme discussed in Sec. 1.2.4.1 to evaluate the expectation values. Consider a many-electron wave function $\Psi_T(\mathbf{X})$, where $\mathbf{X} = (\{\mathbf{r}_1, \sigma_1\}, \{\mathbf{r}_2, \sigma_2\}, ..., \{\mathbf{r}_N, \sigma_N\})$ and $\mathbf{r}_i$ is the spatial coordinate of electron i with spin $\sigma_i \in \{\uparrow, \downarrow\}$. Assume that $\Psi_T(\mathbf{X})$ is an eigenfunction of the total spin operator $\hat{S}_z = \sum_{i=1}^{N} \hat{s}_{z_i}$ with eigenvalue $(N_\uparrow - N_\downarrow)/2$, where $N_\uparrow + N_\downarrow = N$. The expectation value of a spin-independent operator $\hat{A}$ with respect to $\Psi_T(\mathbf{X})$ is

$$\langle \hat{A} \rangle = \frac{\langle \Psi_T | \hat{A} | \Psi_T \rangle}{\langle \Psi_T | \Psi_T \rangle} = \frac{\sum_\sigma \int \Psi_T^*(\mathbf{X}) \hat{A} \Psi_T(\mathbf{X}) d\mathbf{R}}{\sum_\sigma \int |\Psi_T(\mathbf{X})|^2 d\mathbf{R}}, \tag{1.27}$$

where the sums are obtained over all spin configurations such that the number of electrons with a spin-up is $N_\uparrow$ and those with a spin-down is $N_\downarrow$. For fermion particles, the Ψ_T is antisymmetric under an exchange of electrons. As a result of the antisymmetry of Ψ_T, $\mathbf{X}$ can be replaced by

$$\mathbf{X}' = \Big(\{\mathbf{r}_1, \uparrow\}, ..., \{\mathbf{r}_{N_\uparrow}, \uparrow\}, \{\mathbf{r}_{N_\uparrow+1}, \downarrow\}, ..., \{\mathbf{r}_N, \downarrow\}\Big) \tag{1.28}$$

without modifying $\langle \hat{A} \rangle$. The spatial wave function can be defined as

$$\Psi_T(\mathbf{R}) = \Psi_T(\{\mathbf{r}_1, \uparrow\}, ..., \{\mathbf{r}_{N_\uparrow}, \uparrow\}, \{\mathbf{r}_{N_\uparrow+1}, \downarrow\}, ..., \{\mathbf{r}_N, \downarrow\}), \tag{1.29}$$

which is only antisymmetric under the exchanges of positions of same-spin electrons. Therefore, electrons of different spins are treated as distinguishable particles, and Ψ_T can now be called the trial wave function. The terms in the spin sums in Eq. (1.27) are identical; hence, the spin sums cancel each other out, and the expectation value of the operator $\hat{A}$ is given by

$$\langle \hat{A} \rangle = \frac{\int \Psi_T^*(\mathbf{R}) \hat{A} \Psi_T(\mathbf{R}) d\mathbf{R}}{\int |\Psi_T(\mathbf{R})|^2 d\mathbf{R}}. \tag{1.30}$$

The ground–state energy can now be evaluated using the VMC method as an expectation value of the Hamiltonian with respect to the trial wave function $\Psi_T(\mathbf{R})$ as follows:

$$\begin{aligned} E_{VMC} &= \frac{\langle \Psi_T(\mathbf{R}) | \widehat{H} | \Psi_T(\mathbf{R}) \rangle}{\langle \Psi_T(\mathbf{R}) | \Psi_T(\mathbf{R}) \rangle} \\ &= \frac{\int |\Psi_T(\mathbf{R})|^2 E_L d\mathbf{R}}{\int |\Psi_T(\mathbf{R})|^2 d\mathbf{R}} \geq E_0, \end{aligned} \tag{1.31}$$

where $\mathbf{R} = (\mathbf{r}_1, \mathbf{r}_2, .., \mathbf{r}_N)$ is a $3N$–dimensional vector that will be referred to hereupon as an electron configuration, E_{VMC} is the VMC energy, which is an upper bound of the true ground–state energy E_0 and $\hat{H}$ is the many-body Hamiltonian. We have used the importance sampling transformation

$$E_{VMC} = \int p(\mathbf{R}) E_L(\mathbf{R}) d\mathbf{R}, \tag{1.32}$$

where

$$p(\mathbf{R}) = \frac{|\Psi_T(\mathbf{R})|^2}{\int |\Psi_T(\mathbf{R})|^2 d\mathbf{R}} \tag{1.33}$$

is the probability distribution function at $\mathbf{R}$ and the local energy,

$$E_L = \Psi_T^{-1} \widehat{H} \Psi_T. \tag{1.34}$$

In the VMC method, the probability distribution $p(\mathbf{R})$ is sampled using a random walk procedure, such as the Metropolis MC algorithm 1.2.4.2. After an equilibration period, the local energy is accumulated along the walk and averaged over these sample points. The VMC expectation value is given by

$$E_{VMC} = \frac{1}{M} \sum_{i=1}^{M} E_L(\mathbf{R}_i). \tag{1.35}$$

The variance of energy is

$$\sigma^2 = \frac{1}{(M-1)} \sum_{i=1}^{M} (E_L(\mathbf{R}_i) - E_{VMC})^2, \tag{1.36}$$

where M refers to the number of generated configurations R_i after the equilibrium phase has been reached [24, 29]. In practice, this method involves the generation of trial moves that are accepted or rejected according to the Metropolis algorithm, in which each trial move is sampled from a Gaussian distribution with a variance chosen to ensure that the acceptance probability is around 50% [24]. In general, the VMC method is most often used to optimise the trial wave function parameters (see Sec. 1.2.7) that are varied to minimise the energy variance of local energy (see Sec. 1.2.8) and as a preliminary step for DMC simulation [29].

1.2.6 Diffusion Monte Carlo method

The accuracy of the VMC results is limited by the quality of the wave function. This limitation can be overcome using a more accurate method such as the diffusion

Monte Carlo (DMC) method. DMC is a projector method that takes advantage of the imaginary–time Schrödinger equation to project out the electronic ground-state component from the trial wave function.

1.2.6.1 Imaginary-time evolution

The imaginary–time Schrödinger equation (ITSE) is

$$\begin{aligned} -\frac{\partial}{\partial\tau}\Phi(\mathbf{R},\tau) &= (\widehat{H}-E_T)\Phi(\mathbf{R},\tau) \\ &= -\frac{1}{2}\nabla^2\Phi(\mathbf{R},\tau)+(V(\mathbf{R})-E_T)\Phi(\mathbf{R},\tau), \end{aligned} \tag{1.37}$$

where $\Phi(\mathbf{R},t) =$ is a function of the $3N$-dimensional configuration vector $\mathbf{R}$ of all N electron coordinates and $\tau = it$ is the imaginary time, ∇ is the 3N-dimensional gradient with respect to $\mathbf{R}$, $V(\mathbf{R})$ is the potential energy and E_T is a constant reference energy that is used to control the walker population during the simulation [24].

A general solution $\Phi(\mathbf{R},\tau)$ of Eq. (1.37) is

$$\Phi(\mathbf{R},\tau) = \sum_{i=0}^{\infty} c_i\phi_i(\mathbf{R})\ \exp[-(E_i-E_T)\tau], \tag{1.38}$$

where c_i is a set of expansion coefficients, and E_i and $\phi_i(\mathbf{R})$ are the ith eigenvalue and eigenfunction of the Hamiltonian $\hat{H}$, respectively. By choosing $E_T = E_0$ with the initial condition $c_0 \neq 0$, we get rid of the imaginary-time dependence of the wave function at large imaginary time τ. In the limit of $\tau \to \infty$, the stationary solution $\Phi(\mathbf{R},\tau\to\infty) = c_0\phi_0(\mathbf{R})$ is projected and the excited states die away exponentially relative to the ground state.

Considering only the kinetic term, the ITSE in Eq. (1.37) is reduced to a diffusion equation in the 3N-dimensional configuration space, whereas eliminating the kinetic term from Eq. (1.37) results in a rate equation. At the short–time $\delta\tau$ propagator, the DMC algorithm can be simulated by taking a set of configurations initially distributed as $\Phi(\mathbf{R},0)$ and randomly moving through the diffusion process. The rate process is interpreted as a "birth/death" algorithm is used to kill the walkers in regions of high V and replicate those in low V regions. After a long period of evolution in imaginary time, all the excited-states components will die away and leave just the wave function of the ground state.

However, this algorithm suffers from two serious limitations. First, the Coulomb potential $V(\mathbf{R})$ suffers from divergences at coalescences. The resulting divergence leads to significant fluctuation in the walker population and hence to poor statistical estimates of expectation values. This poor behaviour can be addressed using importance-sampling transformation [25]. The second issue is the fermion sign problem, addressed in Sec. 1.2.6.2, which affects all projector QMC methods.

1.2.6.2 The fermion sign problem

This problem arises from the assumption that Φ is interpreted as a probability distribution that is positive everywhere. This is valid for bosonic ground states, but the antisymmetric nature of many-particle fermionic wave functions necessitates both positive and negative regions. This is known as the 'fermion sign problem', and it impacts the DMC method, in which configurations are distributed according to the wave function Φ. The VMC method is unaffected by the fermion sign issue because the distribution of walkers therein is governed by $|\Psi_T|^2$, which is positive everywhere.

Taking the probability density of the walker population in non-importance sampled DMC to be $|\Phi|$ results in the so-called fixed-node approximation [30]. The nodes of the DMC wave function are taken to be almost correct and are fixed to the nodes of the trial wave function during the imaginary–time evolution, which divides the configuration space into nodal pockets. This approximation is equivalent to imposing an infinite repulsive potential barrier on the nodal surface of the trial wave function, which is strong enough to cause the wave function to be zero on the nodal surface. The Schrödinger equation in Eq. (1.37) is solved within each nodal pocket subject to the boundary condition that the wave function becomes zero on the nodal surface.

For complex wave functions, the fixed-phase approximation [31] results from forcing the complex wave function to have the same phase as the trial wave function. This approximation is the complex generalisation of the fixed-node approximation. The fixed-node approximation is for special cases in which the trial wave function is real and has a phase that is equal to 0 or π at each point in the configuration space. Although both approximations are uncontrolled, their performance is remarkable.

In the fixed-node approximation with an antisymmetric trial wave function, the ground-state DMC energy obeys the variational principle, with the error positive and second–order in the nodal surface error [32]. Similarly, the excited-state DMC energy is variational under the fixed-phase approximation with a trial wave function that transforms as a one-dimensional irreducible representation of the symmetry group of the Hamiltonian [33]. The fixed-node approximation can be efficiently implemented via importance– sampling transformation.

1.2.6.3 Importance-sampling transformation

The importance-sampling transformation in the DMC algorithm make use of the trial wave function Ψ_T to bias the random walk to form the mixed distribution $f(\mathbf{R},\tau) = \Phi(\mathbf{R},\tau)\ \Psi_T(\mathbf{R}) \geq 0$ rather than $\Phi(\mathbf{R},\tau)$, where the DMC wave function $\Phi(\mathbf{R},\tau)$ and the trial wave function $\Psi_T(\mathbf{R})$ have the same nodal surfaces. By substituting $\Phi(\mathbf{R},\tau) = \Psi_T^{-1}(\mathbf{R})f(\mathbf{R},\tau)$ into Eq. (1.37), the importance-sampled imaginary-time Schrödinger equation (ISITSE) then can be written as

$$-\frac{\partial}{\partial\tau}f(\mathbf{R},\tau) = -\frac{1}{2}\nabla^2 f(\mathbf{R},\tau) + \nabla\cdot[\mathbf{v}_D(\mathbf{R})f(\mathbf{R},\tau)] + [E_L(\mathbf{R}) - E_T]f(\mathbf{R},\tau), \quad (1.39)$$

where $\nabla = (\nabla_1, \nabla_2, ..., \nabla_N)$ is the $3N$-dimensional gradient and $\mathbf{v}_D(\mathbf{R})$ is the $3N$-dimensional drift velocity given by

$$\mathbf{v}_D(\mathbf{R}) = \Psi_T(\mathbf{R})^{-1}\nabla\Psi_T(\mathbf{R}). \quad (1.40)$$

The three terms on the right side of Eq. (1.39) describe diffusion, drift and branching processes, respectively.

The corresponding integral form of Eq. (1.39) can be written as

$$f(\mathbf{R},\tau+\delta\tau) = \int G(\mathbf{R}\leftarrow\mathbf{R}',\delta\tau)\ f(\mathbf{R}',\tau)\ d\mathbf{R}'\ , \quad (1.41)$$

with an importance-sampled Green's function defined as

$$G(\mathbf{R}'\leftarrow\mathbf{R},\delta\tau) = \langle\mathbf{R}'|e^{-\delta\tau(\hat{F}+E_L(\mathbf{R})-E_T)}|\mathbf{R}\rangle, \quad (1.42)$$

where $\hat{F} = (\frac{1}{2})\hat{\mathbf{P}}^2 + i\hat{\mathbf{P}}\cdot\mathbf{v}_D(\mathbf{R})$ is the Fokker-Planck operator, $\hat{\mathbf{P}}$ is momentum operator, and the Green's function $G(\mathbf{R}\leftarrow\mathbf{R}',\delta\tau)$ is the solution of Eq. (1.39) and satisfies the initial condition $G(\mathbf{R}\leftarrow\mathbf{R}',0) = \delta(\mathbf{R}-\mathbf{R}')$. Using the Trotter-Suzuki

formula [34],

$$\begin{aligned} G(\mathbf{R}' \leftarrow \mathbf{R}, \delta\tau) &= \langle \mathbf{R}' | e^{-\delta\tau(\hat{F}+E_L(\mathbf{R})-E_T)} | \mathbf{R} \rangle \\ &= \langle \mathbf{R}' | e^{-\delta\tau \frac{E_L(\mathbf{R}')-E_T}{2}} e^{-\delta\tau \hat{F}} e^{-\delta\tau \frac{E_L(\mathbf{R})-E_T}{2}} + O(\delta\tau^3) | \mathbf{R} \rangle \\ &= e^{-\delta\tau \frac{E_L(\mathbf{R}')-E_T}{2}} \langle \mathbf{R}' | e^{-\delta\tau \hat{F}} | \mathbf{R} \rangle \, e^{-\delta\tau \frac{E_L(\mathbf{R})-E_T}{2}} + O(\delta\tau^3). \quad (1.43) \end{aligned}$$

Within short-time-step approximation, the Green's function is approximated as the factorisation of a product of the drift–diffusion and branching components, which is as follows:

$$G(\mathbf{R} \leftarrow \mathbf{R}', \delta\tau) \approx G_d(\mathbf{R} \leftarrow \mathbf{R}', \delta\tau) \, G_b(\mathbf{R} \leftarrow \mathbf{R}', \delta\tau) \quad (1.44)$$

where

$$G_d(\mathbf{R} \leftarrow \mathbf{R}', \delta\tau) = (2\pi\delta\tau)^{-3N/2} \exp\left[-\frac{[\mathbf{R} - \mathbf{R}' - \delta\tau \mathbf{v}_D(\mathbf{R}')]^2}{2\delta\tau} \right] \quad (1.45)$$

is the drift-diffusion Green's function, and

$$G_b(\mathbf{R} \leftarrow \mathbf{R}', \delta\tau) = \exp\left\{ -\frac{\delta\tau}{2} [E_L(\mathbf{R}) + E_L(\mathbf{R}') - 2E_T] \right\} \quad (1.46)$$

is the branching Green's function. This simplification of the Green's function converges into the exact Green's function in the limit $\delta\tau \to 0$ [29]

Within this method, the DMC algorithm becomes more stable due to the replacement of the potential $V(\mathbf{R})$ by the local energy $E_L(\mathbf{R})$ in the branching factor. This is convenient because $E_L(\mathbf{R})$ is almost constant and is close to the ground–state energy. This reduces the population fluctuations significantly. Using the importance–sampling, the fixed-node approximation is implicitly enforced by the representation of $f(\mathbf{R}, \tau)$. The $f(\mathbf{R}, \tau)$ is positive everywhere in the configuration space and can now be interpreted as a probability distribution. As a result, whenever a walker approaches the wave function node, the drift velocity grows and prevents the walker from crossing the nodal surface. Also, sampling the wave function becomes more efficient because the drift velocity guides the walkers toward large regions of Ψ_T so that the more important part of the wave function is sampled more often [24].

The importance–sampling DMC algorithm starts with an initial distribution of configurations that is drawn from the distribution $f(\mathbf{R}, 0) = |\Psi_T(\mathbf{R})|^2$, as in the

VMC method. These configurations then evolve such that they sample the mixed distribution $f(\mathbf{R}, \tau)$ propagated depending on Eq. (1.44). In the drift-diffusion process, each walker is drifted from its old position $\mathbf{R}'$ over the distance $\mathbf{v}_D(\mathbf{R}')\delta\tau$ and diffused by a three-dimensional vector $\boldsymbol{\chi}$ of Gaussian random numbers with variance $\delta\tau$ and a zero mean, such that

$$\mathbf{R} = \mathbf{R}' + \boldsymbol{\chi} + \mathbf{v}_D(\mathbf{R}')\delta\tau. \tag{1.47}$$

The importance-sampled Green function can be interpreted as a transition probability density for the stochastic imaginary-time evolution of walkers in the configuration space. The detailed–balance condition can then be read as

$$G(\mathbf{R} \leftarrow \mathbf{R}', \tau)|\Psi_T(\mathbf{R}')|^2 = G(\mathbf{R}' \leftarrow \mathbf{R}, \tau)|\Psi_T(\mathbf{R})|^2, \tag{1.48}$$

where detailed balance follows from the Hermiticity of the Hamiltonian [25]. In the limit of small time steps, the detailed-balance condition is violated due to the approximation that the drift velocity $\mathbf{v}_D$ is constant over the walkers' move. This issue can be solved by including Metropolis–style acceptance–rejection steps in G_d. The detailed-balance condition is reimposed by requiring that a trial move from $\mathbf{R}'$ to $\mathbf{R}$ is accepted with the following probability:

$$P_{accept}(\mathbf{R} \leftarrow \mathbf{R}') = \min\left[1, \frac{G_d(\mathbf{R}' \leftarrow \mathbf{R}, \tau)|\Psi_T(\mathbf{R})|^2}{G_d(\mathbf{R} \leftarrow \mathbf{R}', \tau)|\Psi_T(\mathbf{R}')|^2}\right]. \tag{1.49}$$

Each attempt to cross the nodal surface of the mixed distribution, will be rejected, and the walker will remain in its original position. In this process, it has been found to be more efficient and faster to use an electron–by–electron algorithm in which one electron at a time is moved rather than to use the configuration–by–configuration algorithm, particularly for large systems [35].

In real calculations, using a finite imaginary–time step in the Green's function in Eq. (1.44) leads to time-step bias in DMC calculations. This bias is linear in the limit of a sufficiently small time step and can be largely removed via extrapolation to zero–time step by performing a linear fit of the DMC energies evaluated as a function of τ. The choice of the time–step for DMC calculations is guided by the shortest length scale L_{small} in the system of interest. For a d-dimensional system, the root–mean–square (RMS) distance diffused by an electron in each time–step,

$\sqrt{d\tau}$, should be less than L_{small}.

The branching process is simulated by allowing the growth and decay of the mixed distribution over periods of imaginary time by adjusting the reference energy E_T that appears in Eq. (1.46) throughout a simulation to keep the configuration population under control and close to the target population. This introduces inevitable positive systematic population-control bias into the DMC energy. This bias is inversely proportional to the population size and can be removed simultaneously with time-step bias extrapolation [35]. After a period of equilibration in which the length is determined using Eq. (1.26), the excited–state contributions die away; hence, $f(\mathbf{R})$ has the desired ground–state mixed distribution. The walkers can be further propagated in imaginary time to accumulate and average the needed quantities, particularly the DMC energy, using the mixed estimator

$$\begin{aligned} E_{best} = E_{DMC} &= \frac{\langle \phi_0 | \hat{H} | \Psi_T \rangle}{\langle \phi_0 | \Psi_T \rangle} \\ &= \lim_{\tau \to \infty} \frac{\int f(\mathbf{R}, \tau) E_L(\mathbf{R}) \, d\mathbf{R}}{\int f(\mathbf{R}, \tau) \, d\mathbf{R}} \\ &\approx \frac{1}{M} \sum_{i=1}^{M} E_L(\mathbf{R}_i), \end{aligned} \tag{1.50}$$

where M is the set of walkers of $f(\mathbf{R}, \tau)$ that are propagated in the statistics-accumulation phase. Aside from the fixed-node error in the DMC ground–state solution, the mixed estimator is accurate for operators that commute with the Hamiltonian.

For operators that do not commute with the Hamiltonian, the systemic errors in both the VMC and DMC estimates are linear to the error in the trial wave function. The unbiased estimates can then be obtained using the extrapolated technique [36] as follows:

$$\langle \hat{S} \rangle_{\text{ext}} = 2 \langle \hat{S} \rangle_{\text{DMC}} - \langle \hat{S} \rangle_{\text{VMC}}, \tag{1.51}$$

where $\hat{S}$ denotes the operator that corresponds to the physical quantity of interest, and the accuracy of the extrapolation depends on the quality of the trial function. The error in the extrapolated estimate is quadratic in the error in the trial wave function.

1.2.7 The trial wave function

The appropriate choice of trial wave function is important in both the VMC and DMC methods. The VMC method relies entirely on the trial wave function, whereas the DMC method depends only on the quality of the nodal surface of the wave function [29]. An accurate trial wave function that considers the relevant correlations in the system is important to avoid a large statistical noise, time-step bias, and population-control bias.

The many-electron wave function can be constructed as a product of a small number of antisymmetric Slater determinants and a positive, symmetric parametrised Jastrow factor [37]. The number of determinants required to retrieve a given fraction of the correlation energy with a multideterminant wave function increases exponentially with the system size, making it challenging to converge the results. However, the use of a single determinant for periodic systems has been found to be effective in maintaining the correct symmetry and retrieving a substantial fraction of the correlation energy [24]. The single-determinant Slater-Jastrow wave function for a fermionic system is formally written as:

$$\begin{aligned} \Psi_T(\mathbf{R}) &= e^{J(\mathbf{R})}\Psi_S^{\uparrow}(\mathbf{r}_1, ..., \mathbf{r}_{N_\uparrow})\Psi_S^{\downarrow}(\mathbf{r}_{N_\uparrow+1}, ..., \mathbf{r}_N), \\ &= \mathrm{e}^{J(\mathbf{R})}\Psi_S(\mathbf{R}), \end{aligned} \tag{1.52}$$

where $J(\mathbf{R})$ denotes the Jastrow correlation factor and Ψ_S is decomposed into a product of spin-up and spin-down determinants usually constructed using DFT or HF calculations.

The antisymmetric feature of the Slater determinant ensures that the fermionic symmetry of the wave function is satisfied under the exchange of the position vectors of same-spin electrons. The Jastrow factor must be a positive symmetric function under exchange of same-spin positions to maintain the nodal surface defined by the Slater part of the trial wave function [29]. In the absence of the Jastrow correlation factor, the QMC calculations with only Ψ_S are reduced to the HF level. The inclusion of the Jastrow factor provides a description of the dynamical correlation effects between the particles, so that the correlation energy can be estimated as the difference between the HF energy and the best available QMC energy.

1.2.7.1 The standard Jastrow factor

The general form of the Jastrow factor for N electrons and N_{ion} nuclei, such as that developed by Drummond et al. [37], is written as

$$J(\mathbf{R}) = \sum_{i>j}^{N} u(\mathbf{r}_{ij}) + \sum_{I=1}^{N_{ions}} \sum_{i=1}^{N} \chi_I(\mathbf{r}_{iI}) + \sum_{I=1}^{N_{ions}} \sum_{i>j}^{N} f_I(\mathbf{r}_{iI}, \mathbf{r}_{jI}, \mathbf{r}_{ij}) + \sum_{i=1}^{N-1} \sum_{j=i+1}^{N} p(\mathbf{r}_{ij}), \tag{1.53}$$

which is sum of electron–electron (u), electron–nuclear (χ) and electron–electron–nucleus (f) terms and additionally of the cuspless plane-wave expansion (p) term for periodic systems. The terms $\boldsymbol{r}_{ij}$, $\boldsymbol{r}_{iI}$, $\boldsymbol{r}_i$ and $\boldsymbol{r}_I$ are the electron–electron and electron–nuclei separation vectors and the position vectors of the electrons and nuclei, respectively. The two-body u term behaves according to the cusp conditions (see Sec. 1.2.7.2), but also causes an unintended change in the electronic charge density: the electrons are pushed from a high density region toward a lower one. However, the correct DFT or HF form of the charge density can be retrieved using the single-body χ function.

In periodic systems, QMC calculations are performed on simulation cells subject to periodic boundary conditions. In such systems, the separation vectors are evaluated under the minimum-image convention [29]. Hence, the u, χ and f terms should be truncated at a distance less than or equal to a radius of the largest sphere that can be inscribed in the Wigner-Seitz simulation cell to eliminate the sums over the images. However, the truncation of the u term at the edge of the periodic cell reduces its efficiency in capturing long–range correlations. The inclusion of the p term adds greater variational freedom in the corners of the simulation cell, which allows the correct description of correlation in the corners of the simulation cell [37, 38].

The functional form of the Jastrow factor components should be parametrised efficiently using power expansions with optimisable coefficients. For example, the two-body u term in the Drummond-Towler-Needs Jastrow factor is written as

$$u(r_{ij}) = (r_{ij} - L_u)^C \Theta(L_u - r_{ij}) \times \left(\alpha_0 + \left[\frac{\Gamma_{ij}}{(-L_u)^C} + \frac{C\alpha_0}{L_u} \right] r_{ij} + \sum_{l=2}^{N} \alpha_l r_{ij}^l \right), \tag{1.54}$$

where L_u is the cut-off distance, C is the truncation order, Θ is a Heaviside step function, α_l are optimisable parameters and Γ_{ij} is a constant determined by the

cusp conditions. In this expression, if $C = 2$, the gradient of u is continuous but the second derivative and thus, the local energy, is discontinuous; and if $C = 3$, both the gradient and the local energy are continuous. The complete description of the Jastrow factor can be found in the original paper [37] and the CASINO manual [38].

1.2.7.2 The Kato cusp conditions

The components of the Jastrow factor of Eq. (1.53) should be chosen to enforce the Kato cusp conditions [39]. These conditions define the behaviour of the many-body wave function at the coalescence points. For a system of charged particles, the Coulomb potential energy suffers from divergence whenever two particles coincide. However, the true eigenstate of the Hamiltonian has a smooth and constant local energy throughout the configuration space. To neutralise the singularity of the trial wave function at the coalescence points, an equivalent and opposite divergence in kinetic energy must be forced to cancel out the divergence in the potential energy. For any two particles with charges q_i and q_j and masses m_i and m_j interacting via the Coulomb potential, the Kato cusp condition is

$$\frac{\partial J(\mathbf{R})}{\partial r_{ij}} = \frac{2q_i q_j \mu_{ij}}{d \pm 1} = \Gamma_{ij}, \tag{1.55}$$

where $\mu_{ij} = m_i m_j/(m_i+m_j)$ is the reduced mass and d represents the dimensionality. The positive and negative signs in the denominator are for the indistinguishable and distinguishable particles, respectively. For the Jastrow factor of Eq. (1.53), the Kato cusp conditions can then be written as conditions $\Gamma_{ij} = \frac{1}{2}$ for unlike-spin electrons pairs, $\Gamma_{ij} = \frac{1}{4}$ for like-spin electron pairs, and $\Gamma_{iI} = -Z$ for the electron–nucleus cusp.

As mentioned above, fixed-node approximation is applied to overcome the fermion sign problem in the DMC method. Consequently, the quality of the DMC energy obtained with merely the Slater-Jastrow wave function is limited by the accuracy of the trial wave function $\Psi_S(\mathbf{R})$ nodes. One can of course go beyond the standard form of the Slater-Jastrow wave function to optimised the shape of the nodes by improving the orbital component of the wave function using a higher-order technique such as backflow transformation (1.2.7.3). In recent years, a remarkable

improvement in accuracy has been seen through the introduction of pairing orbitals [40, 41] (Sec. 4.2.1) and multideterminant expansion [25, 42] (Sec. 1.2.7.4) for characterising excited and degeneracy states in QMC calculations.

1.2.7.3 Backflow transformations

Introducing backflow transformations can incorporate further correlation effects in the trial wave function and leads to further variational freedom in the antisymmetric part of the trial wave function $\Psi_S(\mathbf{R})$ [43–45]. The Slater determinant orbitals are evaluated by transforming the coordinate positions $\mathbf{R}$ in Eq. (1.52) into the new collective coordinates $\mathbf{X}(\mathbf{R}) = (\mathbf{x}_i, \mathbf{x}_2, ..., \mathbf{x}_n)$, the so-called 'quasiparticle' coordinates, which are given by

$$\mathbf{x}_i = \mathbf{r}_i + \xi_i(\mathbf{R}) \tag{1.56}$$

where $\xi_i(\mathbf{R})$ is the backflow displacement vector for particle i, which is a function of the position of all the other electrons in the system, given by

$$\xi(\mathbf{R}) = \sum_{i\neq j}^{N} \eta(r_{ij})\mathbf{r}_{ij} + \sum_{I=1}^{N_{ion}}\sum_{i=1}^{N} \mu(r_{iI})\mathbf{r}_{iI} + \sum_{i\neq j}^{N}\sum_{I}^{N_{ion}}[\Phi(r_{iI}, r_{jI}, r_{ij})\mathbf{r}_{ij} + \theta(r_{iI}, r_{jI}, r_{ij})\mathbf{r}_{iI}] \tag{1.57}$$

In this expression, ξ takes a form developed by López Ríos et al. [46] analogous to the parametrisation of the Jastrow factor in Eq. (1.53) where electron–electron $\eta(r_{ij})$, electron–nucleus $\mu(r_{iI})$ and electron–electron–nucleus $\Phi(r_{iI}, r_{jI}, r_{ij})$, $\theta(r_{iI}, r_{jI}, r_{ij})$ are correlation functions.

1.2.7.4 Multideterminant (MD) expansions

Using a linear combination of a few determinants, also known as a multideterminant expansion, significantly improves the trial wave function, expressed as:

$$\Psi_{\mathrm{MD}}(\mathbf{R}) = \mathrm{e}^{J(\mathbf{R})} \sum_{n}^{N_{\mathrm{det}}} c_n \det[\psi_n(\mathbf{r}_i^{\uparrow})] \det[\psi_n(\mathbf{r}_i^{\downarrow})], \tag{1.58}$$

where c_n are coefficients. The use of a multi-determinant wave function in the modelling of extended systems is impracticable since the number of determinants required to reach a specific level of accuracy grows exponentially with the system size.

1.2.8 Wave function optimisation

In the VMC and DMC methods, the statistical efficiency and accuracy of the results are determined by the quality of the trial wave function [24]. Typically, the most expensive part of VMC and DMC computations is the repetitive evaluation of the trial wave function and its gradient. As a result, it is important to use an appropriate trial wave function that is as precise as possible and yet can still be evaluated quickly. VMC simulations are often used to optimise the wave function by minimising the VMC energy or its variance.

The VMC method is typically used to optimise the many-electron trial wave function that includes a set of free parameters $\{\alpha\}$ defined in Eq. (1.53) by minimising the required *cost function* with respect to the values of these parameters. For instance, one can minimise the variance of the local energy as follows:

$$\sigma_E^2 = \frac{\int |\Psi_T(\mathbf{R})|^2 |E_L(\mathbf{R}) - E_{VMC}|^2 \, d\mathbf{R}}{\int |\Psi_T(\mathbf{R})|^2 \, d\mathbf{R}}, \tag{1.59}$$

Ideally, the local energy $E_L(\mathbf{R})$ for the exact trial wave function is the true eigenstate energy with zero variance. The variance minimisation approach [47, 48], is carried out via a correlated–sampling scheme in which a set of configurations distributed according to $|\Psi_T(\mathbf{R})|^2$ is generated and used to optimise the parameters. The procedure is iterated until the parameters converge to optimal values of the wave function with low variance of the local energy (self-consistency).

The variance minimisation method effectively optimises the linear parameters of the Jastrow factor, but it performs badly when optimising parameters that modified the nodal surface of the trial wave function. Changing these parameter values throughout the optimisation cycle will shift the nodal surface across the configurations, which will cause the local energy to diverge whenever a configuration coincides with the nodal surface. A similar technique that can be useful in this situation involves minimising the mean absolute deviation (MAD) [49] of the local energies from the median local energy instead of the variance.

Another approach is the energy minimisation method. The approach proposed by Nightingale and Melik-Alaverdian [50] changes the stochastic optimisation issue into the diagonalisation of the Hamiltonian matrix in a finite basis set. The hard integral evaluation in the diagonalisation procedure is replaced by a more stable

least-squares fitting. This method works very well for linear parameters in the trial wave function and it was extended by Umrigar et al. [51, 52] to optimise nonlinear parameters in the trial wave function.

In this scheme, the resulting VMC energies are usually lower than those obtained using the variance minimisation method [29]. This method is also useful for optimising parameters that modify the nodal surface, such as the backflow parameters. The resulting optimised wave function significantly improves the efficiency of the importance–sampled DMC algorithm [53]. In this thesis, the variance minimisation method was used to generate initial trial wave functions, after which energy minimisation was performed to obtain the final trial wave functions.

1.2.9 Source of uncertainty in VMC and DMC calculations

1.2.9.1 Serial correlations

The estimated value in the Monte Carlo framework has its associated statistical error that determines the confidence intervals of the estimate. Although serial correlation has no impact on estimated values, it complicates the calculation of the statistical error bar in the mean estimate. Serial correlation affects both VMC and DMC, but it is more severe in DMC due to the use of a small time step to reduce the effect of the Green's function approximation. For an accurate estimate of the error bar one must correct for serial correlation. The reblocking approach is a straightforward and effective technique for eliminating serial correlation [54]. For a sufficient sized data set, serially correlated data are repeatedly divided into blocks of successive pairs. The data within each pair are averaged to produce a new data set with half the number of points. As the block length increases, the standard error of the mean increases until it hits a plateau, at which point the block averages are completely independent of one another and the standard error in the mean is correctly estimated [25].

1.2.9.2 Pseudopotentials in the QMC

All-electron DMC calculations scale with atomic number Z from $Z^{5.5}$ to $Z^{6.5}$ [53, 55, 56]. Thus, all-electron QMC calculations are feasible only for light atoms with

atomic numbers $Z < 10$ and have been found to be prohibitively expensive for extended systems of atoms. The existence of core electrons results in two inevitable issues. The first issue is that both the kinetic and potential energies are large near the nucleus, which causes large fluctuations in the local energy. Second, the variation over the short length scale in the wave function close to the nucleus of a heavy atom requires the use of a smaller time-step to converge the results in the linear-time step bias regime. These issues are normally addressed by using pseudopotentials to remove the chemically inert core electrons and nucleus from the problem and create an effective potential to reproduce their effect on the valence electrons.

The use of non-local pseudopotentials in DMC calculations introduces further errors because the non-local pseudopotentials cannot be applied to the implicit probability distribution of the many-body wave function [25]. This issue is often solved by utilising locality approximation, in which the non-local component of the pseudopotential ($\hat{V}_{NL}$) acts on the trial wave function rather than on the DMC wave function, so, $\hat{V}_{NL}$ is replaced by $\Psi_T^{-1}\hat{V}_{NL}\Psi_T$. The leading-order error in this approximation is of second order in the wave function error, which impacts the stability of the DMC computations due to the loss of the variational property. An alternative solution is the implementation of the semi-locality approximation 'T-move scheme' introduced by Casula et al. [57] for dealing with non-local pseudopotentials in DMC calculations.

In this thesis, the non-local Trail & Needs Dirac-Fock (TNDF) pseudopotentials [58, 59] were used in VMC and DMC calculations with the plane-wave cut-off energy values determined in [60]. The T-move scheme [57] has been used in DMC calculations to ensure that the variational principle is obeyed. For plane-wave DFT calculations, the local channel for the TNDF pseudopotentials must be chosen to have an s angular-momentum to avoid ghost states. This problem arises from the use of the Kleinman-Bylander representation of pseudopotentials in the plane-wave DFT calculations [61]. In contrast, the QMC calculations do not employ the Kleinman-Bylander representation, and the local channel of the pseudopotentials with the highest angular-momentum component can be selected [60].

1.2.9.3 Fixed-node error

In theory, the DMC method is an exact approach, but its accuracy is restricted by the uncontrolled but variational fixed-node approximation used to deal with the fermionic nature of the anti-symmetric many-body wave function. The use of fixed-node approximation with a trial wave function that transforms as a one-dimensional (1D) irreducible representation (irrep) of the full symmetry group of the Hamiltonian provides a variational principle with respect to the lowest-lying eigenstate that transforms as that 1D irrep. Therefore, the DMC energy fulfils the variational principle only for the ground state and a few excited states. For the excited state that corresponds to degenerate states, the trial wave function transforms as a multi-dimensional irrep of the full symmetry group, which may lead to a DMC energy lower than the lowest energy of the exact eigenstate of that symmetry. A weaker variational principle can be realised again by selecting a trial function that transforms as a 1D irrep of a subgroup of the full symmetry group. In this case, the DMC energy is an upper or equal bound on the eigenvalue of the lowest exact eigenstate with the specified subgroup symmetry. Thus, the fixed-phase DMC can estimate excited-state energies by using a suitable trial wave function [25, 33]. However, the use of the fixed-node approximation introduces inevitable positive fixed-node errors that scale as second–order in the error in the trial wave function's nodal surface, which can be reduced by using a good trial wave function. The use of backflow transformations in DMC calculations can recover a significant fraction of the fixed-node errors, where backflow does not involve changing the nodal structure [46].

1.2.9.4 Finite-size errors

The main source of finite-size (FS) errors in the many-particle approaches, such as QMC, is the performance of the computations in a simulation cell of limited number of unit cells subject to periodic boundary conditions rather than infinite cells. Unlike single-particle methods, explicitly correlated methods require the use of a supercell as the long-range of electrons correlation may exceed the primitive cell. The supercell approach allows the removal of unwanted surfaces and preserves lattice transitional symmetry but includes the periodic image interaction effects [25]. This

issue can be addressed by calculating the DMC energy at different system sizes and then extrapolating the results to an infinite system size. In addition, performing computations in a finite unit cell involves approximating the continuous integral over the first Brillouin zone by summing over a discrete set of k-point wave vectors with a fixed electron number. This results in oscillatory single-particle finite-size errors, which cause the QMC energy per atom to vary as the size of the system is altered. This issue can be mitigated by using the canonical-ensemble twist averaging approach [62], which involves averaging the energy over offsets to the grid of k-vectors. Further discussion of the effects of finite size can be found in the following chapters.

Chapter 2

Vibrational renormalisation of quantum Monte Carlo band gaps via random sampling of normal coordinates

2.1 Introduction

First-principles electronic-structure calculations have been widely used to examine electronic band structures over the past four decades. Density-functional theory (DFT) approaches using the local density approximation (LDA) and generalised–gradient–approximation exchange–correlation (XC) functionals often succeed remarkably well in describing ground-state properties. However, even if an XC functional that produces the exact ground-state energy were used, DFT would still fail to provide exact band gaps [13], and it is well known that in practice, DFT significantly underestimates gaps. This issue has prompted much research on the calculation of electronic band gaps using more sophisticated methods, such as DFT with hybrid exchange–correlation functionals [63, 64] and *GW* many-body perturbation theory [65–68]. Second-order Møller-Plesset perturbation theory has been found to be unreliable for band-gap calculations [69]. Quantum–chemistry–based approaches, such as similarity–transformed equation of motion coupled–cluster methods, have been used to compute energy gaps for small clusters of atoms

in order to determine bulk band gaps [70], but such cluster calculations inevitably suffer from surface effects, and successful calculations rely on the examination of carefully selected finite clusters. In this study, we focus on quantum Monte Carlo (QMC) methods, which have been shown to be applicable to a broad range of systems and can accurately predict a wide range of ground-state and excited-state properties [24, 71]. QMC has previously been used to investigate the energy gaps of several molecular and crystalline systems [72–75].

Many theoretical methods are devoted to investigating the electronic–structure modification induced by electron–phonon coupling using first-principles approaches. The Allen–Heine–Cardona theory, known also as the quadratic approximation, [76, 77] evaluated the zero-point renormalisation and temperature dependence of band structure by taking the thermal average over an ensemble of atomic displacements based on the perturbation theory framework. This approach has been applied in many first-principles calculations [78–84]. The ab initio frozen-phonon approach allows for the inclusion of electron–phonon effects by computing the change of the electronic eigenvalues due to atomic displacements along the normal modes [81, 83–88]. Alternatives to perturbational methods for the study of electronic and vibrational properties have succeeded in capturing the nuclear quantum effects and solving the electronic problem based on the framework of the Born–Oppenheimer approximation. Path-integral molecular dynamics (PIMD) [89] has been combined with electronic–structure methods to examine the effect of electron–phonon coupling on the band gap [90, 91]. More recently, Monte Carlo (MC) integration methods [92, 93] have been used widely [94–99]. Acceleration techniques for the MC sampling scheme has been developed, such as the thermal lines method proposed by Monserrat (2016) [100] and one-shot method by Zacharias and Giustino (2016) [101].

Over the past decades, several studies have investigated the incorporation of vibrational-renormalisation corrections in first-principles calculations. These studies have shown that for systems with light atoms or weak bonding, zero-point atomic vibrations can have a significant effect on properties such as electronic band gaps and thermodynamic stability, highlighting the importance of including vibrational corrections in any comparison between theoretical and experimental results [102, 103]. In many cases, vibrational renormalisation results in a significant

decrease in electronic band gaps. In the case of diamondoids, a frozen-phonon approach based on DFT calculations has been used to account for vibrational effects, resulting in a correction to the static nucleus energy gap of between −0.1 and −0.3 eV [104]. Vibrational renormalisations of electronic band gaps at the DFT level have recently been shown to be as high as −0.4 eV for diamond and −0.03 eV for silicon [99]. The vibrational-renormalisation correction has been found to be very strong in the case of hexagonal ice, resulting in a significant decrease in the electronic band gap of more than −1.5 eV [105, 106]. Monserrat *et al.* [97] calculated the effect of electron–phonon coupling in molecular crystals of CH_4, NH_3, H_2O, and HF, revealing strong zero-point effects on the band gaps ranging from −1.0 eV in NH_3 to −2.0 eV in CH_4. Recent work by Hunt *et al.* [107] has evaluated the DFT vibrational renormalisation of the gaps of monolayer and bulk hBN. The vibrational corrections were found to be significant in both the monolayer (−0.73 eV) and the bulk (−0.40 eV) at 300 K. Because DFT already underestimates band gaps, including vibrational-renormalisation corrections generally exaggerates the disagreement with experimental results. It is therefore essential to combine vibrational-renormalisation corrections with more accurate methods for calculating static-nucleus band gaps.

Post-DFT methods have also been used to investigate the vibrational renormalisation of band gaps. For example, using the G_0W_0 corrections to the LDA band gap within the many-body perturbation theory, the zero-point renormalisation of the direct band gap of diamond has been determined to be −0.2 eV [81]. A larger zero-point correction of −0.6 eV has been obtained using Allen-Heine-Cardona perturbation theory and a scissor operator equivalent to the GW correction [79]. Monserrat [99] has evaluated the zero-point vibrational correction and temperature dependence of the direct band gap of silicon, diamond, TiO_2, LiF, and MgO using the many-body G_0W_0 approximation via the mean thermal line. The zero-point renormalisation results in a large correction to the direct gap of diamond (−640 meV, LiF (−500 meV), and MgO (−210 meV) and in a slight decrease in silicon (−52 meV) and TiO_2 (−150 meV).

Seeking a more accurate approach to electronic structure, several recent studies have used the diffusion Monte Carlo (DMC) technique to compute the ground-

state and excited-state energies for atomic configurations generated by molecular dynamics (MD). The first implementation to combine the QMC method and the ab initio MD simulation was introduced by Grossman and Mitas (2005) [108]. This approach evaluates the electronic energy within the QMC method along the nuclear trajectories that are generated using the DFT/MD method. More recently, Azadi *et al.* [109] has used DMC-PIMD calculations to evaluate the harmonic and anharmonic effects on the quasiparticle and excitonic band gaps of dense hydrogen at finite temperature. Coupled electron–ion Monte Carlo is an ab initio method based entirely on QMC algorithms [110, 111]. In this approach, the electronic problem is solved within the Born–Oppenheimer approximation using an electronic–ground–state QMC calculation, and the ionic degrees of freedom are sampled with a Metropolis algorithm at a fixed temperature [112–114]. However, the application of these method is focussed on the study of phase transition diagrams rather than the electron excitations.

The true potential energy surface is typically approximated by a quadratic function with a single minimum at the equilibrium point with fixed lattice vectors. In this quasiharmonic approximation, the vibrational Hamiltonian separates into a set of independent harmonic–oscillator Hamiltonians, one for each normal mode (see Sec. 2.2.2); quanta of vibrational energies are referred to as phonons. Small deviations from the ideal quadratic potential energy at fixed lattice vectors, referred to as anharmonicity, result in phonon–phonon scattering and thermal expansion effects. In this study, however, we focus on harmonic vibrational effects on the electronic structure, neglecting anharmonic effects as a small correction to a small correction.

Therefore, this chapter focuses on the vibrational renormalisation of band gaps at zero and finite temperature by developing a methodology that accounts for vibrational effects with the QMC technique in order to achieve quantitative accuracy in gap calculations.

2.2 Theoretical background

2.2.1 The vibrational Schrödinger equation

A complete quantum description of the nuclei vibrations can be provided by solving the Schrödinger equation for the nuclei, which is an important many-body problem. Starting from the eigenvalue problem for a system of coupled electrons and nuclei,

$$\hat{H}\Psi_s(\{\mathbf{r},\mathbf{R}\}) = E_s\Psi_s(\{\mathbf{r},\mathbf{R}\}), \tag{2.1}$$

where $\{\mathbf{r}\}$ are the electron coordinates, $\{\mathbf{R}\}$ are the nuclear coordinates, $\hat{H}$ is the fundamental Hamiltonian defined in Eq. (1.2) and E_s is the total energy of the sth eigenstate of the coupled system. The full solutions wave function Ψ_s can be written as the product

$$\Psi_s(\{\mathbf{r},\mathbf{R}\}) = \sum_i \chi_{si}(\{\mathbf{R}\})\Psi_i(\{\mathbf{r}\}:\{\mathbf{R}\}), \tag{2.2}$$

where $\Psi_i(\{\mathbf{r}\}:\{\mathbf{R}\})$ is the electronic wave function that describes a complete set of electronic states at each nuclear coordinates $\{\mathbf{R}\}$ and $\chi_{si}(\{\mathbf{R}\})$ are the expansion coefficients that depend on the nuclear coordinates. Inserting Eq. (2.2) into the time-independent Schrödinger equation with the total Hamiltonian of Eq. (1.2), multiplying from the left by $\Psi_i^\dagger(\{\mathbf{r}\}:\{\mathbf{R}\})$, and integrating over the electron variables $\mathbf{r}$, we obtain

$$\Big[\sum_{R_l,\kappa} -\frac{1}{2m_\kappa}\nabla_{l\kappa}^2 - E_i^{\text{elec}}(\{\mathbf{R}\}) - E_s\Big]\chi(\{\mathbf{R}\}) = -\sum_i C_{ii'}\chi(\{\mathbf{R}\}), \tag{2.3}$$

where κ denotes the different atoms within a primitive unit cell, m_κ is the mass of atom κ, $\mathbf{R}_l$ denotes the position vectors of the unit cell, and $E_i^{\text{elec}}(\{\mathbf{R}\})$ is electronic energy. The $C_{ii'}$ are the matrix elements given by

$$\begin{aligned} C_{ii'}(\{\mathbf{R}\}) &= A_{ii'}(\{\mathbf{R}\}) + B_{ii'}(\{\mathbf{R}\}) \\ &= -\sum_\kappa \frac{1}{m_\kappa}\langle\Psi_i(\{\mathbf{r}\}:\{\mathbf{R}\})|\nabla_\kappa|\Psi_{i'}(\{\mathbf{r}\}:\{\mathbf{R}\})\rangle\nabla_\kappa \\ &\quad -\sum_\kappa \frac{1}{2m_\kappa}\langle\Psi_i(\{\mathbf{r}\}:\{\mathbf{R}\})|\nabla_\kappa^2|\Psi_{i'}(\{\mathbf{r}\}:\{\mathbf{R}\})\rangle. \end{aligned} \tag{2.4}$$

and describe the electrons' transitions between the electronic states.

Under the Born–Oppenheimer (BO) approximation [7], a small change in the nuclear positions affects the electronic state only adiabatically; the electrons remain in their given electronic state as the nuclei move. In contrast, the nuclei can be affected only by the time–averaged adiabatic electronic potential. This assumption is valid only for materials with nuclei that are heavy enough for the lattice vibration energy to be much lower than the electron's excitation energy between the electronic levels. The nonadiabatic $C_{ii'}$ terms in Eq. (2.4) can therefore be neglected. The nuclear motion now can be described by a purely nuclear Schrödinger equation:

$$\left[\sum_{R_l,\kappa} -\frac{1}{2m_\kappa}\nabla^2_{l\kappa} + E^{\text{elec}}_{ni}(\{\mathbf{R}\})\right]\chi_{ni}(\{\mathbf{R}\}) = \hat{H}_{\text{vib}}\chi_{ni}(\{\mathbf{R}\}) = E^{\text{vib}}_{ni}\chi_{ni}(\{\mathbf{R}\}), \quad (2.5)$$

where n denotes the nuclear state and E^{vib}_{ni} and E^{elec}_{ni} are, respectively, the vibrational energy and the electronic total energy result from solving the electronic Schrödinger equation as a function of nuclear positions, known as the 'BO energy surface'. Using the harmonic approximation, the nuclear motion problem of Eq. (2.5) can be described classically with a set of simple independent harmonic oscillators. Some phenomena, such as thermal expansion, cannot be explained with this method, which is a significant limitation. In this thesis, the treatment of lattice vibration effects will be limited to the harmonic approximation.

2.2.2 Lattice dynamics

Suppose atom κ in the lth unit cell is displaced from its equilibrium position $\mathbf{x}(l\kappa)$ by a small amount $\mathbf{u}(l\kappa)$ compared to the lattice spacings. The instantaneous positions of the atoms are

$$\mathbf{R}(l\kappa) = \mathbf{x}(l\kappa) + \mathbf{u}(l\kappa). \quad (2.6)$$

Under this condition, the BO potential can be expanded in a power series with respect to the atomic displacement $\mathbf{u}(l\kappa)$ to give what is known as the Taylor expansion, that is,

$$\phi = \phi_0 + \sum_{l\kappa\alpha} \phi_\alpha(l\kappa)u_\alpha(l\kappa) + \frac{1}{2}\sum_{\substack{l\kappa\alpha \\ l'\kappa'\beta}} u_\alpha(l\kappa)\phi_{\alpha\beta}(l\kappa; l'\kappa')u_\beta(l'\kappa') + \ldots, \quad (2.7)$$

with

$$\phi_\alpha(l\kappa) = \frac{\partial \phi}{\partial u_\alpha(l\kappa)}|_0 \tag{2.8a}$$

$$\phi_{\alpha\beta}(l\kappa; l'\kappa') = \left.\frac{\partial^2 \phi}{\partial u_\alpha(l\kappa)\, \partial u_\beta(l'\kappa')}\right|_0, \tag{2.8b}$$

where the subscript 0 means that the derivatives are evaluated at the equilibrium configuration; $\phi_0 = E^{\text{elec}}(\mathbf{x})$ is the static equilibrium potential energy of the crystal; $\phi_\alpha(l\kappa)$ is the gradient of potential energy (-1 force) that acts on atom κ in the direction $\alpha = x, y, z$ and vanishes at the equilibrium configuration; and $\phi_{\alpha\beta}(l\kappa; l'\kappa')$ is the interatomic force constants matrix given by the second derivative of the potential energy with regard to atomic displacement. This coefficient gives the negative force that exerted on atom $(l\kappa)$ in the Cartesian direction α when the atom at $(l'\kappa')$ is displaced in the direction β by a small distance, and all other atoms are in their equilibrium positions. This is called the harmonic approximation; it approximates the potential energy surface as a quadratic function of the ionic displacements. The high-order terms of expansion are neglected within the harmonic approximation [8, 115].

The classical harmonic vibrational Hamiltonian for the system with N number of atoms per unit cell can be written as

$$H = \phi_0 + \frac{1}{2}\sum_{l\kappa\alpha} M_\kappa \dot{u}_\alpha^2(l\kappa) + \frac{1}{2}\sum_{\substack{l\kappa\alpha \\ l'\kappa'\beta}} \phi_{\alpha\beta}(l\kappa; l'\kappa') u_\alpha(l\kappa) u_\beta(l'\kappa'), \tag{2.9}$$

where M_κ is the mass of atom κ. The classical equation for the motion of the lattice is

$$M_\kappa \ddot{u}_\alpha(l\kappa) = -\frac{\partial \phi}{\partial u_\alpha(l\kappa)} = -\sum_{l'\kappa'\beta} \phi_{\alpha\beta}(l\kappa; l'\kappa') u_\beta(l'\kappa'). \tag{2.10}$$

This equation is composed of an infinite homogeneous set of coupled linear differential equations. Eq. (2.8b), indicates that $\phi_{\alpha\beta}(l\kappa; l'\kappa')$ satisfies the symmetry condition

$$\phi_{\alpha\beta}(l\kappa; l'\kappa') = \phi_{\beta\alpha}(l'\kappa'; l\kappa). \tag{2.11}$$

Lattice periodicity dictates that the lattice must coincide with itself if it is translated relative to itself by a lattice vector $\mathbf{R}_l$. This indicates that $\phi_{\alpha\beta}(l\kappa; l'\kappa')$ does

not depend on l and l' separately but on the relative positions of cells l and l'. Furthermore, the translation of the entire system by the arbitrary constant amount $\mathbf{u}(l\kappa) = \mathbf{d}$, in which all atoms are displaced from their equilibrium position by $\mathbf{d}$, will not change the potential energy. This can be expressed as

$$\begin{aligned} \sum_{l\kappa} \phi_\alpha(l\kappa) &= 0 \\ \sum_{\substack{l\kappa\alpha \\ l'\kappa'\beta}} \phi_{\alpha\beta}(l\kappa; l'\kappa') &= 0. \end{aligned} \tag{2.12}$$

The general solution of the equation of motion (Eq. [2.10]), as below for $\mathbf{u}(l\kappa)$ is a superposition of harmonic travelling waves with various wavevectors $\mathbf{k}$ in the BZ and mode label j [116], where

$$\mathbf{u}(l\kappa) = \sum_{k,j} \mathbf{u}_{jk}(\kappa) \exp(i[\mathbf{k}\cdot\mathbf{R}_l - \omega_j(k)t]), \tag{2.13}$$

where $\mathbf{u}_{jk}(\kappa)$ is the displacement vector independent of unit cell l, because according to Bloch's theorem, the displacements on different lattice sites differ only by the phase factors. Substituting Eq. (2.13) in Eq. (2.10), the vibrational problem is reduced from the infinite set of equations of motion to a set of 3N linear homogeneous equations in 3N unknowns $\mathbf{u}_{jk}(\kappa')$:

$$M_\kappa\ \omega_j^2(\mathbf{k})\ \mathbf{u}_{j\mathbf{k}}(\kappa) = \sum_{l'\kappa'\beta} \phi_{\alpha\beta}(l\kappa; l'\kappa')\ \mathbf{u}_{j\mathbf{k}}(\kappa')\ \exp[i\mathbf{k}\cdot(\mathbf{R}_l - \mathbf{R}_{l'})]. \tag{2.14}$$

where N is the number of atoms in the primitive cell. Consider a periodic crystal of volume $V = L_1 \times L_2 \times L_3$ and N_p unit cells. Applying the Born–von Karman periodic boundary condition, in which $\mathbf{u}(l + L_i a_i) = \mathbf{u}(l)$ for each of the primitive lattice vectors a_i, restrict the allowed values of the wave vectors $\mathbf{k}$ to a set of discrete values

$$\mathbf{k}_i = \frac{h_i}{L_i}\mathbf{b}_i, \qquad h_i =, 0, .., L_i - 1, \quad i = 1, 2, 3\ , \tag{2.15}$$

where $\mathbf{b}_i$ are reciprocal lattice vectors that satisfy $\mathbf{b}_i \cdot \mathbf{a}_i = 2\pi\delta_{ij}$. This results in the decoupling of the motion equations at different $\mathbf{k}$ vectors. Now, the equations of motion can be written in the compact form

$$\omega_j^2(\mathbf{k})\mathbf{u}_{jk}(\kappa) = \sum_{\kappa'} D(\kappa\kappa'|\mathbf{k})\mathbf{u}_{jk}(\kappa'), \tag{2.16}$$

where $D_{\alpha\beta}$ is the element of the mass-reduced Fourier–transformed–dynamical matrix of the force constants that is given by

$$D_{\alpha\beta}(\kappa\kappa'|\mathbf{k}) = (M_\kappa M_{\kappa'})^{-\frac{1}{2}} \sum_l \phi_{\alpha\beta}(l\kappa; l'\kappa') \ \exp(i\mathbf{k}\cdot[\mathbf{R}_l - \mathbf{R}_{l'}]), \tag{2.17}$$

where $\exp(i\mathbf{k}\cdot[\mathbf{R}_l - \mathbf{R}_{l'}])$ is the phase factor that represents any atomic wave motion. For each wave vector $\mathbf{k}$, the solution of Eq. (2.16) can be obtained by solving the secular equation

$$\det|\ D_{\alpha\beta}(\kappa\kappa'|\mathbf{k}) - \omega_j^2(\mathbf{k})\ \delta_{\alpha\beta}\ \delta_{\kappa\kappa'}\ | = 0, \tag{2.18}$$

which yields a set of $3N$ independent harmonic oscillators (branches) each corresponding to an eigenvector $\mathbf{e}(\kappa|\mathbf{k}j)$. The frequencies $\omega = \omega_j(\mathbf{k})$, $j = 1, 2, \ldots, 3N$ are known as the dispersion curves. Following from Eq. (2.17) and using Eq. (2.11), it can be seen that

$$D_{\beta\alpha}(\kappa'\kappa|\mathbf{k}) = D^*_{\alpha\beta}(\kappa\kappa'|\mathbf{k}). \tag{2.19}$$

Thus, the dynamical matrix is Hermitian, and its eigenvalues $\omega_j^2(\mathbf{k})$ are always real. The equation of motion can be expressed in vector form as

$$\omega_j^2(\mathbf{k})\mathbf{e}(\kappa|\mathbf{k}j) = \sum_{\kappa'} D(\kappa\kappa'|\mathbf{k})\mathbf{e}(\kappa'|\mathbf{k}j) \tag{2.20}$$

The eigenvalues of the dynamical matrix give the squares of the normal mode frequencies $\omega_j(\mathbf{k})$, and the eigenvectors $\mathbf{e}(\kappa'|\mathbf{k}j)$ are known as polarisation vectors that give the pattern of atomic displacement and consist of the displacement vector weighted by the square root of the atomic mass. The use of these mass-weighted variables in the equation of motion (Eq. [2.20]) allows us to find a solution for ω^2 instead of $M_\kappa\omega^2$. Therefore, the eigenvectors should be chosen to satisfy the orthonormality condition, where

$$\sum_\kappa \mathbf{e}^\dagger(\kappa|\mathbf{k}j)\mathbf{e}(\kappa|\mathbf{k}j') = \delta_{jj'}. \tag{2.21}$$

Moreover, Eq. (2.17), indicates that

$$D_{\alpha\beta}(\kappa\kappa'|-\mathbf{k}) = D^*_{\alpha\beta}(\kappa\kappa'|\mathbf{k}), \tag{2.22}$$

which implies that the dynamical matrix is a symmetric matrix. Similarly, taking the complex conjugate of Eq. (2.20), where $\omega_j^2(\mathbf{k})$ is always real, we can state that

$$\mathbf{e}(\kappa'|\mathbf{k}j) = \mathbf{e}^*(\kappa'|-\mathbf{k}j) \tag{2.23}$$

and that due to the time–reversal symmetry,

$$\omega_j^2(\mathbf{k}) = \omega_j^2(-\mathbf{k}). \tag{2.24}$$

Furthermore, the solutions of Eq. (2.20) describe collective modes or excitations as a complete set of linearly independent (orthogonal) atomic motions associated with each wave. These motions are complex in general. Real displacement patterns can be evaluated by taking the real and imaginary parts, which corresponde to linear combinations of the eigenvectors at $+\mathbf{k}$ and $-\mathbf{k}$ [8, 115].

We can simplify the problem further by formulating the harmonic Hamiltonian in terms of a new set of coordinates—normal coordinates $q_{j\mathbf{k}}$ that are linked to the atomic displacements $\mathbf{u}(l\kappa)$ through the expressions

$$q_{j\mathbf{k}} = \frac{1}{\sqrt{N_\mathrm{p}}} \sum_{l,\kappa} \sqrt{M_\kappa}\mathbf{e}^\dagger(\kappa|\mathbf{k}j)\mathbf{u}(l\kappa)e^{-i\mathbf{k}\cdot\mathbf{R}_l}, \tag{2.25}$$

$$\mathbf{u}(l\kappa) = \frac{1}{\sqrt{N_\mathrm{p}M_\kappa}} \sum_{\mathbf{k},j} \mathbf{e}(\kappa|\mathbf{k}j)q_{j\mathbf{k}}e^{i\mathbf{k}\cdot\mathbf{R}_l}, \tag{2.26}$$

where N_p is the number of primitive unit cells, which is chosen to be equal to the number of wave vectors that are commensurate with lattice supercell, and $q_{j\mathbf{k}}$ is the normal coordinate of branch j at wavevector $\mathbf{k}$. Eq. (2.26), indicates that the collective atomic displacement is the superposition of normal mode motions weighted by coefficients $\mathbf{e}(\kappa|\mathbf{k}j)e^{i\mathbf{k}\cdot\mathbf{R}_l}$. The total number of normal–mode frequencies in the crystal is $3N_pN$, in which all the atoms at each frequency vibrate with the same phase. Accordingly, the normal mode coordinate $q_{j\mathbf{k}}$ gives an independent description of the crystal vibration mode with one normal–mode frequency $\omega_j(\mathbf{k})$.

In view of these definitions, the classical Hamiltonian of the lattice as a function of the normal coordinates [115] is

$$H_\mathrm{vib} = \frac{1}{2}\sum_{\mathbf{k}j}\left[\dot{q}_{j\mathbf{k}}^2 + \omega_j^2(\mathbf{k})q_{j\mathbf{k}}^2\right]. \tag{2.27}$$

This Hamiltonian is a summation of terms for noninteracting (uncoupled) simple harmonic oscillators, each of which corresponds to a normal mode $\omega_j(\mathbf{k})$ of the lattice. Thus far, we have formulated discussions in terms of classical mechanics.

2.2.2.1 Quantisation of normal modes

In the landscape of the BO approximation, the nuclei are heavy classical particles that perform small vibrations around their respective equilibrium positions. Never-

theless, a nuclear subsystem must be viewed as a quantum system and described by a wave function whose square modulus defines the probability density of the nuclear locations. For the given vibrational state, the mean value of these calculated nuclear coordinates can be observed experimentally. The complete quantum description of the nuclei is thus given by the Schrödinger equation for the nuclei. The vibrational Schrödinger equation for the mode $j\mathbf{k}$ can be written as

$$\left[-\frac{1}{2}\frac{\partial^2}{\partial q^2}+\frac{1}{2}\omega_j^2(\mathbf{k})q^2\right]\psi_{nj\mathbf{k}}(q)=\mathcal{E}_{nj}(\mathbf{k})\psi_{nj\mathbf{k}}(q), \tag{2.28}$$

with the corresponding well-known solution

$$\psi_{nj\mathbf{k}}(q)=\left(\frac{\sqrt{\omega_j(\mathbf{k})}}{\pi^{\frac{1}{2}}2^n n!}\right)^{1/2} e^{-\frac{1}{2}\omega_j(\mathbf{k})q^2}H_n\left(\sqrt{\omega_j(\mathbf{k})}q\right), \tag{2.29}$$

where n is the occupation number of the normal vibrational mode, H_n is the nth Hermite polynomial, and $\mathcal{E}_{nj}(\mathbf{k})$ is the total energy of the nth excited state of branch j at $\mathbf{k}$ given by the discrete set of values

$$\mathcal{E}_{nj}(\mathbf{k})=\left(n+\frac{1}{2}\right)\omega_j(\mathbf{k}), \qquad n=0,1,2,\ldots. \tag{2.30}$$

Because the Hamiltonian is separable, the overall vibrational wave function can be written as a simple product of single-oscillator wave functions

$$\Psi_n=\prod_{j\mathbf{k}}\psi_{nj\mathbf{k}}(q). \tag{2.31}$$

The classical term 'normal' mode is replaced with analogous term 'Phonon', which is used to describe the quanta of the ionic displacement field. Phonons are boson quasiparticles, with a symmetric wave function under particle exchange, which can exist in the same state at the same time, unlike fermions, which are subject to Pauli's exclusion principle. Phonons adhere to Bose–Einstein statistics, whereby the expected number of phonons in a particular vibrational state is determined by

$$n_{\mathrm{B}}(\omega_{\mathbf{k}j},T)=[\exp\omega_j(\mathbf{k})/k_BT)-1]^{-1}, \tag{2.32}$$

where k_B is the Boltzmann constant.

2.3 The vibrational renormalisation of the band gap

First-principles techniques have been used mainly to calculate physical properties within the static lattice approximation, in which the electronic Schrödinger equation is solved with fixed nuclear positions under the BO approximation. In particular, this is the case for calculations of electronic band gaps because of the difficulty of describing electron–phonon interactions [79, 100]. However, nuclear motion due to both thermal and quantum effects alters the electronic band structure of crystalline materials by altering the equilibrium lattice parameters [117] and by providing a distribution of nuclear positions within each unit cell [76, 77].

In this section, we will discus the vibrational renormalisation of band gap energy. Calculating the band gap requires a determination of the electron's transitions (*excitations*) energy from the valence band to the conduction band. Because electronic transitions are instantaneous on the timescale of nuclear motion, vibrationally renormalised electronic excitation energies are obtained by averaging excitation energies over the distribution of nuclear coordinates in the initial electronic state. Such vibrational renormalisations of optical and excitonic gaps are approximately equal to the effects of including vibrational free energies in quasiparticle bands. The resulting zero–point renormalisation of the band gap, therefore, is sizeable enough to be comparable to the size of the thermal shift of the band gap at room temperature.

2.3.1 The nuclear thermal average

From the theory of statistical mechanics, it is straightforward to apply general formulas to show that the equilibrium distribution of the nuclear configurations can be treated within Boltzmann quantum statistics. Assuming that the nuclei are distinguishable particles, the probability that a given vibrational state s with energy E_s will be occupied can be determined by Boltzmann or Gibbs distribution, as

$$P(E_s) = \frac{1}{Z} \exp\left(-\beta E_s\right), \tag{2.33}$$

where $\beta = 1/(k_{\mathrm{B}}T)$ is the reciprocal temperature, T is temperature, k_{B} is Boltzmann's constant and Z is the normalisation factor, known as the partition function and defined as

$$Z = \sum_{s} \exp\left(-\beta E_s\right). \tag{2.34}$$

For a quantum system with many particles, the thermal density matrix operator (or thermal propagator) $\hat{\rho}$ with a basis of a complete set of eigenstates Ψ_i of $\hat{H}$ can be written as

$$\hat{\rho} \equiv e^{-\beta \hat{H}} = \sum_{i} |\Psi_i\rangle e^{-\beta E_i} \langle \Psi_i|. \tag{2.35}$$

The probability of state i with eigenstates ψ_i of $\hat{H}$ can be written as

$$\rho_i \equiv \langle \Psi_i|\hat{\rho}|\Psi_i\rangle = \frac{1}{Z} \exp\left(-\beta E_i\right). \tag{2.36}$$

We can thus write the quantum expression for the canonical partition function as

$$Z = \sum_{i} \langle \Psi_i|\hat{\rho}|\Psi_i\rangle = \mathrm{Tr}[\hat{\rho}]. \tag{2.37}$$

Therefore, the thermal average of any quantum operator A can be easily expressed using the density matrix ρ:

$$A(T) = \langle A\rangle_T = \frac{1}{Z} \sum_{i} \langle \Psi_i|A|\Psi_i\rangle e^{-\beta E_n} \tag{2.38}$$

$$= \frac{1}{Z} \mathrm{Tr}[\rho A] = \frac{\mathrm{Tr}[\hat{\rho} A]}{\mathrm{Tr}[\hat{\rho}]}. \tag{2.39}$$

During the optical transitions between the initial and final states, the system must satisfy the Franck-Condon (FC) principle [118], in which the time required for an optical transition between vibrational sublevels of two electronic states is substantially less than the time required for the lattice to relax at a constant distance between nuclei. Following this scheme, let the BO potential energy surfaces in the electronic ground state and some particular electronic excited state be $V_0(\mathbf{R})$ and $V_m(\mathbf{R})$, respectively. Let the corresponding distributions of nuclear coordinates be $p_0(\mathbf{R})$ and $p_m(\mathbf{R})$, respectively. Thus, at finite temperature, it is convenient to write a general formula of these distributions, which arise due to both thermal and quantum effects, according to the canonical Boltzmann distribution. Assuming that

the system is in a particular electronic state i, the canonical distribution function for the nuclear configuration $\mathbf{R}$ can be written as [1]

$$\begin{aligned} p_i(\mathbf{R}) &= \frac{\mathrm{Tr}\left[|\mathbf{R}\rangle\langle\mathbf{R}|\exp\left(-\beta\hat{H}_i\right)\right]}{\mathrm{Tr}\left[\exp\left(-\beta\hat{H}_i\right)\right]} \\ &= \frac{\sum_n |\Psi_{n,i}(\mathbf{R})|^2 \exp\left(-\beta E_{n,i}\right)}{\sum_n \exp\left(-\beta E_{n,i}\right)}, \end{aligned} \tag{2.40}$$

where $\hat{H}_i$ is the nuclear Hamiltonian for the BO potential energy surface $V_i(\mathbf{R})$ and $E_{n,i}$ and $\Psi_{n,i}(\mathbf{R})$ are the energy eigenvalues and eigenfunctions of $\hat{H}_i$. The trace operation refers to the sum over all the states of the system with a given number of particles. The index $i = 0, 1, ..$ is here used to identify one electronic state for different nuclear configurations $\mathbf{R}$, and n is the entire set of associated vibrational quantum states.

Using Eq. (2.38), the vibrational average of an observable $A(\mathbf{R})$ can be written as

$$\hat{A}(T) = \frac{1}{Z_i}\sum_n \langle\Psi_{n,i}(\mathbf{R})|\hat{A}(\mathbf{R})|\Psi_{n,i}(\mathbf{R})\rangle e^{-\beta E_{n,i}}. \tag{2.41}$$

This expression can be clearly related to the FC principle [118], which evaluates the thermal average where the electron transition between electronic states $i \to i'$ (i.e. excitations) are allowed at the instantaneous frozen nuclear configuration $\mathbf{R}$. Thus, at every temperature, even absolute zero, the atoms in a crystalline solid can be seen as frozen but randomly displaced from their equilibrium lattice sites, resulting in a distribution of electronic excitation energies with a mean value that differs from the static-nucleus gap.

The adiabatic BO approximation can be invoked by restricting the electronic wave function to a single electronic state in the BO approximation, typically the ground electronic state. Hence, Eq. (2.41) is reduced to considering only the electronic–ground state, expressed as

$$\hat{A}(T) = \frac{1}{Z_0}\sum_n \langle\Psi_{n,0}(\mathbf{R})|\hat{A}(\mathbf{R})|\Psi_{n,0}(\mathbf{R})\rangle e^{-\beta E_{n,0}}, \tag{2.42}$$

where $Z_0 = \sum_n e^{-\beta E_{n,0}}$, and where $E_{n,0}$ and $\Psi_{n,0}(\mathbf{R})$ are the nuclear eigenvalues and eigenfunction in the BO ground electronic states. Using the form of the harmonic

[1] The trace operator is re-expressed on the basis of the nuclear degrees of freedom because it is invariant regarding the basis set choice.

eigenfunction defined in Eq. (2.29), the harmonic vibrational thermal average can be rewritten as

$$\hat{A}(T) = \frac{1}{Z_0} \sum_n \int d\mathbf{R} |\Psi_{n,0}|^2 \hat{A}(\mathbf{R}) e^{-\beta E_{n,0}}. \tag{2.43}$$

The vibrational thermal average in Eq. (2.42) has been evaluated in the literature using the quadratic approximation, known as Allen–Heine–Cardona theory [76, 77], molecular dynamics, path integral molecular dynamics [89] and Monte Carlo methods [92, 93]. In this work, the vibrationally renormalised expectation value is evaluated using the random sampling algorithm, as described in Sec. 2.4.

2.3.2 Band–gap renormalisation

Within the adiabatic approximation, the quantum and thermal effect of lattice fluctuations on physical properties can by demonstrated by simulating the harmonic atomic motion. At a particular nuclear configuration $\mathbf{R}$, the lattice is almost frozen during electron transitions between initial and final states. Using the previous definitions in Sec. 2.3.1, we can now address the vibrational renormalisation of the band gap for the system at a finite temperature from two different perspectives.

2.3.2.1 Optical absorption and emission gaps

In studying the fundamental physical properties of semiconductor materials, the optical simulation of electron excitations across the band gap from the occupied state into the unoccupied state is crucially important [119–121]. The electronic transitions between the ground state and excited state are assumed to be dipole-allowed. During the interaction of radiation with matter, the system undergoes a series of transformations that include absorption and emission, accompanied by changes in the state of the system. For an equilibrium system, the electron transitions start whenever the absorbed or emitted photon energy is equal to the energy gap between the valence and conduction band. Such inter-band transitions can provide the desired absorption (emission) edge to calculate the static-nucleus absorption $\Delta_{\text{abs}}^{\text{static}}$ and emission gaps $\Delta_{\text{em}}^{\text{static}}$ as follows:

$$\Delta_{\text{abs}}^{\text{static}} = V_1(\mathbf{R}_0) - V_0(\mathbf{R}_0) \tag{2.44}$$

$$\Delta_{\mathrm{em}}^{\mathrm{static}} = V_1(\mathbf{R}_1) - V_0(\mathbf{R}_1), \tag{2.45}$$

where $\mathbf{R}_0$ and $\mathbf{R}_1$ are the equilibrium nuclear configurations in the electronic ground state and excited state, respectively.

Thus far, we have referred mainly to the optical transitions of electrons between electronic or quasiparticle states. However, these transitions are subject to thermal shifts induced by the interaction of electrons with the lattice. According to the FC principle, the radiative (optical–induced) electronic transitions (absorption or emission) between initial and final levels are assumed to occur while maintaining the atomic configurations characteristic of the initial state, so the energy of a photon that is absorbed or emitted at nuclear configuration $\mathbf{R}$ is equal to the energy gap $V_1(\mathbf{R}) - V_0(\mathbf{R})$. The nuclear configuration $\mathbf{R}$ fluctuates in time and in space throughout the crystal, so that the electronic transition of interest gives rise to a distribution of photon absorption and emission peaks. If the FC approximation is valid and the absorption or emission bands are narrow, such that we can meaningfully identify a peak corresponding to the electronic transition of interest, the distribution of photon energies is well characterised by its mean [76, 77].

The mean optical absorption gap is

$$\Delta_{\mathrm{abs}} = \int [V_1(\mathbf{R}) - V_0(\mathbf{R})]\, p_0(\mathbf{R})\, d\mathbf{R}. \tag{2.46}$$

Likewise, the mean emission gap is

$$\Delta_{\mathrm{em}} = \int [V_1(\mathbf{R}) - V_0(\mathbf{R})]\, p_1(\mathbf{R})\, d\mathbf{R}. \tag{2.47}$$

The vibrational renormalisation corrections of the absorption and emission gaps can be now calculated as $\Delta_{\mathrm{abs}}^{\mathrm{static}} - \Delta_{\mathrm{abs}}$ and $\Delta_{\mathrm{em}}^{\mathrm{static}} - \Delta_{\mathrm{em}}$. In principle, vibrational renormalisation can be of either sign; in practice, for the commonly encountered situation in which the excited-state BO potential energy surface has a shallower minimum than the ground state, renormalisation is negative. For a situation in which the Stokes shift $\Delta_{\mathrm{abs}} - \Delta_{\mathrm{em}}$ is small, we simply refer to vibrational renormalisation of the optical gap. However, the FC approximation breaks down in any material that exhibits a significant Stokes shift, meaning that the optical absorption and emission gaps differ significantly. This typically arises from a large difference between the equilibrium nuclear configurations $\mathbf{R}_0$ and $\mathbf{R}_1$ in the electronic

ground and excited states caused by the lattice relaxation between the electron excitation and the subsequent emission transitions.

2.3.2.2 Electron addition and removal gaps

In the static-nucleus approximation, the atoms are fixed at their equilibrium configurations $\mathbf{R}$, in which both the nuclear and electronic entropies are neglected. The static-nucleus quasiparticle gap may thus be evaluated as

$$\Delta_{\mathrm{qp}}^{\mathrm{static}} = E_I - E_A = V_+(\mathbf{R}_+) + V_-(\mathbf{R}_-) - 2V_0(\mathbf{R}_0), \tag{2.48}$$

where $E_I = V_-(\mathbf{R}_-) - V_0(\mathbf{R}_0)$ is the ionisation potential and $E_A = V_0(\mathbf{R}_0) - V_+(\mathbf{R}_+)$ is the electron affinity. $\mathbf{R}_\pm$ is the equilibrium nuclear configurations of the system with one additional and one fewer electron, respectively. Under conditions of constant pressure, V_0 and $V_\pm$ are Gibbs free energies. The atomic structure is allowed to relax after the addition or removal of an electron, resulting in a small contribution to the static–nucleus ionisation potential and electron affinity. However, this contribution largely cancels out the static–nucleus quasiparticle gap. Likewise, the static-nucleus excitonic gap can be calculated as

$$\Delta_{\mathrm{ex}}^{\mathrm{static}} = V_1(\mathbf{R}_1) - V_0(\mathbf{R}_0). \tag{2.49}$$

In the vertical excitations of an electron, the equilibrium nuclear coordinates of the excited state are assumed to be the same as that of the ground state. Within this assumption, the static-nucleus excitonic gap is equal to the static-nucleus optical absorption and emission gaps.

During thermodynamic calculations (for occupancies of excited states and transport calculations, etc.), the thermal shift of electronic energy levels due to the lattice vibrations can be understood as the free energy differences upon electronic excitation [122, 123] rather than the average of a gap over nuclear coordinates. Therefore, at a given temperature and system volume, the shift in the energy of a nearly empty conduction band is $\mathcal{E} = F_+ - F_0$, where F_0 is the Helmholtz free energy of the system in the electronic ground state and F_+ is the Helmholtz free energy in the presence of an additional electron in a specified state. Likewise, the shift in the energy of a filled valence band is $\mathcal{E} = F_0 - F_-$, where F_- is the Helmholtz free

energy of the system with an electron removed. The quasiparticle gap is

$$\Delta_{\mathrm{qp}} = F_{+} + F_{-} - 2F_{0}, \tag{2.50}$$

which is the difference between the conduction-band minimum and valence-band maximum. In a similar way, we can define an excitonic gap

$$\Delta_{\mathrm{ex}} = F_{1} - F_{0} \tag{2.51}$$

as the change in free energy when an electron is excited. In semiconductor materials, the difference between Δ_{qp} and Δ_{ex} is the exciton binding energy. The vibrational renormalisation corrections of the quasiparticle gap and excitonic gap can be evaluated as $\Delta_{\mathrm{qp}} - \Delta_{\mathrm{qp}}^{\mathrm{static}}$ and $\Delta_{\mathrm{ex}} - \Delta_{\mathrm{ex}}^{\mathrm{static}}$, respectively.

2.3.2.3 Brooks' theorem

Based on the previous discussion, the vibrational effects in quasiparticle and excitonic gaps have different physical origins to those of the vibrational renormalisation of optical absorption and emission gaps. Nevertheless, these two viewpoints are brought together by Ref. [124] as Brooks' theorem [122]. According to Brooks' theorem, the thermal shift in electronic energy levels arises when the change in the phonon occupancy is equal to the thermal shift of phonon energies resulting from changes in electronic occupancy. In other words, the effects of electron–phonon interactions on the electronic band structure of solids can be computed by renormalising either the phonons or the electrons. As the electronic transitions occur at fixed nuclear coordinates, each configuration $\mathbf{R}$ yields an energy gap equal to $U(\mathbf{R}) = V_1(\mathbf{R}) - V_0(\mathbf{R})$ and a probability, defined by the nuclear wave function as $|\Psi_{n,0}(\mathbf{R})|^2$, that is assumed to be populated according to the Boltzmann distribution Eq.(2.36). The thermal average of the optical absorption gap can be calculated as an expectation value:

$$\Delta_{\mathrm{abs}} = \langle \Psi_{n,0}(\mathbf{R}) | U(\mathbf{R}) | \Psi_{n,0}(\mathbf{R}) \rangle. \tag{2.52}$$

Considering $U(\mathbf{R})$ as a small perturbation, we can now apply the first–order perturbation theory to the optical absorption gap in Eqs. (2.46) as follows:

$$\begin{aligned}\Delta_{\text{abs}} &= \sum_n \frac{e^{-\beta E_{n,0}}}{Z_0} \int \left[V_1(\mathbf{R}) - V_0(\mathbf{R})\right] \left|\Psi_{n,0}(\mathbf{R})\right|^2 \, d\mathbf{R} \\ &\approx \sum_n \frac{e^{-\beta E_{n,0}}}{Z_0} \left(E_{n,1} - E_{n,0}\right) + O(V_1 - V_0)^2. \end{aligned} \tag{2.53}$$

For the optical gap, an analogous form of the thermal average of a band gap over the initial–state ensemble can be written in terms of the Helmholtz free energy [123]. At constant pressure P and finite temperature T, the thermal probability that a system with volume Ω will promote an electron from the ground state to the first excited state is

$$p_{0n} = \exp\left[\beta(F_0 - E_{n,0} - P\Omega)\right], \tag{2.54}$$

where F_0 is the ground–state Helmholtz free energy. The Helmholtz free energy can be expressed in terms of the partition function in the canonical ensemble as

$$F_i = -\frac{1}{\beta} \ln Z_i. \tag{2.55}$$

The thermal average of the excitonic gap Eq. (2.51) can be calculated as

$$\begin{aligned}\Delta_{\text{ex}} &= \frac{-1}{\beta}\left[\ln(Z_1) - \ln(Z_0)\right] \\ &\approx \frac{1}{Z_0} \sum_n e^{-\beta E_{n,0}} \left(E_{n,1} - E_{n,0}\right) + O(V_1 - V_0)^2, \end{aligned} \tag{2.56}$$

where we have inserted a first-order Taylor expansion of $\ln(Z_1)$ in $E_{n,1} - E_{n,0}$, where $Z_1 = \sum_n e^{-\beta E_{n,1}} = \sum_n e^{-\beta E_{n,0}} e^{-\beta(E_{n,1} - E_{n,0})}$. Hence $\Delta_{\text{abs}} \approx \Delta_{\text{ex}}$. Likewise, $\Delta_{\text{em}} \approx \Delta_{\text{ex}}$. For materials in which the exciton–binding energy is negligible because excited quasiparticles are delocalized, the quasiparticle gap can be estimated to be equivalent to the excitonic gap and, therefore, the optical absorption and emission gaps. This result is sometimes referred to as Brooks' theorem. In a material with a large Stokes shift, Brooks' theorem is unlikely to hold because the optical absorption and emission gaps will not be in agreement with the excitonic gap. This results from a significant dissimilarity between the equilibrium nuclear configurations $\mathbf{R}_0$ and $\mathbf{R}_1$ in the electronic ground and excited states.

2.4 Method development

2.4.1 Neumann acceptance/rejection procedure

The expectation value of the band gap and any other properties with respect to the vibrations of the atoms in a solid at temperature T can be determined via MC sampling of the normal coordinates. Although the VMC technique is an elegant and straightforward approach to accurately sampling vibrational wave functions, the resulting atomic configurations are serially correlated. For independent normal modes, this issue can be avoided by using the Neumann acceptance/rejection procedure.

The energy of a normal mode of frequency ω is treated as a discrete random variable that occupies the harmonic-oscillator energy levels according to the Boltzmann distribution $p(n) = \frac{1}{Z} e^{-(n+\frac{1}{2})\omega\beta}$, where $\beta = \frac{1}{k_{\mathrm{B}}T}$, $Z = \sum_{n=0}^{\infty} e^{-(n+1/2)\omega\beta} = \frac{1}{2\sinh\left(\frac{\beta\omega}{2}\right)}$ is the canonical partition function, and k_{B} is Boltzmann's constant. This distribution specifies the probability that the normal mode will be in a particular vibrational quantum state n as a function of temperature. The inverse transform approach is used to sample randomly from the Boltzmann distribution the vibrational state n. This technique is as follows:

1. Generate a random number $u \in [0, 1)$ distributed according to the uniform probability distribution function.

2. Set $n = n'$ if $F(n' - 1) \leq u < F(n')$, where $F(n) = \sum_{n'=0}^{n} p(n')$ is the cumulative probability function. Equivalently, we may set $n = \mathrm{floor}(F^{-1}(u)) + 1$, where the inverse of F is

$$F^{-1}(u) = -\frac{1}{\beta\omega} \ln\left[1 - Zu\left(e^{\beta\omega/2} - e^{-\beta\omega/2}\right)\right] - 1. \tag{2.57}$$

The collective atomic displacements [Eq. (2.26)] are evaluated within the harmonic approximation by sampling the vibrational wave function [Eq. (2.29)]. The Neumann acceptance/rejection approach is an effective method for sampling from a complicated target distribution $f(q)$. This technique requires a comparison function $g(q)$ from which random values of q are drawn, which satisfies

$$f(q) \leq cg(q) \qquad \text{for all } q, \tag{2.58}$$

where $c \geq \sup[f(q)/g(q)]$ is a positive scaling factor that can be adjusted to ensure that the comparison function exceeds the entire target function.

2.4.1.1 Sampling the ground state

The harmonic oscillator's ground-state wave function, and hence the ground-state distribution of normal coordinates in each mode, is a simple Gaussian function. Hence, in the ground state, the normal coordinates for each mode can be sampled using the Box–Muller algorithm [125].

The target distribution $f(q)$, as shown in Fig. 2.1, is a harmonic-oscillator probability distribution:

$$f(q) =\mid \psi_0(q) \mid^2= (\frac{\alpha_j(\mathbf{k})}{\pi^{0.5}})e^{-\alpha_j^2 q^2}, \tag{2.59}$$

where $\alpha_j^2(\mathbf{k}) = \omega_j(\mathbf{k})$. The comparison function $g(q)$ is a normal distribution with the correct asymptotic behaviour for the harmonic oscillator probability distributions $f(q)$, allowing for efficient sampling of the tail of the $f(q)$. The probability density is given by

$$g(q) = \frac{\xi}{\sqrt{\pi}} e^{-\xi^2\ q^2}, \tag{2.60}$$

where ξ is a constant given by

$$\xi = \frac{1}{\sigma_g \sqrt{2}} = c_0\ \sigma_f. \tag{2.61}$$

Here c_0 is a positive real constant selected to guarantee that the comparison function covers the entire target distribution. The standard deviations of the Gaussian and harmonic–oscillator eigenfunctions are represented by σ_g and σ_f, respectively:

$$\sigma_f = \frac{1}{\alpha}\sqrt{\frac{2n+1}{2}} \quad \text{and} \quad \sigma_g = \sqrt{\frac{1}{2\omega_{j\mathbf{k}}}}, \tag{2.62}$$

in which the scaling constant c can be calculated for the ground state as

$$c = c_0 = \frac{\sigma_g}{\sigma_f}. \tag{2.63}$$

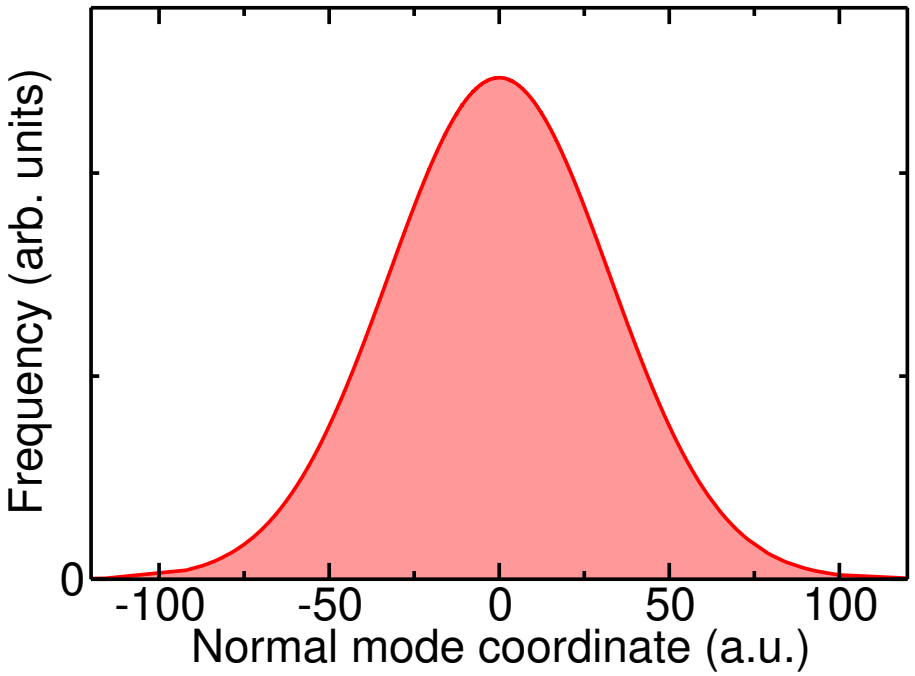

Figure 2.1: Histogram for sampling the vibrational normal coordinates of the ground state harmonic oscillator.

2.4.1.2 Sampling excited states

For the nth excited state of each normal mode, the target distribution $f(q)$ takes the form

$$f(q) = |\psi_n(q)|^2 = \frac{\sqrt{\omega}}{2^n n! \sqrt{\pi}} e^{-\omega q^2} H_n^2(\sqrt{\omega} q). \tag{2.64}$$

This is a multimodal distribution, with $n+1$ maxima. As Fig. 2.2 shows, an appropriate comparison function is

$$g(q) = \begin{cases} f_{\max} & \text{if } |q| \leq q_{\max} \\ f_{\max} \exp(-(|q| - q_{\max})^2/(2\sigma^2)) & \text{otherwise} \end{cases}, \tag{2.65}$$

where $\sigma = \sqrt{\frac{1}{2\omega_{j\mathbf{k}}}}$ is the standard deviation and $q_{\max}$ is the position of the maximum of the target distribution that is obtained using the cubic spline interpolation of the range of points $[0, q_0]$, where q_0 is the positive classical turning point at energy $(n+1/2)\omega$. For known $q_{\max}$, the $f_{\max} \equiv f(q_{\max})$ is the maximum value of the target function. We find that the comparison function [Eq. (2.65)], shown as the black curve in Fig. 2.2(b), spans the full range of our target distributions. We have verified that for a very large number of points q sampled from $g(q)$, in every case $g(q) \geq f(q)$.

In this method, the comparison function $g(q)$ is a combination of three distributions: two half-Gaussian functions and one uniform distribution in the range $[-q_{\max}, q_{\max}]$. Each distribution has an associated probability (a), so the overall $g(q)$ in the range $[-q_{\max}, q_{\max}]$ can be broken into a combination of three easily generated distributions g_1, g_2, and g_3. Let g_1 and g_2 be the left- and right-hand half Gaussians in Fig. 2.2, and let g_3 be the uniform distribution in the center. Then $a_1 = a_2 = \alpha\sqrt{2\pi}\sigma f_{\max}/2$ and $a_3 = 2\alpha f_{\max} q_{\max}$, where the constant α is determined by the normalization condition $a_1 + a_2 + a_3 = 1$. The random sampling method for the given harmonic excited state n is as follows.

1. Select one of the functions with probability a_i, where $\sum_i a_i = 1$, as follows:

   (a) Draw a random number s from a uniform distribution on $[0, 1)$.

   (b) **If** $s < a_1$ **then**
   {sample from $G = g_1$}
   else if $s < a_1 + a_2$ **then**
   {sample from $G = g_2$}
   else if $s < a_1 + a_2 + a_3$ **then**
   {sample from $G = g_3$}
   end if

2. Draw a random number X from the chosen function G using the Box-Muller transformation for g_1 and g_2 or the uniform probability distribution function for g_3.

3. Shift X by the mean of chosen distribution G and then calculate both $f(X)$ and $g(X)$.

4. Draw a random number Z from a uniform distribution on $[0, g(X))$.

5. If $Z < f(X)$, accept, and set $q = X$. Otherwise, return to step 1.

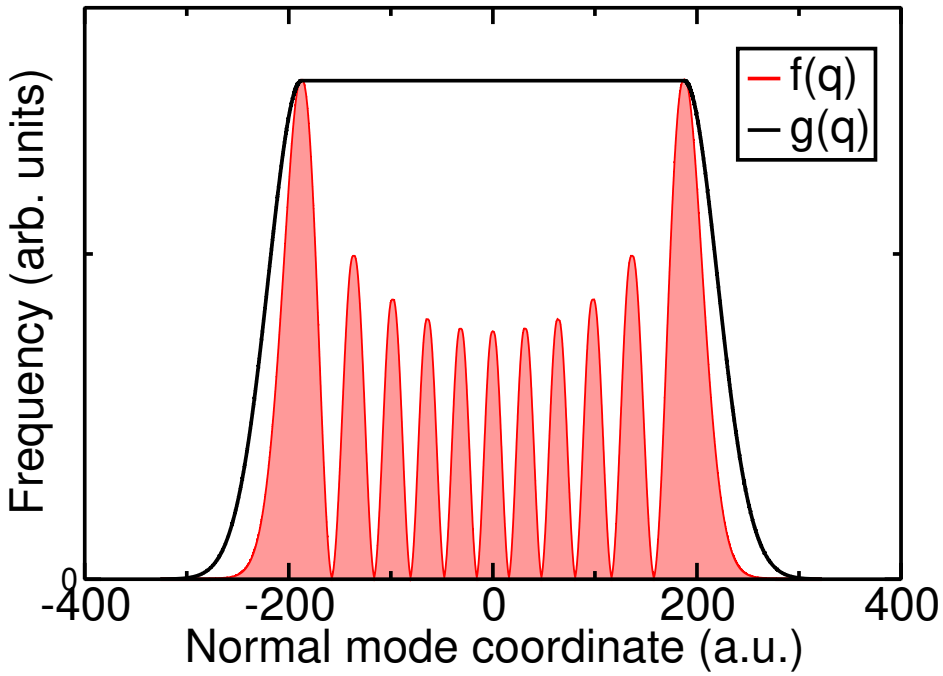

Figure 2.2: Histogram of the acceptance/rejection technique for sampling normal vibrational coordinates from the 10th excited state of the harmonic oscillator.

2.4.2 Unfolding the band structures of periodic systems

To investigate the effects of the vibrational motion of atoms on electronic band structures, calculations of excited electronic states in periodic supercells containing randomly sampled atomic configurations are performed. As we increase the system size, the representative supercell Brillouin zone (SCBZ) gets smaller, resulting in dense blocks of complicated electronic bands. To identify the valence and conduction bands, we need to unfold the hidden primitive cell character in supercell eigenstates. The supercell lattice vectors can be written as

$$\mathbf{a}_i^{\mathrm{s}} = \sum_j S_{ij} \mathbf{a}_j^{\mathrm{p}}, \tag{2.66}$$

where $\mathbf{a}_j^{\mathrm{p}}$ is the j^{th} primitive lattice vector and S_{ij} is a nonsingular integer matrix. The supercell defined by S contains $N_{\mathrm{p}} = |\det(S_{ij})| = \Omega_{\mathrm{s}}/\Omega_{\mathrm{p}}$ primitive cells, where Ω_{s} and Ω_{p} are the volumes of the supercell and primitive cell, respectively. In the case of non-degenerate static-nucleus states, unfolding the band structure would be a straightforward procedure by projecting the primitive-cell eigenvectors of a wavevector $\mathbf{k}_{\mathrm{p}}$ and band m onto all the folded supercell states $\Psi^{\mathrm{s}}_{n\mathbf{k}_{\mathrm{s}}}$ as $\langle \Psi^{\mathrm{p}}_{m\mathbf{k}_{\mathrm{p}}} | \Psi^{\mathrm{s}}_{n\mathbf{k}_{\mathrm{s}}} \rangle$, where the maximum overlap indicates the correct supercell band.

Consider a system in its static nuclear configuration, where the electronic states are g_n-fold degenerate or nearly degenerate, i.e. pseudodegeneracy. In this case, the orbitals in the supercell are identified by examining the overlap between the supercell orbital and the linear combination of primitive-cell degenerate orbitals. The primitive-cell eigenvector can be written in the form of a linear combination of degenerate states:

$$|\Psi^{\mathrm{p}}_{m\mathbf{k}_{\mathrm{p}}}\rangle = c_1\phi_1 + c_2\phi_2 + \cdots + c_{g_{\mathrm{n}}}\phi_{g_{\mathrm{n}}} = \sum_{i}^{g_n} c_i\phi_i, \tag{2.67}$$

subject to the orthonormality constraint

$$\langle\Psi^{\mathrm{p}}_{m\mathbf{k}_{\mathrm{p}}}|\Psi^{\mathrm{p}}_{m'\mathbf{k}_{\mathrm{p}}}\rangle = \delta_{mm'}\ , \tag{2.68}$$

where $\{c_i\}$ are linear coefficients that should be chosen to maximize the square modulus of the overlap between the supercell and primitive-cell eigenvectors. This can be done using the method of Lagrange multipliers:

$$\frac{\partial}{\partial c_i^*}\left[|\langle\Psi^{\mathrm{p}}_{m\mathbf{k}_{\mathrm{p}}}|\Psi^{\mathrm{s}}_{n\mathbf{k}_{\mathrm{s}}}\rangle|^2 - \lambda\sum_{i}^{g_{\mathrm{n}}}|c_i|^2\right] = 0, \tag{2.69}$$

leading to a set of equations

$$(\mathcal{A} - \lambda)\mathcal{C} = 0, \tag{2.70}$$

where λ is the eigenvalue, $\mathcal{C}$ is a vector of coefficients c_i, and $\mathcal{A}$ is an $g_{\mathrm{n}}\times g_{\mathrm{n}}$ Hermitian matrix given by

$$\mathcal{A} = \begin{pmatrix} |\langle\Psi^{\mathrm{s}}_{n\mathbf{k}_{\mathrm{s}}}|\phi_1\rangle|^2 & \langle\phi_1|\Psi^{\mathrm{s}}_{n\mathbf{k}_{\mathrm{s}}}\rangle\langle\Psi^{\mathrm{s}}_{n\mathbf{k}_{\mathrm{s}}}|\phi_2\rangle & \cdots & \langle\phi_1|\Psi^{\mathrm{s}}_{n\mathbf{k}_{\mathrm{s}}}\rangle\langle\Psi^{\mathrm{s}}_{n\mathbf{k}_{\mathrm{s}}}|\phi_{g_{\mathrm{n}}}\rangle \\ \langle\phi_2|\Psi^{\mathrm{s}}_{n\mathbf{k}_{\mathrm{s}}}\rangle\langle\Psi^{\mathrm{s}}_{n\mathbf{k}_{\mathrm{s}}}|\phi_1\rangle & |\langle\Psi^{\mathrm{s}}_{n\mathbf{k}_{\mathrm{s}}}|\phi_2\rangle|^2 & \cdots & \vdots \\ \vdots & \vdots & \ddots & \vdots \\ \langle\phi_{g_{\mathrm{n}}}|\Psi^{\mathrm{s}}_{n\mathbf{k}_{\mathrm{s}}}\rangle\langle\Psi^{\mathrm{s}}_{n\mathbf{k}_{\mathrm{s}}}|\phi_1\rangle & \cdots & \cdots & |\langle\Psi^{\mathrm{s}}_{n\mathbf{k}_{\mathrm{s}}}|\phi_{g_{\mathrm{n}}}\rangle|^2 \end{pmatrix}. \tag{2.71}$$

At this point, the constructed primitive-cell eigenvector Eq. (2.67) is used to perform the overlap with the supercell eigenvector. The solution of Eq. (2.70) can be obtained simply by using the `LAPACK` routine `zheev`. Figure 2.3 shows an example of the overlap results for unfolding the threefold degenerate valence and conduction bands at the center simulation cell of the static-nucleus Si $4\times4\times4$ supercell.

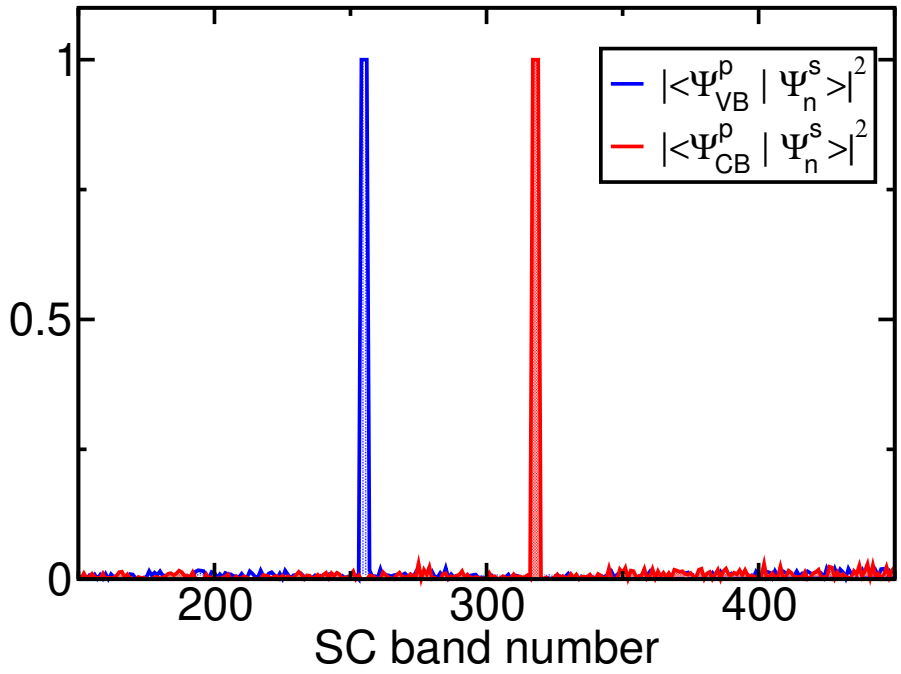

Figure 2.3: Square absolute overlap for unfolding the threefold degenerate valence and conduction bands at the Γ point of a $4 \times 4 \times 4$ supercell of the static-nucleus bulk Si.

For a periodic system with a plane wave basis set, the orbitals may be written as

$$\Psi_{n,\mathbf{k}}(\mathbf{r}) = \sum_{\mathbf{G}} C_{n,\mathbf{k}}(\mathbf{G}) \exp\left[i(\mathbf{k}+\mathbf{G})\cdot\mathbf{r}\right], \tag{2.72}$$

where $\mathbf{G}$ is a reciprocal lattice point, $\mathbf{k}$ is a Bloch wavevector that lies in the first Brillouin zone (BZ), n is the band index, and $C_{n,\mathbf{k}}$ is a Fourier coefficient. The supercell eigenstates are generally superpositions of the Bloch states of the underlying primitive cell. Therefore, a wavevector $\mathbf{k}_\mathrm{s}$ of the SCBZ is said to unfold into N_p wavevectors $\mathbf{k}_\mathrm{p}$ of the primitive-cell BZ (PCBZ) if there exists a set of N_p distinct reciprocal lattice points $\mathbf{G}^0_s$ of the supercell such that

$$\mathbf{k}_\mathrm{p} = \mathbf{k}_\mathrm{s} + \mathbf{G}^0_s. \tag{2.73}$$

The supercell reciprocal space with a mesh of $\mathbf{G}_\mathrm{s}$ that is compatible with the translational symmetry of the primitive cell can be remapped to PCBZ by matching the supercell and the primitive-cell Bloch basis functions that fulfill

$$\mathbf{k}_\mathrm{s} + \mathbf{G}_\mathrm{s} = \mathbf{k}_\mathrm{p} + \mathbf{G}_\mathrm{p}. \tag{2.74}$$

Substituting Eq. (2.73) into Eq. (2.74), the unfolded SC basis function is a

partial function with a subset of the supercell reciprocal lattice points ($\mathbf{G}'_{\mathrm{s}}$) that defined by

$$\mathbf{G}'_{\mathrm{s}} = \mathbf{G}_{\mathrm{p}} + \mathbf{G}^0_s, \tag{2.75}$$

at particular $\mathbf{k}_{\mathrm{p}}$, where all $\mathbf{G}_{\mathrm{s}}$ vectors that do not satisfy Eq. (2.74) are zeroed out. As a result, the supercell's basis function at $\mathbf{k}_{\mathrm{s}}$ can be decomposed into subsets of unfolded functions that correspond to Eq. (2.73) of the primitive cell. The unfolded supercell states can be written as

$$\Psi^{\mathrm{s}}_{n\mathbf{k}_{\mathrm{s}}} = \sum_{\mathbf{G}'_{\mathrm{s}}} C^{\mathrm{s}}_{n\mathbf{k}_{\mathrm{s}}}(\mathbf{G}'_{\mathrm{s}}) \exp\left[i(\mathbf{k}_{\mathrm{s}} + \mathbf{G}'_{\mathrm{s}}) \cdot \mathbf{r}\right] \ . \tag{2.76}$$

For greater efficiency, both $\mathbf{G}_{\mathrm{p}}$ and $\mathbf{G}_{\mathrm{s}}$ are sorted into stars of equal magnitude and then remapped within each star. Using the overlap procedure enables a full recovery of the hidden primitive-cell band structure of a system. This can be accomplished by projecting the primitive-cell Bloch states of a fixed $\mathbf{k}_{\mathrm{p}}$ that satisfy Eq. (2.73) onto all the unfolded supercell states:

$$\begin{aligned} \langle \Psi^{\mathrm{p}}_{m\mathbf{k}_{\mathrm{p}}} | \Psi^{\mathrm{s}}_{n\mathbf{k}_{\mathrm{s}}} \rangle &= \sum_{\mathbf{G}_{\mathrm{p}}} \sum_{\mathbf{G}'_{\mathrm{s}}} C^{\mathrm{p}*}_{m\mathbf{k}_{\mathrm{p}}}(\mathbf{G}_{\mathrm{p}}) C^{\mathrm{s}}_{n\mathbf{k}_{\mathrm{s}}}(\mathbf{G}'_{\mathrm{s}}) \Omega_{\mathrm{s}} \delta_{\mathbf{k}_{\mathrm{p}}+\mathbf{G}_{\mathrm{p}}, \mathbf{k}_{\mathrm{s}}+\mathbf{G}'_{\mathrm{s}}} \\ &= \Omega_{\mathrm{s}} \sum_{\mathbf{G}_{\mathrm{p}}} C^{\mathrm{p}*}_{m\mathbf{k}_{\mathrm{p}}}(\mathbf{G}_{\mathrm{p}}) C^{\mathrm{s}}_{n(\mathbf{k}_{\mathrm{p}}-\mathbf{G}^0_{\mathrm{s}})}(\mathbf{G}_{\mathrm{p}} + \mathbf{G}^0_{\mathrm{s}}), \end{aligned} \tag{2.77}$$

where the maximum overlap should indicate the correct band. For an ideal supercell structure with no degeneracy, the overlap procedure would identify the supercell states unambiguously.

2.4.3 Random selection method

Freezing in random lattice vibrations generally lowers the lattice symmetry to the trivial group that contains only the identity operation. Consequently, in most cases, the electronic-state degeneracy will be removed. Applying the band unfolding technique, we can determine an appropriate orbital in the supercell containing a randomly sampled atomic configuration by looking for the maximum overlap of each supercell orbital with the desired static-nucleus primitive-cell orbital (or set of degenerate primitive-cell orbitals). Effectively we assume that only one supercell orbital has a non-negligible overlap with the primitive-cell orbital of interest, and that the electron remains in that state as the nuclei move.

Alternatively, supercell orbitals may be identified using a random selection approach based on the square absolute overlap with the desired static-nucleus primitive-cell orbitals. These square absolute overlaps give the probabilities that an electron initially in the desired static-nucleus orbital ends up in the corresponding supercell orbitals, assuming an instantaneous change in the nuclear positions. Since the nuclei in fact move slowly on the electronic time-scale, it is more reasonable to use this MC approach to select between the $N = g_n$ supercell orbitals with the largest overlaps with g_n-fold degenerate static-nucleus primitive-cell orbitals.

The random selection method is as follows.

1. Let $y = \sum_{i=1}^{N} a(i)$ be a sum of the N squared absolute overlaps of target "offset" atomic configuration orbitals with the linear combination of the g_n-fold degenerate orbitals of the reference "static" atomic configuration.

2. Generate a random variable s taken uniformly from y.

3. **If** $s < a(1)$ **then**

   return {The random selected band is the band with square absolute overlap $a(1)$}

   else if $s < a(1) + a(2)$ **then**

   return {The random selected band is the band with square absolute overlap $a(2)$}

   ...

2.5 The optical band gap in single–particle–orbital theories

The excitonic (optical) gap is the energy at which the onset of absorption or emission of photons occurs. In an N-electron system, the optical gap can be written as the difference between the electron affinity (the amount of energy needed to create an anion from a neutral atom or molecule) and the ionisation energy (the amount of energy needed to remove an electron from its orbital). In first–principle calculations, this can be defined as the energy difference between the eigenvalue at the bottom of the conduction band (LUMO) and the eigenvalue at the top of the valence band

(HOMO). In the HF approximation, the excitation energy can be examined using Koopmans' theorem [126]. Assuming the orbitals are frozen, the orbitals of the remaining electrons cannot respond to the removed or added one. The ionisation energy (I) and electron affinity energy (A) are given by

$$\begin{aligned} I &= E_N - E_{N-1} \\ A &= E_{N+1} - E_N \ . \end{aligned} \tag{2.78}$$

In the HF approximation, the ionisation energies are relatively plausible, but the electron affinity energies are not, because the empty states are meaningless and unbounded, resulting in an overestimation of the predicted band gap. In addition, the HF theory is insufficient for making reliable predictions of band gaps because it neglects the electrons' correlation energy.

In DFT, the Kohn–Sham eigenvalues are evaluated as the derivatives of the total energy with respect to the occupation of a state:

$$\varepsilon_i = \frac{dE_{\text{total}}}{dn_i} = \int d\mathbf{r} \frac{dE_{\text{total}}}{dn(\mathbf{r})} \frac{dn(\mathbf{r})}{dn_i} \ . \tag{2.79}$$

This derivative is discontinuous due to the discontinuous nature of the exchange–correlation energy, which is a function of the density. Therefore, the HOMO–LUMO gap from the KS–DFT differs from the exact band gap. The DFT optical gap can be written as

$$\Delta_{\text{Ex}} = \varepsilon_g + \Delta_{xc} \ , \tag{2.80}$$

where ε_g is the KS eigenvalue band gap and Δ_{xc} is the additional contribution of the derivative discontinuity of the exchange–correlation energy. This well-known problem is called band-gap discontinuity. As a result of this discontinuity, the band gap is underestimated in the DFT calculations. Even with the exact KS eigenvalues obtained from a high-quality exchange–correlation function, the accuracy of the calculated gap remains questionable [127]. Because the reliability of DFT band–gap calculations has been questioned in recent years, the theory describing the vibrational renormalisation process should depend on accurate static gap calculations instead. Currently, the most accurate computations for gaps in materials are based on fixed-node DMC, in which the calculated energies are merely a function of the nodes of the many-body trial function.

2.6 Summary

In this chapter, we introduced a new method based on the random sampling of the vibrational normal coordinates from the nuclear wave functions. The incorporation of the classical treatment of ion displacements and the quantum treatment of electrons allows the efficient exploration of the configurational space within the adiabatic approximation. Furthermore, we developed an efficient method to unfold the electronic band structure with negligible computational expense, which takes into account the degeneracy of orbitals. In addition, we proposed the random selection approach based on the MC technique for determining the vibrational offset band structure. Using the proposed methods, the harmonic zero-point renormalisation and temperature-dependence of the optical gaps for a range of materials are presented in the next chapter within the QMC and DFT methods.

Chapter 3

Application of vibrational renormalisation of the band gap

In many materials with light atoms, the vibrational corrections of band gaps caused by the quantum effects of zero-point motion and temperature dependence are significant. The treatment of these effects on the electronic band structure has a long history. In the previous chapter, we gave a brief summary of current developments in this area, an outline of the theory, and a formal description of the proposed technique. In this chapter, at the harmonic level, we calculate the zero-point renormalisation of the band gap in molecular and crystalline systems using both the DFT and QMC calculations. In addition, we examine the temperature-dependent renormalisation of the direct band gap of benzene, silicon, and diamond arising from harmonic–disorder effects using our proposed method with first–principle DFT calculations.

3.1 Computational methodology

3.1.1 DFT calculations

3.1.1.1 Geometry optimisation, phonon calculations, and band-structure calculations

All of our DFT calculations were implemented using the CASTEP plane-wave-basis code [128]. These calculations were performed using the Perdew–Burke–Ernzerhof

(PBE) generalised gradient approximation and ultrasoft "on the fly" pseudopotentials [129] to represent the nuclei and core electrons, unless otherwise stated. For benzene, the geometry–relaxation, phonon, and band-structure calculations were performed using both the PBE and the LDA exchange–correlation functionals for comparison and a plane-wave cutoff energy of 740.15 eV. The phonon calculations were performed using the method of finite displacements in supercells [130] with atomic displacements of about 10^{-3} to 10^{-2} Å from the equilibrium position. The vibrationally renormalised highest occupied molecular orbital (HOMO)-lowest unoccupied molecular orbital (LUMO) band gaps were found to be independent of the size of the atomic displacement in the phonon calculation.

For bulk silicon and carbon diamond, we used the DFT-LDA lattice parameters $a = 3.529$ and 5.394 Å, respectively, taken from Ref. [100]. The phonon and band-structure calculations were performed using LDA exchange–correlation functionals for consistency with Ref. [100]. The phonon calculations were performed using the method of finite displacements in supercells [130] with atomic displacements of amplitude 0.005 Åand plane-wave cutoff energies of 305.77 and 566 eV, respectively. The calculations used a $16 \times 16 \times 16$ Monkhorst–Pack **k**-point grid centred at Γ for 2-atom primitive cell and a set of phonon **q**-point grids commensurate with the supercell size $2\times2\times2$, $3\times3\times3$ and $4\times4\times4$ for C-diamond and $3\times3\times3$ and $4\times4\times4$ for Si-diamond. The Si calculation with a **q**-point grid of size $2 \times 2 \times 2$ was found to be insufficient to capture all the relevant phonons in the supercell, resulting in negative frequencies. The DFT-LDA band-structure calculations were implemented at different system sizes (containing $2N_\mathrm{p}$ atoms, where N_p is the number of primitive cells), using norm-conserving pseudopotentials (again, for consistency with Ref. [100]) and plane-wave cutoff energies of 348.31 and 1001.4 eV, respectively.

In the case of monolayer hBN, all of our DFT calculations were performed using norm-conserving pseudopotentials. We used the DFT-PBE lattice parameter $a = 2.512$ Å reported in Ref. [107]. The phonon calculations were implemented using density–functional perturbation theory [131] with phonon wave vectors commensurate with supercell size, a 32×32 Monkhorst–Pack **k**-point grid centred at Γ, a plane-wave cutoff energy of 700 eV, and an artificial periodicity of 26.46 Å. Our DFT-PBE electronic-band-structure calculations were performed for different

system sizes (containing $2N_\mathrm{p}$ atoms) using a plane-wave cutoff of 680 eV and an artificial periodicity of 21.17 Å in the out-of-plane direction. For bulk hBN, we used Tkatchenko–Scheffler dispersion-corrected [23] to include the van der Waals interlayer interaction. DFT-PBE phonon calculations with the DFT-PBE in-plane lattice parameter $a = 2.512$ Å [107] and the experimental out-of-plane lattice parameter $c = 6.6612$ Å [132] were performed. The calculations were performed for supercells containing $N_P = 9$ and 18 primitive cells.

3.1.1.2 DFT orbital generation for QMC trial wave function

The DFT calculations were used to generate orbitals for our QMC trial wave functions using Trail–Needs Dirac–Fock pseudopotentials with s chosen as the local channel to ensure the elimination of ghost states [60]. These orbitals were re-represented by 3D B-splines (blips) on a grid. For benzene, the DFT orbitals were obtained using both PBE and LDA functionals and a plane-wave cutoff energy of 2176.9 eV. For silicon and carbon diamond, the DFT-LDA orbitals were generated using different supercell sizes, a single $\mathbf{k}$-point at Γ, and plane-wave cutoff energies of 1088.456 and 1632.6840 eV, respectively. For hBN, we used the same lattice parameters as in our pure DFT calculations (see Sec. 3.1.1.1), with a plane-wave cutoff energy of 2721 eV.

3.1.1.3 The vibrational renormalisation of degenerate band edges

The vibrational renormalisation of the band gap due to electron-phonon coupling can be defined in three different ways, as shown in Table 3.5: (i) Δ_vib denotes the quantum average band gap between the valence band and conduction band with maximum overlap between the g_n-fold static-nucleus and offset geometry band structures; (ii) Δ_rand indicates the quantum average of the band gap that results from the random selection method presented in Sec. 2.4.3; and (iii) $\bar{\Delta}$ is the quantum average of the band gap calculated as the mean value of all direct transitions between the g_n^VB highest eigenvalues associated with the valence band maxima (VBM) and the g_n^CB lowest eigenvalues associated with the conduction band minima (CBM). In the case of a molecule system, Δ_vib is the quantum average HOMO-LUMO band gap.

3.1.2 QMC calculations

3.1.2.1 DMC calculations

Our QMC calculations were carried out using CASINO [25], in which we employed trial wave functions of the Slater–Jastrow (SJ) type with a single Slater determinant containing Kohn–Sham orbitals obtained from the DFT calculations; (see Sec. 3.1.1.2). We used a flexible Jastrow factor consisting of isotropic electron–electron, electron–nucleus, and electron–electron–nucleus polynomial terms and, for periodic systems, plane-wave electron–electron terms [37]. The wave function free parameters were optimised via minimisation of the variance of the energy [47, 48] followed by minimisation of the VMC energy [52]. For benzene, we also performed calculations using Slater–Jastrow–backflow (SJB) trial wave functions [46]. Where backflow was used, the Jastrow factor and backflow function were optimised together via VMC energy minimisation. We used Trail–Needs Dirac–Fock pseudopotentials, selecting the highest available angular momentum channel d as the local potential. Although the use of pseudopotentials introduces a bias into DMC calculations, the T-moves method ensures that this bias is positive [60, 133], resulting in some cancellation of errors in band-gap calculations.

The fixed-node DMC calculations were performed to compute the ground- and excited-state energies. The DMC energy is exact if the nodal surface of the trial wave function is exact; otherwise it is an upper bound on the exact ground-state energy. For each excited state, an appropriate wave function can be constructed by choosing the occupancies of the single-particle orbitals in the Slater determinants of QMC wave functions.

3.1.2.2 Optical band gap

The optical gap can be calculated as the difference between the total energies acquired by promoting an electron to an excited state and the total energy of the ground state. Therefore, the excited state can be selected by occupying single-particle orbitals in the Slater determinant in the trial wave function. The optical gap, then, is given by

$$\Delta_{\mathrm{Ex}}(\mathbf{k}_{\mathrm{v}}, \mathbf{k}_{\mathrm{c}}) = E'_N(\mathbf{k}_{\mathrm{v}}, \mathbf{k}_{\mathrm{c}}) - E_N, \tag{3.1}$$

where E_N is the ground-state energy and E'_N is the excited-state total energy of a system in which an electron has been promoted from an occupied state at wave vector $\mathbf{k}_\mathrm{v}$ to an unoccupied state at wave vector $\mathbf{k}_\mathrm{c}$. This promotion may be accompanied by a spin flip for triplet excitations. In the present study, we consider only the singlet excitations that correspond to the optical absorption gap. Our calculations also utilised the multideterminant trial wave functions to be examined in the calculations of the benzene molecules. In the QMC calculations of optical gaps, both E_N and E'_N must be assessed between pairs of $\mathbf{k}$-points that are simultaneously represented in the grid of the crystal momentum $\mathbf{k}$ that is commensurate with the supercell.

3.1.2.3 Random errors in the vibrationally renormalised gap

The standard error in the vibrational average of the excitation energy falls off as one over the square root of the number of atomic configurations sampled. Averaging over QMC calculations simultaneously reduces error bars due to the QMC sampling of electronic configurations and the sampling of atomic configurations; hence, the total cost of vibrationally renormalised QMC calculations may be sublinear in the number of atomic configurations. Indeed, if the computer time for a QMC gap calculation is dominated by DMC statistics accumulation, vibrational averaging is almost "for free." Furthermore, averaging over atomic configurations introduces trivial parallelism. Nevertheless, QMC gap calculations are much more expensive than their DFT counterparts, and it is thus possible to obtain significantly smaller error bars on vibrationally renormalised DFT energy gaps. We therefore used the DFT gaps as a control variate to reduce the statistical error bar of QMC gaps by fitting

$$\Delta_\mathrm{DMC}(\mathbf{R}) = \langle \Delta_\mathrm{DMC} \rangle + c\,[\Delta_\mathrm{DFT}(\mathbf{R}) - \langle \Delta_\mathrm{DFT} \rangle] \tag{3.2}$$

to the DMC energy gaps at different atomic configurations; $\Delta_\mathrm{DMC}(\mathbf{R})$ and the $\Delta_\mathrm{DFT}(\mathbf{R})$ are the DMC and DFT gaps at atomic configuration $\mathbf{R}$, c and the renormalised DMC gap $\langle E_\mathrm{DMC} \rangle$ are fitting parameters, and $\langle E_\mathrm{DFT} \rangle$ is the DFT renormalised gap with a fine sampling of atomic configurations.

3.1.2.4 Finite-size errors

To simulate an extended system, QMC simulations were performed using finite simulation cells subject to periodic boundary conditions. The simulation cell's size was constrained by both practical and computational considerations. These constraints resulted in finite-size (FS) errors that can be significant and represent one of the main barriers to the application of accurate QMC methods to solids [134]. Achieving high accuracy in QMC simulations of extended systems relies heavily on quantifying and correcting these errors.

We reduced FS effects by obtaining vibrationally renormalised gaps in different supercell sizes and extrapolating the results to infinite system size. Extrapolation to infinite system size uses scaling laws obtained by considering the screened electrostatic interactions between periodic images of excited quasiparticles or excitonic complexes [75, 135]. Such extrapolation not only removes much of the systematic error in the gap, but also helps to average out some of the quasirandom FS errors in energy gaps.

In a finite simulation cell, only a discrete set of vibrational wave vectors is commensurate with the periodic boundary conditions, leading to quasirandom FS effects in vibrational properties. For this reason, when evaluating the QMC vibrational renormalisation of the hBN gap, we evaluated a correction to the DFT vibrational renormalisation in a finite cell, which is then applied to the DFT vibrational renormalisation reported in Ref. [107]. This approach allowed us to focus on the difference between DFT and QMC vibrational renormalisations. The DFT renormalisation reported in Ref. [107] was itself determined via MC sampling of normal coordinates in finite cells to evaluate a correction to the DFT renormalised gap obtained by assuming a quadratic dependence of the gap on the normal coordinates; the latter approach enables the use of much larger system sizes [136].

3.1.2.5 Backflow

To address the effect of fixed-node errors in our calculations of excitonic gaps, we carried out some DMC gap calculations using backflow transformations with polynomial electron-electron and electron-nucleus terms. The inclusion of backflow

reduces the static-nucleus DMC optical gap of benzene by 0.07(2) eV. The energy difference is less than the effect of different geometry structures from LDA and PBE. In monolayer hBN, we find that backflow lowers the static-nucleus DMC direct gap by 0.02(2) eV and the indirect gap by 0.01(2), which are not statistically significant. In contrast, backflow lowers the static-nucleus DMC optical gap of Si 3×3×3 bulk and C diamond $2 \times 2 \times 2$ bulk by 0.22(7) and 0.091(22) eV, respectively, as shown in Table 3.1. These effects are expected to influence the vibrationally renormalised gap results to a comparable extent. However, the use of backflow correlation significantly increases the computational cost of QMC calculations, which can be highly demanding in vibrational-renormalisation calculations.

Table 3.1: Static-nucleus direct gaps in eV with and without backflow.

System	SJ-DMC	SJB-DMC
Benzene	5.679(18)	5.610(7)
Si $(3 \times 3 \times 3)$	3.83(5)	3.61(5)
C $(2 \times 2 \times 2)$	7.11(2)	7.02(1)
hBN^{dir} $(3 \times 3 \times 1)$	6.214(19)	6.20(2)
$\text{hBN}^{\text{indir}}$ $(3 \times 3 \times 1)$	5.953(19)	5.94(2)

3.2 Results and discussion

3.2.1 Molecular system: Benzene

Benzene is a planar nonlinear molecule with D_{6h} symmetry and a large energy gap, found to be about 4.9 eV [137] experimentally in gas-phase measurements. Recent DFT-PBE calculations revealed that vibrational effects reduce the static-nucleus gap by 0.5 eV [98]. Table 3.3 shows the energy gaps of benzene obtained via DFT with two choices of functional (LDA and PBE) and different wave functions with which to assess the accuracy of the DMC gaps. All the calculations were performed using a large simulation cell of volume 3507.4 Å^3 to ensure the elimination of the contribution of periodic images. Figure 3.1 illustrates the temperature dependence of benzene's optical gap over a wide temperature range (from 0 to 1800 K) based

on two different density functionals.

At 0 K, the atoms vibrate around their equilibrium positions as a result of quantum effects only, leading to zero-point renormalisation of band gaps. The DFT-PBE and DFT-LDA zero-point corrections to the band gap are −0.429(7) eV and −0.418(9), respectively. The renormalised band-gap curves showed a monotonic decrease with temperature, as illustrated in Fig. 3.1. At low temperature, renormalised band-gap curves are quadratic and governed by both the quantum and classical effects of lattice vibrations. However, at very high temperature, the renormalised band gaps shows a linear asymptote of temperature dependency that is dominated by classical effects. This relation can be well described by fitting to the Bose-Einstein law [1, 5]:

$$\Delta(T) = \Delta_0 - a\left[1 + 2\left(e^{\Theta/T} - 1\right)^{-1}\right], \tag{3.3}$$

where a and Θ are the fitting parameters given in Table 3.7. In general, both the DFT-LDA and DFT-PBE results exhibit a significant underestimation of the band gap due to the derivative discontinuity in the XC potential for the excited state [138].

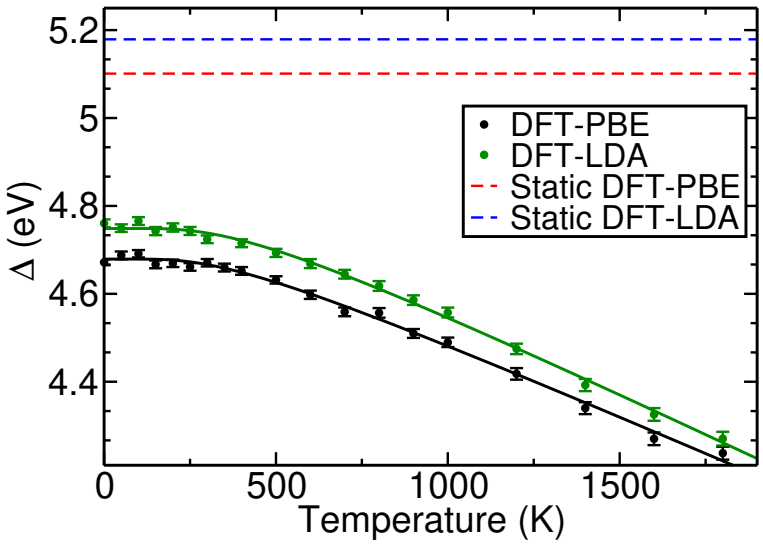

Figure 3.1: Temperature dependence of the vibrationally renormalised optical gap of benzene. The solid lines are the fit with the Bose–Einstein statistical factor, where fitting parameters are reported in Table 3.7.

In benzene the HOMO and LUMO are two-fold degenerate, so that we have to consider the different ways in which the orbitals at each randomly sampled atomic

configuration can be identified as corresponding to the static-nucleus HOMO and LUMO. The vibrational renormalisation of the band gap due to electron-phonon coupling can be defined in three different ways (see Sec. 3.1.1.3), as shown in Table 3.2. As a result of the local deformation of interatomic bonds caused by the presence of lattice vibrations (electron-phonon coupling), the bands are shifted to their vibrational renormalised values. Therefore, the PBE-DFT Δ_{vib}, Δ_{rand} and $\bar{\Delta}$ gaps showed that there are significant vibrational renormalisations of about $-0.428(7)$, $-0.121(1)$ and $-0.11(2)$ eV, respectively.

In Fig. 3.2, we report the vibrational renormalised (blue curve) eDOS average of benzene at room temperature. The static-nucleus band gap can be easily calculated between the 2-fold degenerate HOMO and LUMO bands, which were represented by two vertical black lines. The inclusion of the harmonic vibrational effects led to increase in the valence eigenvalue by around 0.14 eV, but significantly reduced the conduction eigenvalue by 0.28 eV as a result of the strong electron-phonon coupling. We found that these strong effects substantially removed the band edges degeneracy, as shown in Fig. 3.2 by the orange and red vertical lines. The renormalised HOMO-LUMO gap can be effectively inferred using the renormalised eigenvalues to be the highest occupied band energy and the lowest unoccupied band energy, respectively. Consequently, the minimum Δ_{vib} gap edge accurately represents the renormalised optical gap of benzene.

Table 3.2: The vibrationally renormalised optical gaps in eV for benzene at room temperature for different choices of the renormalised band gap.

Method	Δ_{vib}	Δ_{rand}	$\bar{\Delta}$
DFT-PBE	4.672(7)	4.98(1)	4.99(2)
SJB-DMC SD (PBE)	5.184(3)	-	-

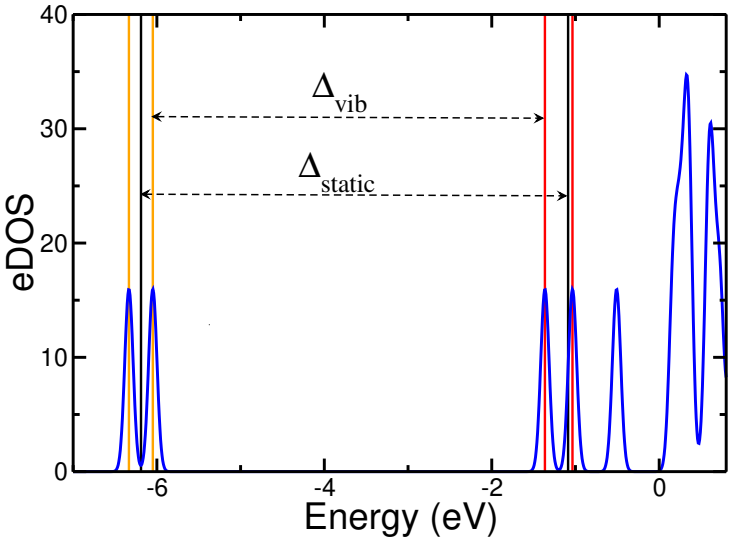

Figure 3.2: The vibrational renormalisation average of electronic density of states (eDOS) of benzene at room temperature (blue curve). The black vertical lines are the 2-fold degenerate static-nucleus HOMO and LUMO bands. The orange and red vertical lines are the two highest renormalised valence eigenvalues and two lowest renormalised conduction eigenvalues, respectively.

For vibrationally renormalised QMC gap calculations, we performed the calculation for 24 random distribution of nuclear coordinates. The VMC and DMC results obtained using the trial wave function with different level of accuracy are reported in Table 3.3. All the VMC gap results are upper bounds on the DMC gap energies, as shown in Fig. 3.4. All the DMC calculations were performed using time steps $\tau = 0.01$, 0.04, and 0.16 a.u. with the corresponding target walker populations being varied in inverse proportion to the time step. The total energies of both ground and excited states were extrapolated linearly to zero time step, as shown in see Fig. 3.3. To improve the nodal surfaces of our wave functions, we also carried out calculations using SJB wave functions. As shown in Table 3.3, the inclusion of backflow reduces the static-nucleus SJ-DMC band gap by 0.07(2) eV.

Multideterminant trial wave functions with a few determinants of 2-fold degenerate ground- and excited-states at the single-particle level were also used in our calculations. The use of multideterminant expansions to characterise electron promotion between degenerate states was statistically insignificant, resulting in a 0.01(1) eV reduction in the static-nucleus SJB-DMC band gap. We also performed SJB-DMC calculations using the DFT-LDA geometry, which showed a larger gap

than SJB-DMC using the DFT-PBE geometry by 0.14(2) eV. We found that the SJB-DMC ground-state energy obtained using PBE-DFT geometry and orbitals is lower than that calculated with LDA geometry and orbitals by 0.01(1) eV, which is statistically insignificant. The energy difference, however, is less than the vibrational-renormalisation correction to the band gap.

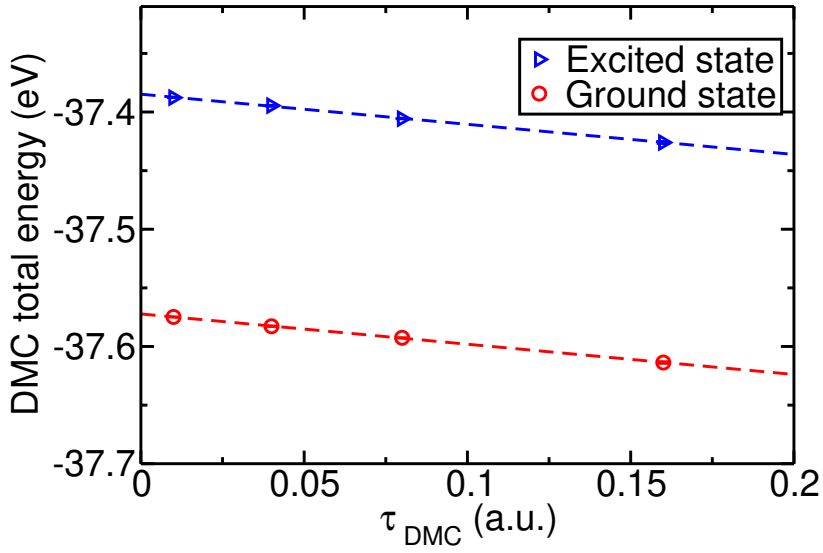

Figure 3.3: DMC total energies of benzene against DMC time step τ at the static-nucleus structure. The dashed lines show linear fits to the energy as a function of time step.

For vibrationally renormalised DMC gap calculations at zero temperature, the inclusion of a multideterminant expansion to describe the electron promotions from HOMO to the LUMO degenerate or nearly degenerate states introduced additional improvement into the trial wave function and reduced the excited-state energies, leading to a lowering of the renormalised SJB-DMC energy gap from 5.183(3) eV to 5.146(3) eV. At a randomly sampled atomic configuration, the degeneracy of the HOMO and LUMO states is lifted. The excited states can thus be correctly determined by promoting an electron from the HOMO to the LUMO using a single-determinant (SD) wave function in QMC calculations, leading to a zero-point renormalisation of $-0.427(8)$ eV. We found that employing a few-determinant expansion in the excited-state calculations lowered the vibrationally renormalised band gap by 0.037(5) eV with respect to the SD wave function, which is negligible compared to the attributable vibrational corrections.

Our results demonstrate a strong correlation (correlation coefficient $\rho = 0.98$) between SJB-DMC (SJB-VMC) and DFT-PBE gaps at randomly sampled atomic configurations, as shown in Fig. 3.4, justifying our use of DFT gaps as a control variate to reduce the statistical error bar of QMC gaps [Eq. (3.2)]. For the purpose of comparison, we performed SJB-DMC calculations of vibrational renormalisation based on the DFT-LDA structure. The SJB-DMC zero-point correction was found to be $-0.443(17)$ eV. Ideally, the two zero-point SJB-DMC corrections based on PBE- and DFT-LDA geometries should be identical; therefore, the discrepancies that arose were due to the DFT functional approximations and the errors inherent in the DFT evaluation of the harmonic vibrational frequencies of benzene [139]. This issue introduced a further source of error in our calculations, that is, the DFT evaluation of the harmonic normal mode frequencies of benzene. The vibrational renormalisation of the SD SJB-DMC optical gap at room temperature did not differ significantly from the zero-point vibrational renormalisation. However, it was found that the use of multideterminant wave functions was necessary to preserve the symmetry of the wave functions and retrieve the vibrational renormalisation of the band gap at room temperature. Our calculations using multideterminant wave functions significantly reduced the vibrational renormalisation of SJB-DMC optical gap to 5.087(3) eV, which was in good agreement with experimental results [137]. Additional sources of error in the VMC and DMC gaps included the neglect of anharmonicity effects and the use of pseudopotentials.

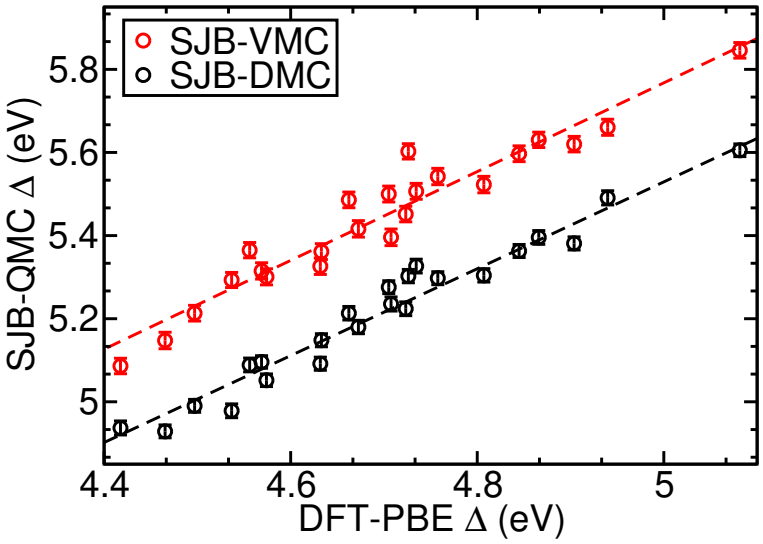

Figure 3.4: Benzene vibrationally renormalised gaps using SJB-VMC (red circles) and SJB-DMC (black circles) against DFT-PBE gaps, for different atomic configurations.

Table 3.3: Static-nucleus and vibrationally renormalised excitonic gaps in eV for benzene at 0 K. An asterisk (*) denotes the vibrationally renormalised gaps at room temperature.

Method	Δ_{static}	Δ_{vib}
DFT-PBE	5.101	4.672(7) 4.673(7)*
DFT-PBE [98]	5.106	4.653
DFT-LDA	5.179	4.761(9) 4.724(9)*
SJ-VMC SD (PBE)	5.93(1)	
SJB-VMC SD (PBE)	5.89(1)	5.415(4)
SJB-VMC MD (PBE)	5.76(1)	
SJ-DMC SD (PBE)	5.68(2)	
SJ-DMC SD (PBE) [98]	5.63(4)	
SJB-DMC SD (PBE)	5.610(7)	5.1827(34) 5.184(3)*
SJB-DMC SD (LDA)	5.75(2)	5.302(3)
SJB-DMC MD (PBE)	5.600(7)	5.1460(34) 5.087(3)*
Exp. ($T = 300$ K)		4.9 [137]

3.2.2 2D crystalline system: monolayer hexagonal boron nitride

Of the materials in the family of 2D atomic crystals, hexagonal boron nitride (hBN) was one of the first to be mechanically exfoliated from bulk phases [140]. It is a dielectric, insulating material possessing D_{6h} space group symmetry with a honeycomb lattice structure based on sp_2 covalent bonds that complements graphene and the transition metal dichalcogenides in electronic and optical properties [141]. In contrast to graphene, which has no band gap, hBN exhibits a wide band gap in the π bands because the inversion symmetry is broken by the mismatch between the boron and nitrogen sublattices [142]. Recent advances in experimental approaches for merging graphene and other 2D materials to form van der Waals heterostructures have garnered significant interest owing to their remarkable properties. Because hBN is atomically flat and electrically inert, it has been found to be an exceptional substrate for graphene when the lattice misalignment angle is large [141, 143]. At small misalignment angles, the moiré superlattice potential can radically change the low-energy electronic properties of graphene. Examples include the appearance of second-generation Dirac points and the formation of Hofstadter's butterfly states in the presence of an applied magnetic field [144, 145].

Recently, many theoretical and experimental studies have investigated the atomically thin hBN sheets consisting of a single to a few monolayers due to the unique properties associated with their 2D structure and high crystal quality [107, 146–153]. For 2D monolayer materials, in-plane screening modifies the form of the Coulomb interaction between charges, resulting in strong long-range Coulomb interactions that heavily influence the band gap in these materials. The main feature of interest here is the enhancement of the electron–phonon interactions in these 2D systems [154] and its effect on the band gaps. As a consequence of the strength of electron–phonon coupling in 2D materials, studies have identified considerable vibrational renormalisation of band gaps for both monolayer and bulk hBN [107, 155]. Despite this increasing interest in hBN and the vast number of studies dedicated to this material, the fundamental issues of the nature of its band gap and the effect of including electron–phonon interactions remain controversial.

Utilising our newly developed random sampling technique along with the DFT and QMC calculations, we investigated the vibrational renormalisation of optical band gaps in both monolayer and bulk hBN.

The phonon dispersion in hBN obtained from DFT-PBE calculations along the high–symmetry directions $\Gamma \rightarrow \mathrm{K} \rightarrow \mathrm{M} \rightarrow \Gamma$ is illustrated in Fig. 3.5(a). The calculations showed that artificial imaginary frequencies were introduced into the flexural acoustic phonon modes around the Γ point, a phenomenon frequently observed in first-principles lattice dynamics calculations for 2D materials [107, 156]. This was not an issue for wave vectors commensurate with the supercells that we used to sample normal mode coordinates. Our results were consistent with the phonon dispersion curves reported in Ref. [107].

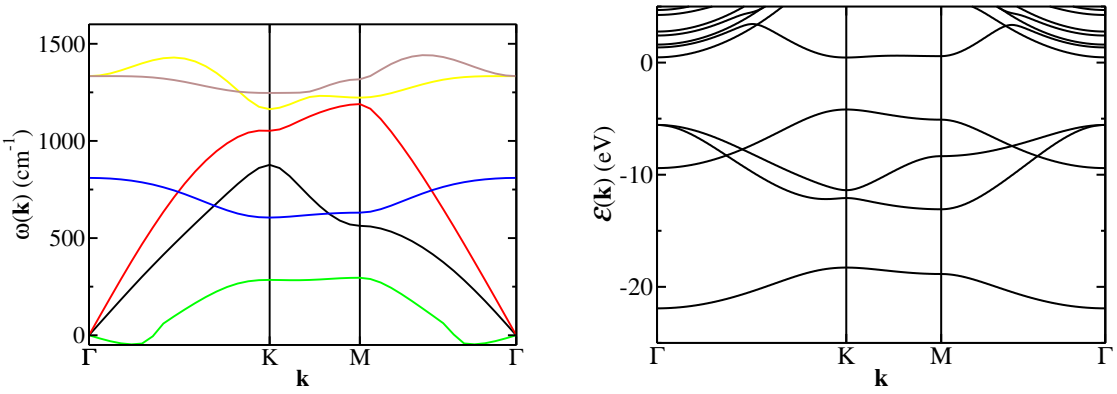

(a) (b)

Figure 3.5: (a) DFT-PBE phonon dispersion curves for monolayer hBN and (b) DFT-PBE electronic band structure for monolayer hBN.

Table 3.4 summarises our final DFT-PBE and SJ-DMC static-nucleus and vibrationally renormalised optical band gaps at 0 K. We calculated the promotion of electrons from $K_\mathrm{v} \rightarrow K_\mathrm{c}$ and $K_\mathrm{v} \rightarrow \Gamma_\mathrm{c}$ at different system sizes. The direct and indirect optical gap calculations were performed in supercells of size $3m \times 3n$ centered on the Γ point, where m and n are integers. In a 4×4 supercell of hBN, only the $K_\mathrm{v} \rightarrow K_\mathrm{c}$ excitonic gap was calculated by shifting the supercell Bloch vector $\mathbf{k}_\mathrm{s}$ point to the K point of the primitive-cell BZ. Both the valence and conduction bands of supercells were identified using the band-unfolding procedure described in Sec. 2.4.2. Averaging over harmonic nuclear vibrational motion reduced the static-lattice band gaps. Our DFT-PBE band-structure calculations predict a direct band

gap ($K_v \rightarrow K_c$), as shown in Fig. 3.5(b). The DFT-PBE $K_v \rightarrow K_c$ and $K_v \rightarrow \Gamma_c$ energy gaps with a fine **k**-point mesh are 4.636 eV and 4.654 eV, respectively. For the larger system size $6 \times 6 \times 1$ (72 atoms), harmonic vibrational effects increase the valence band eigenvalue at K_v by around 0.034(2) eV and reduced that of the conduction band by more than 0.089(1) eV at K_c and by 0.069(4) eV at Γ_c. This indicates that electron-phonon coupling is stronger than hole-phonon coupling. Our DFT zero-point correction for the minimum gap $K_v \rightarrow K_c$ was $-0.125(3)$ eV and for the $K_v \rightarrow \Gamma_c$ gap was $-0.103(4)$ eV. However, the DFT calculations significantly underestimate the band-gap results.

All the SJ-DMC calculations were performed using time steps $\tau = 0.04$ and 0.16 a.u. and target populations that were varied inversely with time step τ. To account for systematic FS errors, the energies of optical gaps were calculated at different supercell sizes. Using DFT-PBE calculations, the $O(N_p^{-1})$ FS error was dominant in the $K_v \rightarrow K_c$ and $K_v \rightarrow \Gamma_c$ excitonic gaps of the isolated hBN sheet, as shown in Fig. 3.6. We therefore extrapolated our SJ-DMC optical gaps to the thermodynamic limit using an order $O(N_p^{-1})$ scaling. Physically, this scaling is appropriate because the simulation cell size is comparable to the exciton Bohr radius [107]. In agreement with the observation in Ref. [107], our SJ-DMC calculations show that the isolated hBN sheet is an indirect semiconductor. For the static-nucleus direct optical gap, there is a statistically significant difference between our DMC result and earlier work [107] despite using a similar range of supercell sizes. This is probably due to the fact that our results were accurately converged to the limit of infinite system size with a lower estimated error bar. We found that the static-nucleus results of the direct and indirect optical gaps were 8.06(3) eV and 6.88(5) eV, respectively.

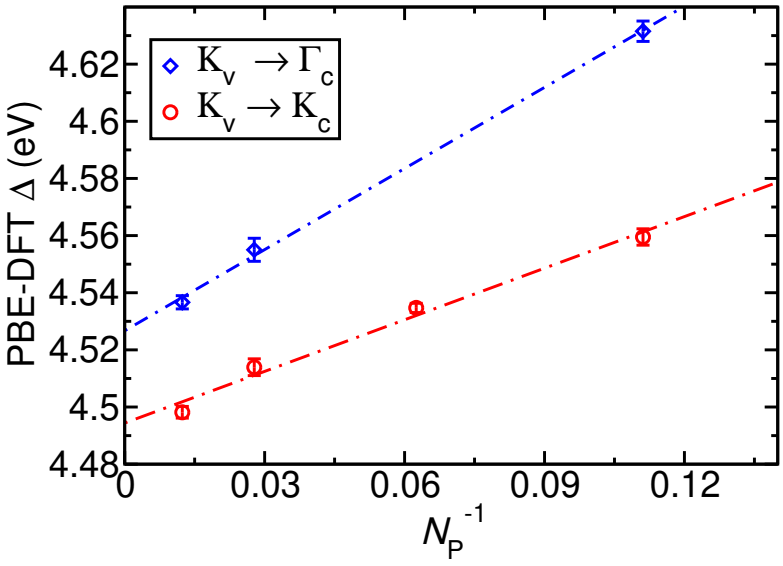

Figure 3.6: DFT-PBE renormalised excitonic gaps of monolayer hBN against N_{p}^{-1}, where N_{p} is the number of primitive cells in the supercell.

Figure 3.7 shows a plot of the SJ-DMC vibrational renormalised excitonic band gaps for both direct and indirect gaps against system size. The SJ-DMC vibrational-renormalisation results were obtained for 24 random atomic configurations. The energies were then extrapolated linearly to zero time step, and the results were then averaged over atomic configurations using Eq. (3.2). The DMC optical gaps of supercells of various system sizes were extrapolated to the thermodynamic limit of infinite system size using $O(N_{\mathrm{p}}^{-1})$ scaling. The zero-point renormalisation of the direct optical gap $K_{\mathrm{v}} \rightarrow K_{\mathrm{c}}$ was around $-0.61(4)$ eV slightly larger than the DFT result of the earlier work [107]. In contrast, the inclusion of zero-point motion effects induces a slight decrease in the indirect gaps by around $-0.08(5)$ eV in disagreement with [107]. Our results show that the inclusion of the vibrational effects improves the agreement with the experimental result.

Table 3.4: Static-nucleus and vibrationally renormalised optical gaps for monolayer hBN at 0 K.

Gap	Supercell	SJ-DMC (eV)		DFT-PBE (eV)		Exp.
		Δ_{static}	Δ_{vib}	Δ_{static}	Δ_{vib}	
$K_{\text{v}} \to K_{\text{c}}$	3×3	6.214(19)	5.924(13)	4.591	4.560(2)	
	4×4	6.802(29)	6.594(14)	4.6305	4.5347(16)	
	6×6	7.61(3)	7.074(12)	4.639	4.514(3)	
	9×9	8.43(8)	-			
		8.6(2) [107], 8.06(3)	7.46(2)			
$K_{\text{v}} \to \Gamma_{\text{c}}$	3×3	5.953(19)	5.710(13)	4.606	4.632(3)	
	6×6	6.49(4)	6.524(12)	4.658	4.555(4)	
	9×9	7.19(8)	-			
		6.9(3) [107], 6.88(5)	6.80(2)			
VBM→CBM						6.1(3) [157]

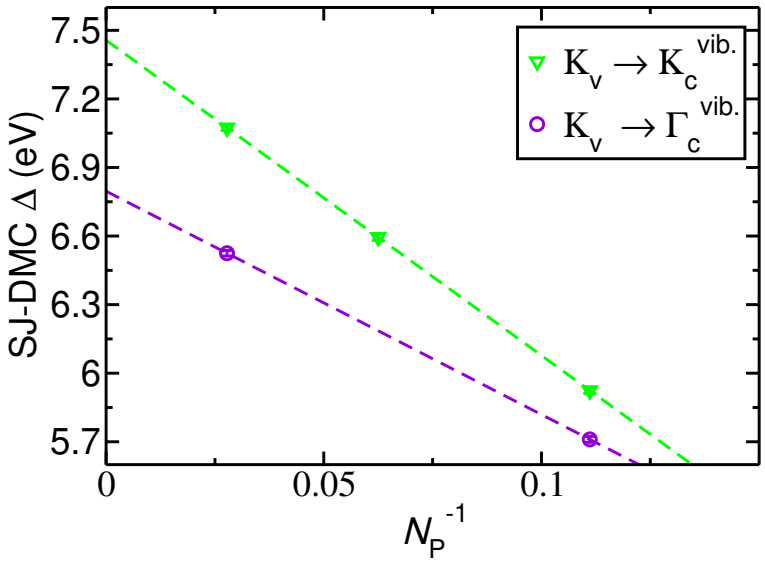

Figure 3.7: SJ-DMC vibrationally renormalised excitonic gaps of monolayer hBN against N_{p}^{-1}, where N_{p} is the number of primitive cells in the supercell.

3.2.3 3D crystalline systems

3.2.3.1 Si and C diamond

Si and C in the diamond structure are semiconductors with indirect band gaps and a face centered cubic lattice with a basis of two atoms. The valence-band maximum is at the Γ point, and the conduction-band minimum is on the line connecting the Γ and X points of the BZ. The effects of electron-phonon interactions on the electronic band structure represent one of the fundamental properties of the semiconductors that have been extensively investigated experimentally and theoretically over the last few decades [1, 75, 79, 81, 86, 102, 158–165]. Understanding electron-phonon coupling in these materials continues to be very important for more recent technological applications [166, 167]. Si and C diamond, therefore, offer an ideal foundation for benchmarking the vibrational renormalisation of QMC band-gap results. Using our approach, we investigated the zero-point harmonic renormalisation and temperature dependence of the direct $\Gamma_v \rightarrow \Gamma_c$ excitonic gap in both materials.

Table 3.5 shows the DFT-LDA vibration renormalisation of the direct band gap using three different methods. Our C diamond $2 \times 2 \times 2$, $3 \times 3 \times 3$ and $4 \times 4 \times 4$ supercell Δ_{vib} results show that there is a substantial difference of around $-0.05(2)$ eV, $-0.29(1)$ eV and $-0.286(9)$ eV, respectively, from the static-nucleus band gap. These vibrational renormalisation corrections are a clear indication of the strength of the electron-phonon coupling effects. In contrast, the Si bulk results demonstrated a marginal difference between the gaps, implying weak electron-phonon coupling. In both systems, the direct optical band gaps of Si and C diamond correspond to the minimum Δ_{vib} gaps.

Figure 3.8 shows the calculated zero-point normalization and T-dependence of the DFT-LDA direct band gap of Si and C diamond with the static band gap as a reference. The calculations were carried out using large simulation cells containing 128 atoms. The ground and excited states were determined by finding the orbitals that have the maximum overlap with the "target" static lattice orbitals (see Sec. 2.4.2). The Si and C diamond DFT-LDA static-nucleus direct band gaps with fine $\mathbf{k}$-point sampling are 2.545 eV and 5.556 eV, respectively. Electron-

Table 3.5: Zero-point vibrational renormalisation of direct band gaps of Si and C diamond at 0 K for different choices of the renormalised band gap.

Supercell	C diamond (eV)			Si diamond (eV)		
	Δ_{vib}	Δ_{rand}	$\bar{\Delta}$	Δ_{vib}	Δ_{rand}	$\bar{\Delta}$
$2 \times 2 \times 2$	5.40(2)	5.41(2)	5.41(2)	-	-	-
$3 \times 3 \times 3$	5.24(1)	5.316(9)	5.30(1)	2.487(3)	2.480(3)	2.480(2)
$4 \times 4 \times 4$	5.261(9)	5.35(2)	5.36(5)	2.506(2)	2.504(2)	2.502(2)

phonon interactions introduce temperature-dependence into the electronic band structure. In particular the band gaps of many semiconductors exhibit the well-known monotonic decrease with temperature [168]. This relation can be well described using the phenomenological expression of the Bose-Einstein law [1, 5], where the fitting parameters are given in Table 3.7. As Fig. 3.8 shows, the T-dependence of the direct band gap in bulk Si is relatively small compared to that in C diamond. The zero-point renormalisation corrections for the larger supercell size ($4\times4\times4$) are $-0.03(2)$ eV for Si and $-0.286(9)$ eV for C diamond in agreement with DFT-LDA vibrational corrections in Ref. [99]. The insets in Fig. 3.8 also illustrate a comparison with experimental results [1, 2]. All the DFT-LDA results substantially underestimate the direct band gap in both materials, and the use of a post-DFT method (DMC in this work) is critical to restoring the agreement with experiments.

Our final DFT and DMC energy gap results for Si and diamond are shown in Table 3.6. The fixed-node DMC results were obtained using real trial wave functions constructed at the Γ point of the simulation supercell. The SJ-DMC static-nucleus band gaps were 3.83(5) eV for Si and 8.653(11) eV for C diamond. DMC calculations were performed for 24 randomly sampled atomic configurations using time steps $\tau = 0.04$ and 0.16 a.u. and target populations that were varied inversely with time step τ. Figure 3.9 shows the linear correlation between the DFT and DMC zero-point motion renormalisation of optical gaps as a function of atomic configuration. DFT band gaps can therefore be used as a control variate when evaluating the DMC band-gap energy. To investigate the convergence of the results as a function of cell size and to account for FS errors, the calculations were performed using different sizes of fixed supercell shape. The results were then extrapolated to the thermodynamic

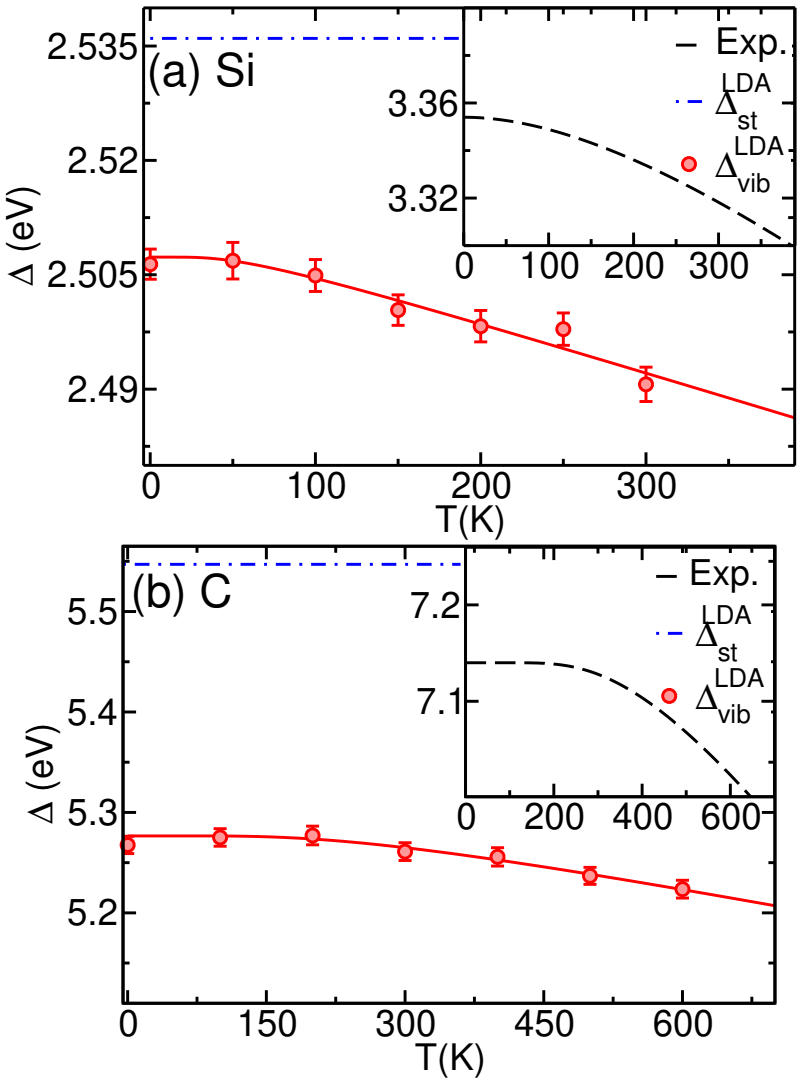

Figure 3.8: T-dependence of the direct energy gap of (a) Si ($4 \times 4 \times 4$ supercell) and (b) C diamond ($4 \times 4 \times 4$ supercell). The blue lines represent the DFT-LDA static-nucleus band gap with a set of **k**-points grid that commensurate with the supercell size. The red circles indicate DFT-LDA results, which have error bars of around 0.002 eV. The black dashed lines in the inset show curves fitted to the experimental results of Ref. [1] for Si and Ref. [2] for C diamond.

limit assuming the errors scale as $O(N_{\mathrm{p}}^{-1/3})$, because the supercells are much smaller than the exciton Bohr radius, implying that the electron-hole pair is unbound and hence that the systematic finite-size error is a screened simulation-cell Madelung constant [75].

The SJ-DMC vibrational-renormalisation calculations of C diamond show a significant reduction in the direct band gaps. The zero-point correction of the direct band gap Δ_{vib} is about $-1.0(1)$ eV, larger than previously reported GW corrections in Refs. [79] and [81]. In addition, the random selection direct optical gap Δ_{rand} was calculated in order to explore the harmonic vibrational effects on the band edge degeneracies. Our SJ-DMC Δ_{rand} results showed a insignificant difference of around 0.2(2) eV from the direct optical gap Δ_{vib}. The large vibrational renormalisation indicates strong electron-phonon coupling effects. The incorporation of harmonic vibration correction significantly improves the agreement with the experiment, and the remaining discrepancy can be attributed to the neglect of anharmonic effects and the use of pseudopotential. In contrast, the vibrational-renormalisation correction of the Si band gap was relatively small, in agreement with the DFT results in Table 3.5. We found that the SJ-DMC zero-point correction to the Si band gap is $-0.12(5)$ eV for a simulation cell containing 54 atoms. This indicates the weak effects of the electron-phonon coupling on the silicon direct band gap.

Comparing the vibrational renormalised SJ-DMC optical gaps with experimental results for silicon and diamond shows overestimate of around 0.31(2) eV and 0.39(7) eV, respectively. There are several sources of uncertainty in our calculations, including the use of pseudopotentials, the neglect of anharmonic effects, the unquantified fixed-node errors resulting from the use of a single determinant wave function, and the residual finite-size errors in diamond or the untreated finite-size effects in the case of silicon. In addition, the backflow results in Table 3.1 indicate that the fixed node errors significantly impact the static-nucleus DMC gaps. The neglect of the treatment of these effects in the vibrational renormalisation gap calculations introduces an additional source of errors in the results.

Table 3.6: Static-nucleus and vibrationally renormalised $\Gamma_v \to \Gamma_c$ excitonic gaps for Si and C diamond at 0 K in eV.

System	Supercell	SJ-DMC optical gap			DFT-LDA optical gap			Exp.
		Static	Δ_{vib}	Δ_{rand}	Static	Δ_{vib}	Δ_{rand}	
Si	$2 \times 2 \times 2$	3.57(4) [75]			2.401			3.354(2) [1], 3.40 [162]
	$3 \times 3 \times 3$	3.82(9)[75], 3.83(5)	3.713(21)		2.493	2.487(3)	2.480(3)	
	$4 \times 4 \times 4$	3.9(1) [75]			2.536	2.506(2)	2.504(2)	
Diamond	$2 \times 2 \times 2$	7.23(2) [169], 7.11(2)	6.59(1)	6.57(1)	5.446	5.40(2)	5.41(2)	7.3 [169], 7.153(9) [2]
	$3 \times 3 \times 3$	7.62(3)	6.98(2)	7.01(2)	5.526	5.24(1)	5.316(9)	
	$4 \times 4 \times 4$				5.547	5.261(9)	5.35(2)	
	∞	8.653(11)	7.69(7)	7.88(8)				

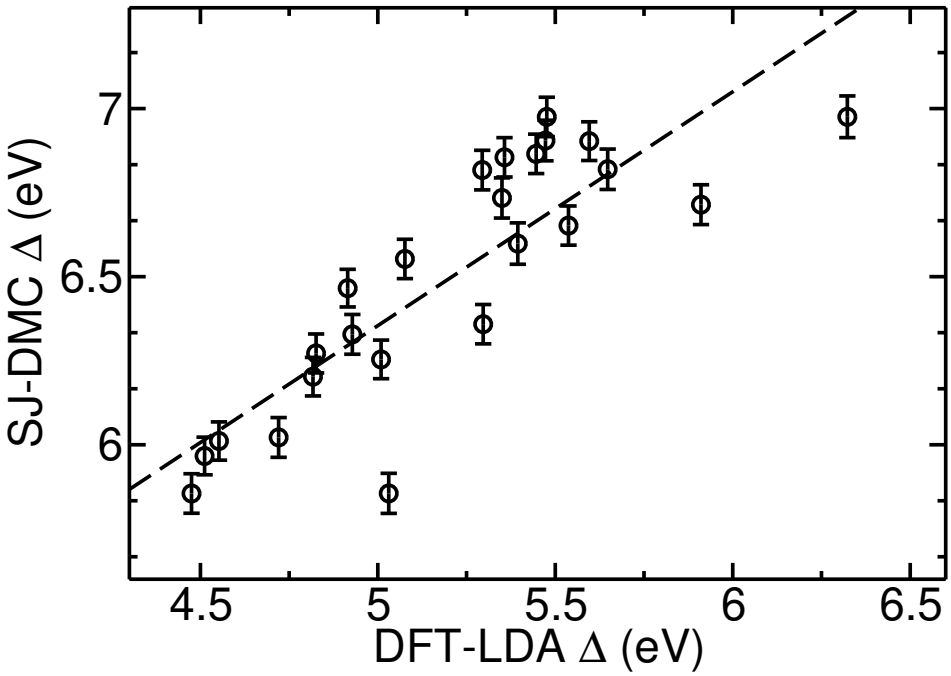

Figure 3.9: SJ-DMC vibrationally renormalised direct optical gap of C-diamond $2\times2\times2$ bulk against DFT-LDA gaps, for different atomic configurations. The error bar at each atomic configuration is around 0.06 eV.

Table 3.7: The values of resulting parameters from the fit of the T-dependence band-gap energies to the Bose–Einstein law [1, 5].

System	Δ_0 (eV)	a (meV)	Θ **K**
C_6H_6 (DFT-PBE)	4.851	171.98	1006.67
C_6H_6 (DFT-LDA)	4.96	210.73	1122.2
Si (DFT-LDA)	2.512	5.099	153.89
C (DFT-LDA)	5.35	68.73	763.77

3.2.3.2 Bulk hBN

Bulk hBN, also known as white graphite, is a wide-band-gap semiconductor with high chemical and thermal stability. Bulk hBN consists of monolayer hBN layers that are bonded by weak interplanar van der Waals force. This stacking is an AA' arrangement with experimental interatomic spacing of 6.6612 Å [132], in which the prime symbol indicates that the atoms in the same vertical sublattice sites of

the hexagonal lattice layers are of different species. The experimental estimate of the nature (direct–indirect crossover) and magnitude of the bulk hBN band gap has long been a point of contention, with findings varying across studies. Experimentally measured band gaps range from 4.3 to 7.1(1) eV [148, 150–153]. Recent experimental work by Watanabe *et al.* [153] has determined that bulk hBN is a direct semiconductor with an excitonic gap of 5.822 eV. Recent research conducted by Cassabois *et al.* [148] has revealed that bulk hBN is in fact an indirect semiconductor with an excitonic gap of 5.955 eV.

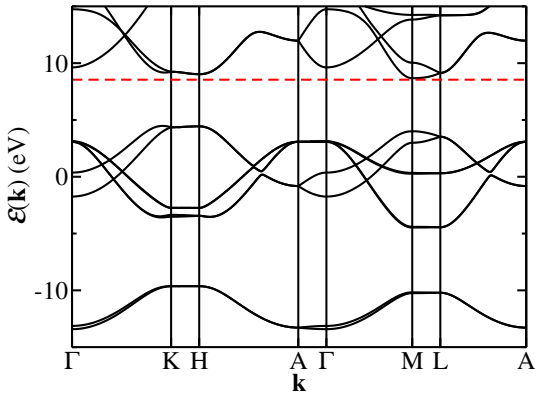

Figure 3.10: The DFT-PBE electronic band structure for bulk hBN.

In the Fig. 3.10, the PBE-DFT band structure for bulk hBN is plotted along high-symmetry directions of the BZ. The static-nucleus DFT-PBE energy gaps with a fine **k**-point sampling for $K_{\mathrm{v}} \to K_{\mathrm{c}}$ and $K_{\mathrm{v}} \to \Gamma_{\mathrm{c}}$ optical gaps were 4.890 eV and 5.278 eV, respectively. In Table 3.8, we report the PBE-DFT and SJ-DMC gap results for bulk hBN supercells. We observe that both the direct and indirect gaps of bulk hBN decreased with the increase of the number of layers. This trend of decreasing band gaps was attributed to the increased dispersion of electronic bands caused by interlayer interactions [170]. The DFT band-structure calculations were performed using supercells containing 36 and 72 atoms at the gamma point. Our results showed that the DFT calculations not only underestimated the band gaps but also yielded an incorrect conduction band minimum. In the DFT-PBE band-structure calculations, the bulk hBN had a direct optical gap ($K_{\mathrm{v}} \to K_{\mathrm{c}}$) with a zero-point correction of around $-0.066(2)$ eV. The vibrational renormalisation of the indirect gap ($K_{\mathrm{v}} \to \Gamma_{\mathrm{c}}$) was approximately $-0.046(3)$ eV.

Within the static-nucleus SJ-DMC gap calculations, we found that a supercell

of bulk hBN containing $N_p = 9$ primitive cells has an indirect optical gap, in agreement with the latest experimental observation [148] and QMC study by Hunt *et al.* [107]. Our results show that the static-nucleus SJ-DMC optical gap between the top of the valence band at K and the bottom of the conduction band at Γ is 6.90(2) eV. In contrast, the static-nucleus SJ-DMC direct ($K_v \to K_c$) gap is around 7.04(2) eV. The SJ-DMC vibrational renormalisation calculations were performed for 24 atomic configurations with time steps $\tau = 0.04$ and 0.16 a.u. and target populations that were varied inversely with time step. The band-unfolding procedure was performed to identify the valence and conduction bands and the final gap results were obtained by averaging over the atomic configuration using Eq. (3.2). The SJ-DMC zero-point vibrational corrections for the minimum band gap $K_v \to \Gamma_c$ was $-0.12(2)$ eV and for the $K_v \to K_c$ gap was $-0.28(2)$ eV. Our results show that the inclusion of the vibrational effects in SJ-DMC calculations alters gaps by significant fractions compared with the PBE-DFT vibrational corrections. These large SJ-DMC zero-point corrections indicate strong electron-phonon coupling effects and the inefficiency of DFT calculations in describing them. These effects are expected to substantially modify the optical gaps for larger supercell sizes and enhance the agreement with the experimental results.

Table 3.8: Static-nucleus and vibrationally renormalised optical gaps for bulk hBN at 0 K.

Gap	Supercell	SJ-DMC (eV)		DFT-PBE (eV)		Exp.
		Δ_{static}	Δ_{vib}	Δ_{static}	Δ_{vib}	
$K_v \to K_c$	$3 \times 3 \times 1$	7.04(2)	6.876(6)	4.863	4.826(3)	
	$3 \times 3 \times 2$			4.582	4.516(2)	
		8.3(1) [107]				
$K_v \to \Gamma_c$	$3 \times 3 \times 1$	6.90(2)	6.772(8)	5.239	5.219(4)	
	$3 \times 3 \times 2$			5.154	5.108(3)	
		8.2(5) [107]				
VBM→CBM						5.822 [153] 5.955 [148]

3.3 Conclusion

In summary, we performed DFT and QMC calculations to determine the static-nucleus and vibrationally renormalised band gaps for a range of materials. The zero-point renormalisation and the temperature dependence effects were included in the calculations using the proposed method. The vibrational renormalisation results of benzene band gap showed that the implementation of a superior wave function with a backflow function and multideterminant expansions substantially improves the agreement with the experimental results. The SJ-DMC renormalised direct gap calculations of C-diamond gave the largest vibrational correction in our presented calculations by around $-1.0(1)$ eV, whereas bulk Si showed small but non-trivial vibrational corrections. We have also investigated the vibrational corrections of the optical gaps of monolayer hBN at different system sizes. Our results showed that the inclusion of the zero-point motion effect significantly decreases the direct gap by around $-0.61(4)$ eV, but the indirect gap is only marginally reduced. The vibrational renormalisation of bulk hBN showed a seizable correction of band gaps and a larger range of supercell sizes are needed to improve the agreement with the experimental results.

Chapter 4

Quantum Monte Carlo study of trion formation in weakly doped monolayer $MoSe_2$ encapsulated by hBN

4.1 Introduction

In recent years, the rapid development in the fabrication and control of quasi-two-dimensional semiconductor heterostructures has led to the production of truly two-dimensional (2D), atomically thin semiconductors [140]. Extensive research has been dedicated to investigating the functional properties of these materials. At thermodynamic equilibrium, the intrinsic charge carriers of these systems encounter reduced out-of-plane electrostatic screening, resulting in the formation of electron-hole pairs (neutral exciton) via Coulomb attraction, generally with exciton binding energies ranging from tens to hundreds of meV [147, 171, 172]. Under finite doping, the weak out-of-plane electrostatic screening and the strong 2D geometrical confinement result in the emergence of new many-particle phenomena such as trions [173]. The rich physics resulting from the Coulomb interaction between electrons and holes in these materials offers a wide range of potential novel optoelectronic applications.

Monolayer transition metal dichalcogenides (TMDCs) are very promising nanos-

tructures of the 2D-periodic thin layer semiconductors that can be easily exfoliated. Their remarkable electronic and optical properties attract a lot of interest [174–177]. The pre-existing finite concentration of charge carrier for these materials led to the emergence of an abundance and variety of excitonic complexes that were observed as distinct lines in their photoluminescence (PL) spectra [175, 176, 178–180]. The unusual nature of excitonic complexes in 2D TMD materials shows strong binding energies that have been the subject of many theoretical studies [172, 181–186]. As a result of their nature of strong excitonic effects, as well as their promising optoelectronic application, TMDCs have become attractive materials for many studies. Recent experimental investigations have demonstrated that the lowest energy peak in the PL spectra of a doped TMDC monolayer is often induced by trions (negative and positive) [187–190]. Their distinct band structure of direct band gap at K and K' points of the hexagonal Brillouin zone associated with the spin and valley degrees of freedom, allowing for the investigation of various trion states (dark and bright) in 2D TMDC [185, 191, 192].

Recent experiments investigated high-quality van der Waals heterostructures based on TMDC monolayers encapsulated in hexagonal boron nitride (hBN) layers [193–195]. The results showed that the hBN encapsulation of TMDC materials isolated them from the effects of the substrate and sharply narrowed their photoluminescence linewidth, allowing access to their intrinsic optical properties. These homogeneous dielectric environments induced additional screening effects that influenced the exciton binding energy and renormalised the free-particle bandgap in TMDC materials [196, 197]. Moreover, both the polarisation effects of these thin layers and their weak dielectric screening mutually contribute to modifying the interaction form between charge carriers from the Coulomb interaction to the so-called Keldysh interaction [198–200]. The Keldysh interaction behaves logarithmically at a short distance and it reduces to the Coulomb form $(1/r)$ at long range. Over the past decade, many works have studied the binding energies of isolated excitonic complexes in 2D semiconductors using the Keldysh interaction [181, 183–185, 201], but the effect of the surrounding charge carriers on these species remains ambiguous. In this chapter, I will present the quantum Monte Carlo simulations of a single hole in ideal, dilute weakly doped 2D homogeneous

electron gas (HEG) modelling ($MoSe_2$). This allows for investigation of the effect of a finite concentration of charge carriers that interact via the Keldysh interaction on the binding energy of negative trions.

In the study of 2D HEG, it is more convenient to work in a scaled set of units that are physically appropriate for the system. In Hartree atomic units ($\hbar = |e| = m_e = 4\pi\epsilon_0 = 1$), lengths are in terms of the Bohr radius a_0, masses are in terms of the bare electron mass m_e, and energies are in terms of Hartree (Ha). In this chapter, effective Hartree atomic units are used unless otherwise stated. The lengths are given in unit of the exciton Bohr radius as $a_0^* = (\epsilon/\mu)\, a_0$, where ϵ is the static dielectric constant (relative permittivity) of the host material, $\mu = m_e^* m_h^*/(m_e^* + m_h^*)$ is the reduced mass of the electron–hole pair, and m_h^* and m_e^* are the hole and electron effective masses, respectively. The energy is given in terms of the exciton Hartree $\mathrm{Ha}^* = (\mu/\epsilon^2)\,\mathrm{Ha}$, where the exciton Rydberg (Ry^*) is $1R_y^* = \mathrm{Ha}^*/2$. There are three important length scales in our calculations including the Coulomb exciton Bohr radius a_0^*, the Keldysh interaction length scale r_0 and the density parameter r_s of the 2D HEG.

4.1.1 Keldysh interaction

It is important to consider the electrostatic screening effects in describing the interactions between charge carriers in 2D semiconductor materials. In the 2D TMDs thin sheets, the polarisation effects of a confined structure alter the Coulomb electrostatic interactions to Keldysh interaction form. Consider a 2D semiconductor sheet of zero thickness at $z = 0$ that contains a charge density

$$\rho(r) = \rho(x, y)\delta(z), \tag{4.1}$$

and embedded in an isotropic medium of permittivity ϵ. The electric displacement field $\mathbf{D}$ that results due to this charge is given by

$$\mathbf{D} \;=\; \epsilon\mathbf{E} + \mathbf{P} = -\epsilon\nabla\phi + \mathbf{P} \tag{4.2}$$

where $\mathbf{E}$ is the electric field, ϕ is the electrostatic potential, and $\mathbf{P} = \mathbf{P}_\perp(x, y)\delta(z)$ is the polarisation vector, where $\mathbf{P}_\perp(x, y)$ is the in-plane polarisation. The $\mathbf{P}_\perp$ can be written as

$$\mathbf{P}_\perp = -\kappa\nabla[\phi(x, y, 0)], \tag{4.3}$$

where $\mathbf{P}_\perp$ has no component in the z direction because the charge lies in-plane and κ is the in-plane susceptibility of the material.

Now, using Gauss's law, where $\nabla \cdot \mathbf{D} = \rho(x,y)\delta(z)$, gives

$$\epsilon\nabla^2\phi = -\rho\delta(z) - \kappa(\nabla^2[\phi(x,y,0)])\delta(z). \tag{4.4}$$

By taking the Fourier transform of Eq. (4.4), we find

$$\phi(\mathbf{q},k) = \frac{\rho(\mathbf{q}) - \kappa q^2\phi(\mathbf{q},z=0)}{\epsilon(q^2+k^2)}. \tag{4.5}$$

but

$$\begin{aligned}\phi(\mathbf{q},z=0) &= \frac{1}{2\pi}\int \phi(\mathbf{q},k)dk \\ &= \frac{1}{2\epsilon q}[\rho(\mathbf{q}) - \kappa q^2\phi(\mathbf{q},z=0)].\end{aligned} \tag{4.6}$$

Then, by rearranging for $\phi(q,z=0)$, the in-plane electric potential can be written as

$$\phi(\mathbf{q},z=0) = \frac{\rho(\mathbf{q})}{q(2\epsilon+q\kappa)} \tag{4.7}$$

For a 2D semiconductor that contains point charges q_i and q_j, the electrostatic potential energy is given by

$$v(q) = \frac{q_iq_j}{q(2\epsilon+\kappa q)} = \frac{q_iq_j}{2\epsilon q(1+r_*q)} \tag{4.8}$$

where $r_* = \kappa/(2\epsilon)$ is the Keldysh interaction screening length parameter. Taking the inverse Fourier transform of Eq. (4.8), the potential energy can be written as

$$v(r) = \frac{q_iq_j}{4\pi\epsilon r_*}V\left(\frac{r}{r_*}\right) \tag{4.9}$$

where r is the particle separation, and

$$V\left(\frac{r}{r_*}\right) = \frac{\pi}{2}\left[H_0\left(\frac{r}{r_*}\right) - Y_0\left(\frac{r}{r_*}\right)\right], \tag{4.10}$$

where $H_n(x)$ is a Struve function and $Y_n(x)$ is a Bessel function of the second kind (Neumann function). The interaction in the expression in Eq. (4.10) is known as the Keldysh interaction [200]. At long range ($r >> r_*$), this potential reduces to the Coulomb interaction:

$$V\left(\frac{r}{r_*}\right) \approx \frac{r_*}{r}. \tag{4.11}$$

However, at short range ($r << r_*$), the interaction is approximately logarithmic:

$$V\left(\frac{r}{r_*}\right) \approx [\log(2r_*/r) - \gamma] = \log\left(\frac{2r_*}{\exp(\gamma)r}\right), \tag{4.12}$$

where γ is Euler's constant. We refer to the interaction potential of Eq. (4.12) as the logarithmic interaction. For a system of N electrons (and holes) interacting via the Keldysh interaction, the Schrödinger equation is

$$\Big[-\sum_i \frac{\nabla^2_{\mathbf{r}_i}}{2m_i} + \sum_{i>j}^{N} \frac{q_i q_j}{4\pi\epsilon r_*} V\left(\frac{r_{ij}}{r_*}\right)\Big]\psi = E\psi, \tag{4.13}$$

where m_i and q_i are the band effective mass and charge of particle i, r_{ij} is the separation of particles i and j, and E is the energy eigenvalue.

4.1.2 Lattice sums

To model HEG in 2D material, the Keldysh interaction must be carried out in finite simulation cells subject to periodic boundary conditions. Therefore, it is necessary to provide a means for addressing the lattice sum for two-particle interactions of the form

$$v(\mathbf{r}) = \sum_{\mathbf{R}} v_K(|\mathbf{r} - \mathbf{R}|) \tag{4.14}$$

where $\mathbf{R}$ is the 2D lattice translation vectors. The Keldysh interaction is logarithmic at short range; however, it behaves identically to the Coulomb interaction at long range. This implies that the 2D periodic Keldysh interaction can be rewritten as a typical Coulomb interaction plus a correction Δv. This correction is equal to the difference of the finite Keldysh potential and the Coulomb potential $\Delta v = v_K - v_C$ summed over periodic images. The difference between Keldysh and Coulomb interactions falls off as (r^{-3}) at long range [4], and thus, summation of this difference over all periodic images of a pair of particles yields an absolute convergence. Therefore, Eq. (4.14) becomes

$$v(\mathbf{r}) = \sum_{\mathbf{R}} v_C(|\mathbf{r} - \mathbf{R}|) + \sum_{\mathbf{R}} \Delta v(|\mathbf{r} - \mathbf{R}|) \tag{4.15}$$

As the Keldysh interaction reduces to the Coulomb interaction at long range, this indicates that the long-range Keldysh behaviour inherits the same issue as the long-range Coulomb interaction in which the sums over the periodic images

do not converge completely. This problem can be overcome using the standard solution Ewald method [202]. In the CASINO software package [25], the Coulomb lattice sums of the 2D periodic system are evaluated using the standard 2D Ewald method developed by Parry [203], in which the lattice sum in Eq. (4.14) is replaced with the Ewald interaction potential plus Madelung constant (particle self-image energy). Therefore, the implementation of the Keldysh interaction in periodic systems requires an Ewald-like version. Additionally, the Madelung constant must be modified to ensure that the average electrostatic potential within the simulation cell is fixed at zero. All these required expressions were developed by R. J. Hunt [4]. The resultant Ewald–Keldysh interaction is well suited for simulating the HEG in 2D semiconductors [38].

4.1.3 Model material parameters

For free-standing $MoSe_2$, the hole and electron effective masses are respectively $m_h^* = 0.44m_0$ and $m_e^* = 0.38m_0$ [204], where m_0 is the free electron mass. The Keldysh screening parameter is $r_* = 39.79$ Å[205]. The encapsulation of $MoSe_2$ in hBN introduces additional screening, where the dielectric constant of the surrounding medium $\epsilon = 4\epsilon_0$ [206], decreases the Keldysh screening parameter to $r_* = 9.9475$ Å $= 1.7858\ a_0^*$. The size of the exciton in 2D materials with the Keldysh interaction between the charges is $r_0 = \sqrt{r_*/(2\mu)}$ [185]. For the embedding a $MoSe_2$ monolayer in flakes of hBN, the exciton size is $r_0 = 4.2$ a.u.. Using the Wigner-Seitz radius r_s, which is the average radius of the circle containing one electron, the densities were determined by

$$r_s = \frac{m_e^*}{\epsilon}\frac{1.06616 \times 10^8}{\sqrt{n}} = \frac{1.01 \times 10^7 \mathrm{cm}^{-1}}{\sqrt{n}}, \tag{4.16}$$

where r_s is in effective Hartree atomic units and n is the number density in experimentally relevant units of cm^{-1}.

4.2 QMC calculations

4.2.1 Trial wave functions

The calculations were performed using Slater-Jastrow (SJ) and Slater-Jastrow-backflow (SJB) [46] trial wave functions. The main results were obtained using the plane-wave (PW) orbitals for each particle. The trial wave function forms using PW orbitals are as follows:

$$\begin{aligned} \Psi_{\mathrm{PW}}^{\mathrm{SJ}} &= \mathrm{e}^{J(\mathbf{R})}\det\left[e^{i\mathbf{k}_i\cdot\mathbf{r}_\uparrow}\right]\det\left[e^{i\mathbf{k}_i\cdot\mathbf{r}_\downarrow}\right] \\ \Psi_{\mathrm{PW}}^{\mathrm{SJB}} &= \mathrm{e}^{J(\mathbf{R})}\det\left[e^{i\mathbf{k}_i\cdot(\mathbf{r}_\uparrow+\zeta(\mathbf{R}))}\right]\det\left[e^{i\mathbf{k}_i\cdot(\mathbf{r}_\downarrow+\zeta(\mathbf{R}))}\right] \end{aligned} \tag{4.17}$$

where $\mathrm{e}^{J(\mathbf{R})}$ is the Jastrow factor [37] that is used to provide a description of the electron–hole and electron–electron correlations, $\mathbf{R}$ is the particle coordinates, $\zeta(\mathbf{R})$ is the backflow displacement [46], and $\mathbf{r}_\uparrow$ and $\mathbf{r}_\downarrow$ denote the positions vector of the ith spin up and down electron.

We also tested another type of orbital called a pairing orbital (Pair), which was suggested by Spink *et al.* [3]. The trial wave function form is defined in terms of a product of Slater determinants containing pairing orbitals ϕ_i that describe the electron-electron and electron-hole correlation. The trial wave functions using pairing orbitals can be written as

$$\begin{aligned} \Psi_{\mathrm{Pair}}^{\mathrm{SJ}} &= \mathrm{e}^{J(\mathbf{R})}\det\left[\phi_i(\mathbf{r}_i^\uparrow-\mathbf{r}_h)\right]\det\left[\phi_i(\mathbf{r}_i^\downarrow-\mathbf{r}_h)\right] \\ \Psi_{\mathrm{Pair}}^{\mathrm{SJB}} &= \mathrm{e}^{J(\mathbf{R})}\det\left[\phi_i(\mathbf{r}_i^\uparrow-\mathbf{r}_h+\zeta(\mathbf{R}))\right]\det\left[\phi_i(\mathbf{r}_i^\downarrow-\mathbf{r}_h+\zeta(\mathbf{R}))\right] \end{aligned} \tag{4.18}$$

where $\mathbf{r}_h$ is the position vector of the hole. The pairing orbitals take a flexible form with optimisable parameters as

$$\phi_i(\mathbf{r}) = \exp[u_{G_i}(r)]\exp\left\{i\mathbf{G}_i\cdot\mathbf{r}[1-\eta_{G_i}(r)/r]\right\}, \tag{4.19}$$

where $u_{G_i}(r)$ refers to the orbital-dependent electron-hole Jastrow factor and η_{G_i} is the orbital-dependent electron-hole backflow function, where $\mathbf{G}_i$ indicates the ith shortest reciprocal lattice vector. The full description of the paring orbitals components can be found in [3].

For a system of particles interacting via the Ewald-Keldysh interaction, satisfying the Kato cusp conditions at coalescence points requires adding a minimal cusp-satisfying term to the ordinary two-body Jastrow u term [4] to become

$$u_{\mathbf{K}}(r_{ij}) = -\left(1 - \frac{r_{ij}}{L_{u\mathbf{K}}}\right)^{C} \Theta(L_{u\mathbf{K}} - r_{ij}) \Gamma^{\mathbf{K}}_{ij} r_{ij}^2 \log(r_{ij}), \tag{4.20}$$

where $L_{u\mathbf{K}}$ is the cutoff distance of the $u_{\mathbf{K}}$ term, C is the truncation order, and the pairing coefficient $\Gamma^{\mathbf{K}}_{ij}$ for distinguishable pairs of particles of masses m_i and m_j and charges q_i and q_j is given by

$$\Gamma^{\mathbf{K}}_{ij} = \frac{q_i q_j m_i m_j}{2r_*(m_i + m_j)}. \tag{4.21}$$

For indistinguishable particle pairs, the value of the pairing coefficient $\Gamma^{\mathbf{K}}_{ij}$ is halved.

For all the trial wave function types, the Jastrow function was composed of the electron–electron u term and p term in the case of PW orbitals, whereas the backflow function consisted of the cuspless two-body polynomial η function [46]. We also performed tests using the cuspless PW backflow Π term, which is similar to the p term for describing the long-range correlations [38]. The Jastrow exponents components were first optimised using the VMC variance–minimisation method [48], and then all parameters including the pairing orbitals and backflow parameters were optimised using the VMC energy–minimisation method [52]. The optimisation calculations of wave function parameters were performed separately for each wave function and system used.

4.2.2 DMC time step and target population

The DMC total-energy calculations were performed using a hexagonal simulation cell subject to the periodic boundary for systems with $N_e = 54,\ 62,$ and 110 electrons over a range of low densities. The DMC time steps were chosen to be small enough to ensure the time-step linear regime. The reasonable choice of time steps τ are such that the typical diffusion distance $\sqrt{2\tau}$ should be much smaller than the smallest physical length scale in the system. The smallest physical length in the model of the fluid phase of the single hole in the 2D HEG is the exciton Bohr radius. The target walker populations were varied inversely with respect to the time step, enabling simultaneous extrapolation to infinite population and zero time step. Our main results were obtained using simulation cell area $A = \pi r_s^2 N_e$.

4.2.3 Electron–hole relaxation energy

In the context of the photoluminescence experiments, consider an n-doped semiconductor system with a finite concentration of charge carriers in the conduction band, which undergoes an electron photoexcitation across the band gap. A single hole in a homogenous N_e-electron gas will bind with two electrons to create a negative trion. In response to the creation of the trion via photoexcitation, the remaining $(N_e - 2)$ electrons in the interacting electron gas system rearrange themselves in the new potential. The $(N_e - 2)$-electron gas system then relaxes into a new state of ground-state energy $E_{\mathrm{HEG}(N_e-2)}$. The minimum photon energy required in the photoexcitation process can be calculated as the sum of electron–hole correlation energy, the Fermi energy of electron gas, hole energy at the Fermi wave vector, and quasiparticle band gap [25].

In the optical absorption spectra, the change in the band gap due to photon absorption can be inferred by calculating the energy gained by allowing the creation of the electron-hole pair. In the theoretical modelling of creation of excitonic complexes in the 2D dilute electron gas system interacting via the Keldysh interaction, the electron–hole correlation energy, known also the relaxation energy, can be evaluated as

$$E_R = E_{h+\mathrm{HEG}(N_e)} - E_{\mathrm{HEG}(N_e)} \tag{4.22}$$

where $E_{h+\mathrm{HEG}(N_e)}$ is the total energy of the system that contains a single hole in a 2D HEG of area A and $E_{\mathrm{HEG}(N_e)}$ is the total energy of the pristine 2D HEG of the same area containing the same number of electrons. In the limit of low density, the electron–hole correlation (relaxation) reaches the energy of an isolated trion, and $E_{h+\mathrm{HEG}(N)}$ can be approximated as

$$E_{h+\mathrm{HEG}(N)} \approx E_{\mathrm{HEG}(N-2)} + E_{X^-} + E_{X^-}^{\mathrm{imm}}, \tag{4.23}$$

where E_{X^-} is the total energy of a negative trion and $E_{X^-}^{\mathrm{imm}}$ is the energy acquired by immersing the trion in HEG. At low density, $E_{X^-}^{\mathrm{imm}}$ is roughly equivalent to the Fermi energy of the HEG. For an infinite 2D HEG, the Fermi energy is given by

$$E_F = \epsilon(r_s) - \frac{r_s}{2}\frac{d\epsilon(r_s)}{dr_s} \tag{4.24}$$

where ϵ is the energy per electron as a function of r_s. The Fermi energy E_F is equal to the energy required to pluck one electron from a HEG system of constant area in the thermodynamic limit [3]. Therefore, the relaxation energy Eq. (4.22) can be reexpressed as

$$\begin{aligned} E_R &\approx -2E_F + E_{X^-} + E_{X^-}^{\text{imm}} \\ &\approx -E_F + E_{X^-}. \end{aligned} \tag{4.25}$$

In this study, the electron-hole relaxation energy is calculated directly using Eq. (4.22).

4.2.4 Pair-correlation function

The electron–hole pair-correlation functions (PCFs) were calculated by binning the electron–hole distances r sampled in VMC and DMC calculations as

$$g_{eh}(r) = \frac{A}{2\pi r N_e} \Big\langle \sum_{j=1}^{N_e} \delta(|\mathbf{r}_j - \mathbf{r}_h| - r) \Big\rangle, \tag{4.26}$$

which approaches unity when $r >> r_s$. The DMC PCFs were obtained at different time steps and then averaged. For an operator that does not commute with the Hamiltonian, such as the PCF, the errors in the VMC and DMC expectation values are linear in the error in the trial wave function. Therefore, the leading-order finite size errors that result from the dependence of PCF on the trial wave function can be removed by extrapolated estimation [36]

$$g_{eh}(r) = 2g_{\text{DMC}}(r) - g_{\text{VMC}}(r), \tag{4.27}$$

where g_{DMC} and g_{VMC} are the DMC and VMC PCFs, respectively. The errors in the extrapolated estimate Eq. (4.27) are quadratic in the error in the trial wave function.

The short-range PCF data at zero inter-particle distance, known as the contact PCF, can be inferred by extrapolating the electron-hole PCFs to zero separation for each system at each r_* value. To perform the extrapolation, we fitted $\ln[g_{eh}(r)]$ to the polynomial satisfying the Kimball's cusp conditions suggested by Drummond *et al.* [207] for the electron-hole PCF at short range. A compatible form for the

Keldysh interactions can be written as

$$\ln g_{eh}(r) = a_0 + \frac{\mu}{r_*} r^2 \ln(r) + a_2 r^2 + a_3 r^3 + ... + a_6 r^6, \tag{4.28}$$

where a_0, a_2, ... and a_6 are fitting parameters. The cusp term in Eq. (4.28) was obtained from the electron-hole cusp condition in Eq. (4.21). The estimated contact PDF is $g_{eh}(0) = \exp(a_0)$. To compute the error bars on $g_{eh}(0)$, we used the method outlined in Refs. [3, 207] by assigning a constant error σ to the PCF data and defining its value as

$$\chi^2 = \frac{\sum_i \left[g_{eh}^{\text{fit}}(r_i) - g_{eh}(r_i)\right]^2}{d\sigma^2} = 1, \tag{4.29}$$

where d indicates the number of degrees of freedom.

4.2.5 Finite–size effects

The largest common source of the bias in the QMC calculation is the finite-size effects that are incurred mainly due to the use of finite simulation cells subject to periodic boundary conditions (PBCs), causing the expectation values to depend on the shape and size of the used supercell. For 2D systems of N_e-electrons, the dominant PBC finite-size errors result from quasirandom single particle momentum quantisation effects, the neglecting of long-range correlations, and the artificial distortion of the exchange-correlation hole surrounding the electrons. The single-particle finite-size error can be effectively reduced using the Monte Carlo twist–average (TA) method; see Sec. 5.2.3 for more details. The residual systematic error arising from finite-size effects in the energy per particle was found to scale as $O(N^{-5/4})$ with system size [134]; hence, it can be removed via extrapolation to infinite system size. In our calculations, the energies per particle were calculated at different system sizes of $N_e = 54$, 62, and 110 electrons in hexagonal lattice at a range of low electron densities, which will introduce an inevitable finite-size effect. Therefore, it is important to extrapolate the relaxation energy results at each density to the thermodynamic limit assuming that the systematic finite-size effects are $O(N_e^{-1})$ by fitting the relaxation energy data to

$$E_R(N_e) = E_R(\infty) + CN_e^{-1}, \tag{4.30}$$

where $E_R(\infty)$ and C are fitting parameters. Such scaling was used in Ref [3]. The relaxation energy is effectively a defect formation energy of a single hole in the electron gas, see Chapter 5 for more discussion of finite-size effects.

To examine the quasirandom single-particle errors that arose from the momentum-quantisation finite-size effects in the relaxation energy, we implemented the TA method for a system of 54 electrons at $r_s = 15$ a.u. and simulation cell area $N_e \pi r_s^2$. The TA method was performed using 24 offsets randomly sampled throughout the first Brillouin zone, in which both the pristine 2D HEG and single-hole doped 2D HEG systems have the same set of twists. The Jastrow factor and backflow function were independently optimised at each twist. In the DMC simulations, a full-length period of equilibration is undertaken at each of the twists with the same amount of samples followed by a period of the statistics accumulation for the given target accuracy. Therefore, averaging the energy over a set of twists will effectively reduce the statistical noise as $\sigma_{\mathrm{TA}}/\sqrt{N_{\mathrm{TA}}}$, where σ_{TA} is the obtained average error on one twist and N_{TA} is the number of twists.

The comparison between the non-twist ($\mathbf{k}_s = 0$) and TA SJB-DMC energies is reported in Table 4.1. During the TA simulation, the energy per particle varies as the twist offset is changed, where the energy difference between the TA and non-twist results shows the convergence with cell size. Moreover, the use of the Hartree-Fock (HF) energies as a control variate leads to improving the accuracy of the TA energies [208]. The use of an HF control variate reduced the standard error in the TA DMC energy per particle. However, we found that the uncertainty due to the statistical noise in the energy per particle results were cancelled out in the calculations of the relaxation energies. The twist average relaxation energy was calculated at each twist and then averaged over the set of twists. As shown in Table 4.1, the twist-averaged and non-twist relaxation energy results were close. Therefore, there is no point in adding the complexity involved in the TA method when a single, longer, and non-twist calculation can obtain an equivalent result. Thus, all the main calculations were performed using a simulation-cell Bloch vector of $\mathbf{k}_s = 0$.

Table 4.1: Energies from SJB-DMC simulation in 54 electrons at $r_s = 15$ a.u.. The COV refers to that we used the HF kinetic and potential energy of the Keldysh 2D HEG as control variates when averaging over a set of twists. The twist average relaxation energy was calculated at each twist and then averaged over the set of twists.

-	$\mathbf{k}_s = 0$		TA	
	hole-2D HEG	2D HEG	hole-2D HEG	2D HEG
DMC energy(a.u./particle)	−0.056634(3)	−0.0529602(5)	−0.056702(3)	−0.053030(3)
DMC^{COV} energy(a.u./particle)	-	-	−0.056701(2)	−0.0530284(4)
DMC relaxation energy (a.u.)	−0.2550(2)		−0.2550(1)	

4.3 Results and discussion

4.3.1 Trial wave function and simulation cell area choice

Table 4.2 show the energies per particle evaluated using VMC and DMC with different trial wave functions ($\Psi^{\text{SJ}}_{\text{PW}}$, $\Psi^{\text{SJ}}_{\text{Pair}}$, $\Psi^{\text{SJB}}_{\text{PW}}$ and $\Psi^{\text{SJB}}_{\text{Pair}}$) for a single hole immersed in a 2D HEG at $N_e = 62$ electrons and $r_s = 15$ electron density. As shown in Table 4.2, the VMC and DMC energies with the SJB wave functions are lower than those with the SJ wave functions. The inclusion of the backflow function has a more profound effect on the VMC than on the DMC results, in which the energy difference in VMC results is equivalent to four times the difference in the DMC results. Hence, we used the backflow function in all our production calculations. The PW orbitals were found to be relatively insensitive to optimising the cutoff length of the η backflow term, and the usage of the Π backflow component had an insignificant effect on the results.

The VMC and DMC results of pairing orbitals with only the η backflow term showed dependence on the optimisation of the η cutoff length to recover the expected behaviour as the lower bound or equivalent to those in the PW orbital results. However, we found that using the long-range Π backflow term in $\Psi^{\text{SJB}}_{\text{Pair}}$ calculation is important to improve the trial wave function by retrieving more correlation effects and maintain the agreement with $\Psi^{\text{SJB}}_{\text{PW}}$ results. It can be seen that the pairing

orbitals $\Psi^{\rm SJB}_{\rm Pair}$ generally gave lower energies than the PW orbitals $\Psi^{\rm SJB}_{\rm PW}$ but with negligible energy differences, indicating that the DMC energies are highly accurate. The DMC calculations using $\Psi^{\rm SJB}_{\rm Pair}$ wave functions were found to be more expensive than the DMC using $\Psi^{\rm SJB}_{\rm PW}$ wave functions with almost identical results. Therefore, we used the $\Psi^{\rm SJB}_{\rm PW}$ with only the η backflow term in all our main calculations.

Table 4.3 shows the SJB-VMC and SJB-DMC results for two different choices of simulation cell area, $\pi r_s^2(N_e-1)$ and $\pi r_s^2 N_e$. The cell area $\pi r_s^2(N_e-1)$ has been used previously in Ref. [3] to ensure that the electron charge density is correct at the long range far from the doped impurity [209, 210]. As illustrated in Table 4.3, the two mentioned cell areas show a noticeable energy difference in the energy per particle for the single hole in 2D HEG and pure 2D HEG systems, which is expected to vanish in the limit of the infinite system size. However, the relaxation energies and on-top PCF results were found to be almost identical in both cell areas. The SJB-VMC relaxation energy data showed a small energy difference of about $-0.00086(8)$ a.u.. In the more accurate calculations, the SJB-DMC relaxation energy results were insensitive to the used cell area with a negligible energy difference of around $0.0003(4)$ a.u.. In any case, finite size effects result from the choice of simulation cell area will be removed in the extrapolation to the thermodynamic limit, in which the energies become independent of the cell area and number of electrons and are only functions of r_s. Therefore, we used simulation cells of area $A = \pi r_s^2 N_e$ in all our main calculations.

Table 4.2: The VMC and DMC results for a system of $N_e = 62$ electrons at $r_s = 15$ and area $A = N_e \pi r_s^2$. The results show the effect of optimising the backflow cutoff lengths and including the backflow Π term at different level of the trial wave function.

Method	WF	$E_{\text{cut}}^{\text{BF}}$ optimised	Π present	Energy (a.u./part.)	Variance (a.u.)
VMC	$\Psi_{\text{PW}}^{\text{SJ}}$	F	F	$-0.055263(1)$	0.02453(3)
VMC	$\Psi_{\text{Pair}}^{\text{SJ}}$	F	F	$-0.0553345(9)$	0.02316(3)
DMC	$\Psi_{\text{PW}}^{\text{SJ}}$	F	F	$-0.056181(4)$	
DMC	$\Psi_{\text{Pair}}^{\text{SJ}}$	F	F	$-0.056182(4)$	
VMC	$\Psi_{\text{PW}}^{\text{SJB}}$	F	F	$-0.055553(1)$	0.02480(3)
VMC	$\Psi_{\text{PW}}^{\text{SJB}}$	T	F	$-0.055556(1)$	0.02386(3)
DMC	$\Psi_{\text{PW}}^{\text{SJB}}$	F	F	$-0.056257(4)$	
DMC	$\Psi_{\text{PW}}^{\text{SJB}}$	T	F	$-0.056257(4)$	
VMC	$\Psi_{\text{Pair}}^{\text{SJB}}$	F	F	$-0.0555296(9)$	0.02453(3)
VMC	$\Psi_{\text{Pair}}^{\text{SJB}}$	T	F	$-0.0555654(9)$	0.02429(3)
DMC	$\Psi_{\text{Pair}}^{\text{SJB}}$	F	F	$-0.056243(4)$	
DMC	$\Psi_{\text{Pair}}^{\text{SJB}}$	T	F	$-0.056257(4)$	
VMC	$\Psi_{\text{PW}}^{\text{SJB}}$	F	T	$-0.055555(1)$	0.02456(3)
VMC	$\Psi_{\text{PW}}^{\text{SJB}}$	T	T	$-0.055558(1)$	0.02501(3)
DMC	$\Psi_{\text{PW}}^{\text{SJB}}$	F	T	$-0.056269(4)$	
DMC	$\Psi_{\text{PW}}^{\text{SJB}}$	T	T	$-0.056256(4)$	
VMC	$\Psi_{\text{Pair}}^{\text{SJB}}$	F	T	$-0.055589(1)$	0.02531(3)
VMC	$\Psi_{\text{Pair}}^{\text{SJB}}$	T	T	$-0.055599(1)$	0.02487(3)
DMC	$\Psi_{\text{Pair}}^{\text{SJB}}$	F	T	$-0.056269(4)$	
DMC	$\Psi_{\text{Pair}}^{\text{SJB}}$	T	T	$-0.056268(4)$	

Table 4.3: The SJB-VMC and SJB-DMC results for a system of $N_e = 62$ electrons at $r_s = 15$ and $\mathbf{k}_s = 0$ using different simulation areas.

Method	$N_e\pi r_s^2$		$(N_e-1)\pi r_s^2$	
	hole-2D HEG	2D HEG	hole-2D HEG	2D HEG
VMC energy (a.u./particle)	−0.055553(1)	−0.0528702(2)	−0.0558644(9)	−0.0532006(2)
VMC variance (a.u.)	0.02480(2)	0.000653(4)	0.02430(3)	0.000643(2)
DMC energy (a.u./particle)	−0.056257(4)	−0.0530508(8)	−0.056576(4)	−0.0533803(9)
VMC relaxation energy (a.u.)	−0.22188(6)		−0.22102(6)	
DMC relaxation energy (a.u.)	−0.2550(3)		−0.2547(3)	
On-top $g_{eh}(0)$	62.3(1)		61.8(2)	

4.3.2 The electron-hole relaxation energies

Table 4.4 shows the relaxation energies of a single hole immersed in 2D HEG for different system sizes at a range of low charge densities. We calculated the electron–hole relaxation energy using $\Psi_{\text{PW}}^{\text{SJB}}$ wave function, $N_e\pi r_s^2$ simulation cell area and $\mathbf{k}_s = 0$ Block wave vector. The SJB-DMC relaxation energies are plotted against the inverse of system sizes in Fig. 4.2. Our DMC data show that the relaxation energy results converged well with system sizes and the single-particle finite size effects are negligible. Using the fitting form from Ref. [207], the relaxation energy data can be well fitted to a function form, as follows,

$$E_R(r_s) = \frac{A_{-1}r_s^{-1} + A_0 + A_1 r_s + E_{X^-} B_2 r_s^2}{1 + B_1 r_s + B_2 r_s^2}, \tag{4.31}$$

where $A_{-1} = 110.864$, $A_0 = -6.41894$, $A_1 = -1.64917$, $B_1 = 9.10327$ and $B_2 = 0.689267$. The $E_{X^-}^K = -1.213\ R_y^*$ is the energy of the isolated negative trion, which was calculated using parameters in Sec. 4.1.3 and a supplied utility from Ref. [185]. In addition, the energy of the isolated exciton is $E_X^K = -1.1194\ R_y^*$ in Keldysh interaction. The fitting form of electron-hole relaxation energy reaches the energy of the isolated negative trion at extreme low densities. Fig. 4.1 shows the electron-hole relaxation energy along with the total energies of negative trion and neutral exciton.

Fig. 4.3 illustrates that the sum of the relaxation energy and the Fermi energy of

the 2D HEG approaches the total energy of an isolated negative trion at the extreme low carrier density. The Fermi energy data were obtained using the parameterisation of the paramagnetic Fermi fluid energy $\epsilon(r_s)$ reported in Ref. [4]. The PCFs results, as illustrated in Sec. 4.3.3, indicate that for r_s length larger than the trion radius, the effect of the surrounding electron gas screening on the interaction between the trion's charge carrier is weak, resulting in the formation of the trion. Therefore, the results in Fig. 4.3 imply that Eq. (4.25) is not exact at the range of used r_s values. In the optical absorption spectra, the change (renormalisation) in the band gap ΔE_g due to the photon absorption and the electron-hole pair correlation effects can be understood as

$$\Delta E_g = E_{exc} - E_h - (E_R + E_F), \tag{4.32}$$

where E_{exc} is the minimum energy required to create an electron-hole pair via photoexcitation and $E_h = k_F^2/(2m_h)$ is the kinetic energy of a hole at Fermi wave vector k_F. At the finite concentration of charge carriers, this change is well approximated to the energy of an isolated negative trion.

The QMC study for the isolated negative trion and electron-hole relaxation energies in 2D HEG of free standing material have been reported previously [3]. Using parameterisation of the fitting function (S16) in Ref. [3], the total energy of the isolated negative trion with mass ratio $m_h/m_e = 1.158$ in the presence of screened Coulomb interaction is $E^C_{X^-} = -4.477\ R^*_y$, lower than the $E^K_{X^-}$ by around $3.264\ R^*_y$. This large difference in the results might be due to the dependence of the trion state on the host environment, as screening by material encapsulation reduced the Keldysh screen parameter (r^*) resulting in an increase in the negative trion total energy.

Figure 4.1 shows also the electron-hole relaxation energy at high densities by interpolating the data from Ref. [3] at mass ratio $m_h/m_e = 1.158$ plus a correction obtained by considering the energy difference between the Keldysh and Coulomb interactions. The correction was evaluated using the exact trion energies as $E^K_{X^-} - E^C_{X^-}$. The validity of this correction originates from the fact that the localised nature of an isolated negative trion dominates the low-density limit where the long-range Keldysh interaction reduces to Coulomb interaction. In addition, the relaxation energy can be approximated to Eq. (4.25) at extreme low densities ($r_s \to \infty$). It

is also important to point out that the Fermi energy E_F is only weakly dependent on the form of the screened interaction. E_F at high densities is dominated by the kinetic energy, which is the same for both interactions, whereas at low densities the difference between Fermi energies of the Keldysh and Coulomb interactions is insignificant because the Keldysh interaction behaves identically to the Coulomb interaction. Fig. 4.1 demonstrates that the relaxation energies at high densities are well approximated by the correction $(E^K_{X^-} - E^C_{X^-})$, showing some consistency with our results at low densities. It also illustrates that the localised form of the negative trion does not arise at high densities due to the strong screening effects by the electron gas, as the electron-hole relaxation energy diverges towards $-\infty$.

Table 4.4: System-size dependence of the SJB-DMC electron-hole relaxation energies calculated using PW orbitals in a.u. for a range of densities.

N_e	r_s (a.u.)				
	15	20	25	30	35
54	−0.2550(2)	−0.2689(3)	−0.2766(3)	−0.2858(4)	−0.2880(4)
62	−0.2550(2)	−0.2689(5)	−0.2778(3)	−0.2835(4)	−0.2885(2)
110	−0.2543(3)	−0.2687(4)	−0.2780(3)	−0.2844(4)	−0.2883(4)
∞	−0.2538(6)	−0.2685(9)	−0.2793(7)	−0.2832(9)	−0.2885(8)

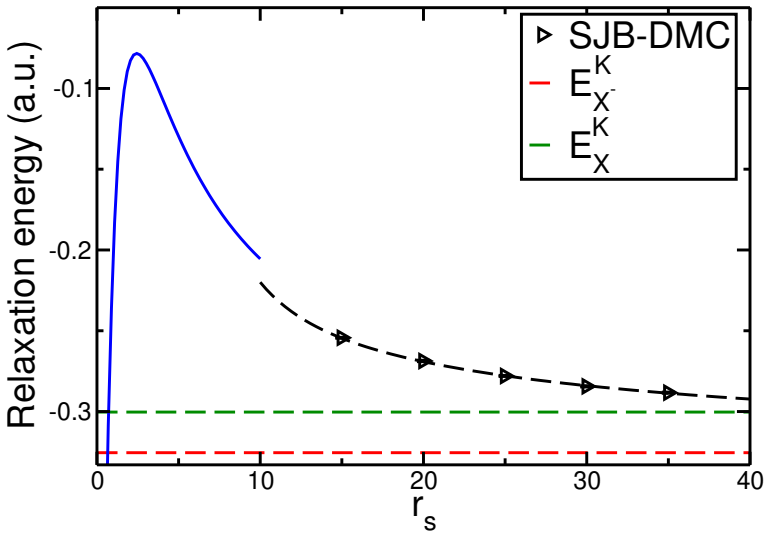

Figure 4.1: Relaxation energy data as a function of density parameter (r_s) of a hole immersed in 2D 110-electron gas. The dashed black line shows the least–squares fit of the SJB-DMC relaxation energy to Eq. (4.31). The dashed green and red lines are the total energy of the neutral exciton and negative trion, respectively. The blue curve is the interpolation of electron-hole relaxation energy at high density from Ref. [3] of mass ratio $m_h/m_e = 1.158$ plus the difference between the Keldysh and Coulomb trion total energies ($E_{X^-}^K - E_{X^-}^C$).

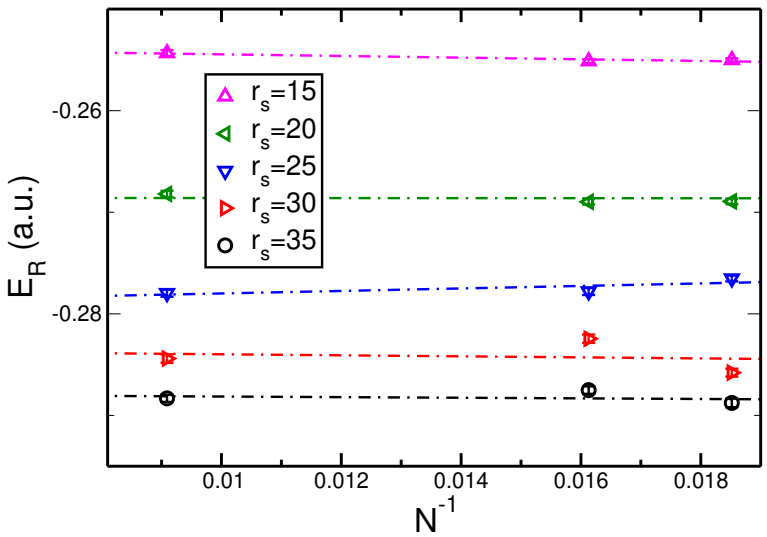

Figure 4.2: Relaxation energy data against the inverse of the system size for a hole immersed in HEGs at different density parameter (r_s). The dashed fitting lines shows the linear least–squares fit of the DMC data.

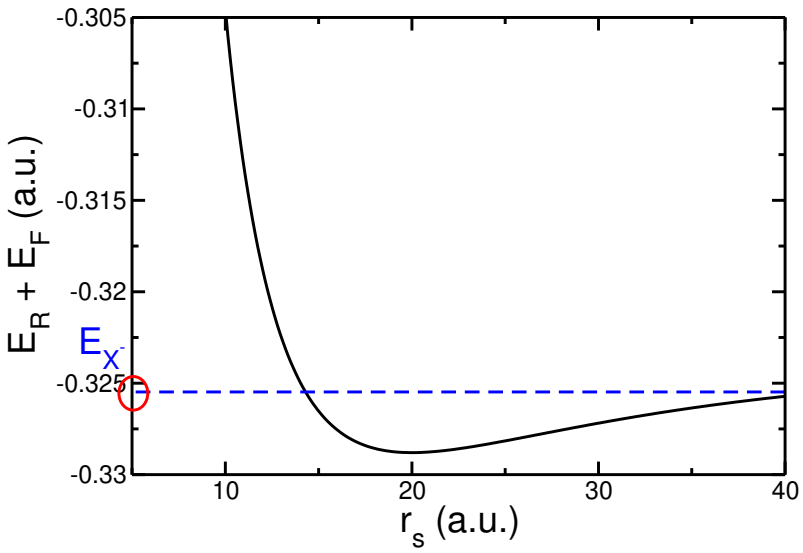

Figure 4.3: The sum of the relaxation energy and the Fermi energy of HEG as a function of the density parameter r_s. The Fermi energy data of HEG were obtained using the parameterisation of the paramagnetic Fermi fluid energy in Ref. [4]. The blue dashed line is the total energy of isolated negative trion in the Keldysh interaction.

4.3.3 Pair correlation functions (PCF)

4.3.3.1 The total PCF data

The total electron-hole PCFs were evaluated using the extrapolated estimation of Eq. (4.27) due to the small but statistically significant differences between the VMC and DMC results; the DMC PCFs were averaged over different time steps. We found that the effect of the extrapolated estimate at low densities is significant, as seen in Table 4.5. The total electron-hole PCFs $g_{eh}(r)$ are plotted for $N_e = 110$ at different densities in Fig. 4.4 and for different system sizes at $r_s = 20$ a.u. in Fig 4.5. The importance of the electron-hole PCF is that its value at r represents the proportion of the electronic density at a distance of r from the hole to that of the surrounding electron gas. Therefore, the first measured minimum of the electron-hole PCF gives a very direct indication of the degree of isolation of the localised trion. For the low-density limit, our results show that all of the $g_{eh}(r)$ data have regions less than one and become more pronounced at the lowest density, which indicates the localisation of the negative trion in this region away from the surrounding electrons.

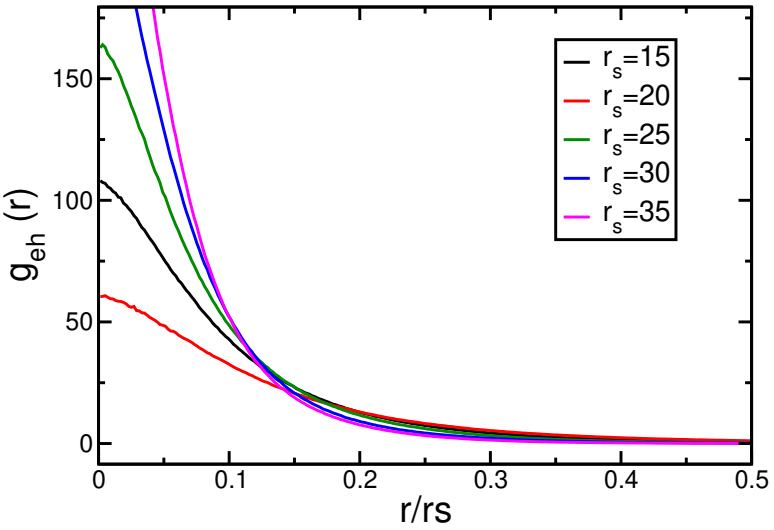

Figure 4.4: The total electron-hole PCF $g_{eh}(r)$ as a function of the density parameter (r_s) of the 110-electron gas.

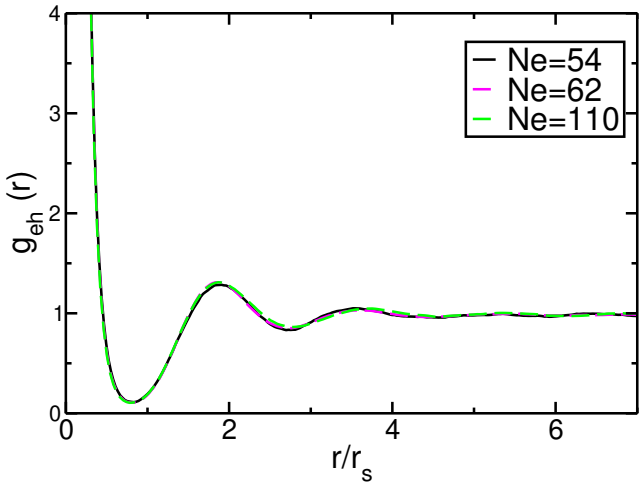

Figure 4.5: The total electron-hole PCF $g_{eh}(r)$ as a function of the system size at a density parameter ($r_s = 20$) of the electron gas.

4.3.3.2 On-top pair density

Adapting the fitting function from Ref [207] slightly to a compatible form for the Keldysh interaction, we extrapolated all the total electron-hole contact PCF results by fitting Eq. (4.28) to $\ln[g_{eh}(r)]$ on the short range $0 < r < r_s/2$ and then estimated the contact PCF as $g_{eh}(0) = \exp[a_0]$. The uncertainty in $g_{eh}(0)$ data as estimated using Eq. (4.29) with $N - 1$ degrees of freedom, where N is the number of data fittings minus the number of fitting parameters in Eq. (4.28). It is clear that the

contact PCFs increase rapidly as the density decreases, as shown in Table 4.6. Large values of $g_{eh}(0)$ at low densities suggest a strong electron-hole correlation and the formation of the negative trion. Using the fitting form from Ref. [207], we fit the electron-hole contact PCF at low-density limit to:

$$g_{eh}(0) = 1 + 1.23r_s + a_1 r_s^{3/2} + a_2 r_s^2 + a_3 r_s^{7/3} + a_4 r_s^{8/3} + a_5 r_s^3, \tag{4.33}$$

where $a_1 = 128.687$, $a_2 = -188.778$, $a_3 = 124.459$, $a_4 = -32.372$ and $a_5 = 3.04482$ are the fitting parameters. The electron-hole contact PCF results are plotted against r_s in Fig. 4.6. We also compared the contact PCF obtained for different system sizes at various low density parameter (r_s) in Fig. 4.7. The $g_{eh}(0)$ is particularly important in constructing the local and semilocal exchange-correlation functionals for use in DFT calculations to describe a single hole embedded in inhomogeneous systems [211, 212]. It is also important to determine the recombination rate for hole immersed in a HEG, in which the $g_{eh}(0)$ is proportional to the electron-hole recombination rate.

Table 4.5: Contact PCF for a single hole in 2D 110-electron HEG at $r_s = 15$ using different methods.

Method	$g_{eh}(0)$
SJB-VMC	35.7(1)
SJB-DMC	48.15(2)
Extrap.	60.5(1)

Table 4.6: System-size dependence of the calculated contact PCF data using $\Psi_{\mathrm{PW}}^{\mathrm{SJB}}$ for a range of densities.

N_e	r_s (a.u.)				
	15	20	25	30	35
54	63.5(2)	107.4(3)	161.8(3)	228.5(5)	263.5(5)
62	62.3(1)	105.7(2)	161.3(2)	213.8(3)	288.7(2)
110	60.5(1)	107.7(1)	166.7(4)	229.9(2)	313.2(4)

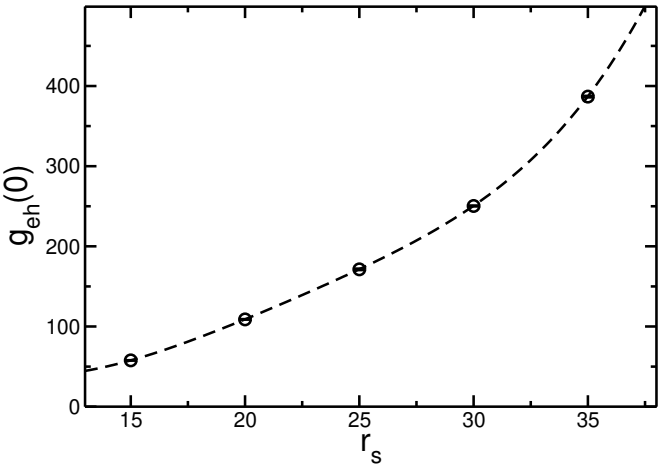

Figure 4.6: The electron-hole contact PCF, $g_{eh}(0)$, at a range of density parameter (r_s) values. The $g_{eh}(0)$ results were obtained by extrapolating to the thermodynamic limit using the scale N^{-1}. The dashed line shows the results obtained by fitting the extrapolated $g_{eh}(0)$ data at different density parameter (r_s) values to Eq. (4.33).

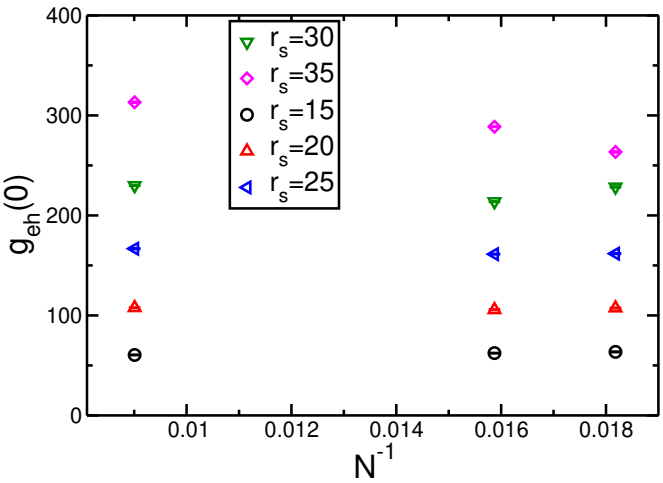

Figure 4.7: Electron-hole contact PCF $g_{eh}(0)$ as a function of the inverse of the system size for a range of density parameter (r_s) values of the electron gas.

4.4 Conclusion

In summary, QMC calculations were performed to simulate finite concentrations of charge carriers interacting through the Keldysh interaction in 2D materials. At the low density limit, the electron-hole relaxation energy, PCF and the contact PCF were calculated. The calculated electron-hole relaxation energy was found to approach

the isolated trion energy at extreme low densities. In addition, the relaxation energy results show some consistency with the earlier work using Coulomb interaction at high densities. Our results indicate that the screening effects of the surrounding electron gas on the formation of trion in the range of used r_s values is weak.

Chapter 5

Point defect in graphene

5.1 Introduction

Graphene [1], a sheet of carbon atoms arranged in a honeycomb structure, is one of the most intriguing materials for future technological applications [214–216]. However, the production of large, defect-free graphene layers on insulating substrates remains a considerable technical difficulty [217]. Point defects may occur spontaneously during the synthesis of graphene, or they can be deliberately injected into pure graphene through processing [218]. As point defects can have a significant effect on the electrical and optical properties of graphene [219, 220], it is vital to understand their structure and features to comprehend fully the performance of graphene-based devices. Graphene defect structures have been observed using high-resolution transmission electron microscopy and related techniques [221, 222]; however, these approaches inevitably produce more defects. Theoretical approaches have played an important role in graphene defect research. In particular, density functional theory (DFT) has been utilised in a large number of studies to examine defect formation energies and other features in a variety of applications and devices, including graphene [223–225], graphite [6, 226, 227] and other two-dimensional (2D) or layered materials [228–230].

The Dirac point at the Fermi level of pure graphene is the most significant char-

[1] This work was done in collaboration with D. M. Thomas and N. D. Drummond. Only minor modifications were introduced to Ref. [213]. The pristine graphene QMC total energies used in this work were calculated by D. M. Thomas [213].

acteristic of its electronic structure. Many types of defects at finite concentrations break the sublattice symmetry or shift the Fermi level, significantly altering the electronic properties of graphene [231]. Substitutional impurity atoms are among the most common defects in graphene, and they have been extensively studied using DFT [232]. Several studies [233–235] have shown that nitrogen and boron impurities in graphene act as donors and acceptors, respectively. DFT has been used to investigate the electronic and magnetic properties of a graphene sheet doped with iron, cobalt, silicon, and germanium impurities at a 3% concentration, finding that the substitution of a carbon atom with silicon or germanium can open a band gap in the electronic spectrum of graphene, while the insertion of iron or cobalt produces a metallic phase [236]. Silicon substitutions (SiSs) in graphene are an attractive approach for engineering the band structure [237]. The silicon atom, which has the same number of valence electrons as carbon, has been shown to be able to modulate the electronic structure of graphene without significantly changing its carrier mobility [220].

Stone–Wales (SW) defects in graphene are some of the most commonly observed intrinsic topological defects [231]. SW defects influence the electronic, structural, chemical and mechanical properties of graphene [238–243]. SW defects result in the tendency for monolayer graphene to bend; therefore can be used in the fabrication of nonplanar carbon nanostructures [244]. SW defects show mutual attraction [245], and the formation of SW defects clusters at high temperature is one of the first steps in the melting of graphene [246]. SW defects have also been observed to migrate over the graphene lattice. The SW migration energy barrier can be determined by the activation energy barrier E_{a} of thermally induced processes and by the threshold energy of the electron irradiation processes [247]. Once again, DFT has played a key role in elucidating the properties of SW defects.

The most significant thermodynamic attribute of a point defect is its formation energy $\mathcal{E}^{\mathrm{f}}$, which can be calculated as the free energy difference between the defective material and the pristine material, in addition to any changes in the energies of atom reservoirs that are added or subtracted when the defect is generated. For instance, the defect formation energy of an SiS defect is equal to the difference between the free energy of a large region of graphene containing a single SiS defect and the free

energy of the corresponding large region of pristine graphene, plus the free energy per atom of graphene and minus the free energy per atom of bulk silicon.

This chapter focuses on the quantum Monte Carlo (QMC) calculations of the formation energies of isolated SiSs and SW defects. Using first–principles density functional calculations, the energy barrier to SW defect formation has been investigated. Our aim is to provide a QMC assessment of defect-formation energy to evaluate the validity of the DFT method, which has been widely used in studies of graphene defects. Because this work necessitates the calculation of the energy per atom of both graphene and bulk silicon, we also take this opportunity to report the QMC atomisation energy of bulk diamond-structure silicon.

5.2 Computational methodology

5.2.1 Defect formation energies

The investigation of the changes in the free-energy surface of graphene provides a substantial understanding of the formation and migration of defects. The 'pure' formation energy $\mathcal{E}^{\mathrm{pf}}$ of an isolated defect in graphene is defined as the free-energy difference between a large graphene layer with a single defect and an analogous sheet of pristine graphene. The pure defect formation energy is approximately equal to the sum of the difference between the static-nucleus electronic ground-state energies of defective and pristine graphene, which we evaluate using both DFT and DMC, and the temperature-dependent difference in vibrational Helmholtz free energies, which we evaluate using DFT.

The defect formation energy $\mathcal{E}^{\mathrm{f}}$ can be calculated as the summation of $\mathcal{E}^{\mathrm{pf}}$ and the changes in the free energies of the reservoirs of the atoms that are added or removed. For the SW defect and SiS, these are:

$$\mathcal{E}^{\mathrm{f}}_{\mathrm{SiS}} = \mathcal{E}^{\mathrm{pf}}_{\mathrm{SiS}} + \mu_{\mathrm{C}} - \mu_{\mathrm{Si}} \tag{5.1}$$

$$\mathcal{E}^{\mathrm{f}}_{\mathrm{SW}} = \mathcal{E}^{\mathrm{pf}}_{\mathrm{SW}}, \tag{5.2}$$

where the chemical potentials μ_{C} and μ_{Si} are the Helmholtz free energies per atom of monolayer graphene and bulk diamond-structure silicon, respectively. The chemical potential is defined as the sum of the static-nucleus electronic ground-state energy

per atom and the temperature-dependent Helmholtz free energy per atom. Because the pure defect generation energy is dependent on the pseudopotentials chosen, it has no physical significance in itself. However, it is important from a theoretical standpoint to distinguish between the finite-concentration and finite-size effects caused solely by the calculations in the finite simulation subject of the periodic boundary conditions from the finite-size errors in the energy per atom of graphene and silicon.

5.2.2 Free energies of atomisation

The atomisation energy of a solid is an important quantity used to evaluate the binding strength and thermal stability of a crystal. It is defined as the energy required to release an atom from a solid. We calculate the free energy of the atomisation of bulk silicon as the difference in the energy of an isolated, spin–polarized silicon atom in its $^3P_0$ ground state and the Helmholtz free energy per atom in bulk silicon. This provides a pseudopotential-independent (in principle) free energy per atom that can be used to compare the stability of different condensed phases. Note, however, that the temperature dependence of the free energy of the reference gaseous atomic state is neglected.

5.2.3 Twisted periodic boundary conditions

Calculations of infinite periodic crystals in one-particle theories, such as DFT, can be simplified to calculations of a single primitive cell that is subject to Bloch boundary conditions. The expectation values can then be calculated per unit cell by integrating them over the entire first Brillouin zone (BZ) or, equivalently, averaging them over a discrete set of dense points in **k**-space. However, this approach cannot be implemented in many-particle methods, such as QMC, as the long range of electrons correlation may exceed the primitive cell size. Therefore, QMC calculations must be performed in simulation cells comprised of several primitive cells that are subject to the periodic boundary conditions described in [26]. For a supercell that contains N electrons, the Hamiltonian must obey:

$$\hat{H}(\mathbf{r}_1, ..., \mathbf{r}_i + \mathbf{R}_s, ..., \mathbf{r}_N) = \hat{H}(\mathbf{r}_1, ..., \mathbf{r}_i, ..., \mathbf{r}_N) \tag{5.3}$$

$$\hat{H}(\mathbf{r}_1 + \mathbf{R}_p, ..., \mathbf{r}_i + \mathbf{R}_p, ..., \mathbf{r}_N + \mathbf{R}_p) = \hat{H}(\mathbf{r}_1, ..., \mathbf{r}_i, ..., \mathbf{r}_N) \tag{5.4}$$

where $\mathbf{r}_i$ is the electronic coordinate of electron i, and $\mathbf{R}_p$ and $\mathbf{R}_s$ are the primitive cell and supercell lattice vector, respectively. As a result of these translational symmetries, the many-body wave function of the simulation cell must satisfy the following many-body Bloch conditions:

$$\Psi_{\mathbf{k}_s}(\mathbf{r}_1, ..., \mathbf{r}_N) = U_{\mathbf{k}_s}(\mathbf{r}_1, ..., \mathbf{r}_N) \ \exp\left(i\mathbf{k}_s \cdot \sum_{i=1}^{N} \mathbf{r}_i\right), \tag{5.5}$$

where $\mathbf{k}_s$ is the supercell Bloch wave vector that lies within the supercell first BZ. $U_{\mathbf{k}_s}$ is an invariant function under the translation of any electron through a vector $\mathbf{R}_s$.

$$\Psi_{\mathbf{k}_p}(\mathbf{r}_1, ..., \mathbf{r}_N) = V_{\mathbf{k}_p}(\mathbf{r}_1, ..., \mathbf{r}_N) \ \exp\left(i\mathbf{k}_p \cdot \frac{1}{N}\sum_{i=1}^{N} \mathbf{r}_i\right), \tag{5.6}$$

where $\mathbf{R}_p$ is a primitive cell Bloch wave vector that lies within the first BZ of the primitive cell. $V_{\mathbf{k}_p}$ is an invariant function under the simultaneous translation of all N electrons by a vector $\mathbf{R}_p$. The use of a supercell Bloch vector $\mathbf{k}_s \neq 0$ is referred to as the twisted boundary condition [62], where the wave function picks up a phase $\exp(i\mathbf{k}_p \cdot \mathbf{R}_s)$ whenever a single particle is translated by a supercell lattice vector $\mathbf{R}_s$.

The trial wave function should be selected to fulfil Eqs. (5.5) and (5.6) simultaneously, with $U_{\mathbf{k}_s}$ and $V_{\mathbf{k}_p}$ differing only by a phase factor. To do so, the one-particle orbitals in the Slater determinant must be chosen to be of Bloch form $\Psi_{\mathbf{k}}(\mathbf{r}) = u_{\mathbf{k}}(\mathbf{r}) \ \exp[i\mathbf{k} \cdot \mathbf{r}]$, where $u_{\mathbf{k}}$ has the periodicity of the primitive cell. The twisted boundary conditions require that for a supercell consisting of $l \times m \times n$ primitive cells, the single-particle orbitals must be generated for a single primitive unit cell with an $l \times m \times n$ Monkhorst-Pack grid [248] offset from the origin by the supercell Bloch vector (twist) $\mathbf{k}_s$, which lies within the supercell BZ. The twist offset $\mathbf{k}_s$ is permitted to vary randomly across the first BZ of the simulation cell. For a fixed number of electrons, the total expectation values are computed as an average over all twist vectors $\mathbf{k}_s$ that are uniformly distributed over the supercell BZ. This approach is called the canonical-ensemble twist averaging (TA) method [62], and it has been shown that this method of averaging greatly reduces the oscillatory single-particle finite-size effects of ground-state expectation values [134].

5.2.4 The activation energy for the SW transformation

Defects migration is typically regulated by an activation barrier that varies with the type of defect and grows exponentially with the temperature [247]. The activation barrier refers to the amount of energy that reactants must obtain prior to producing the products. Hence, the activation barrier energy of SW transformation can be calculated as the difference between the ground-state energy of the transition state, which is a saddle point with an energy maximum in the direction of the reaction coordinate and minimum energy in all other directions, and the energy of the pristine graphene ground state. Using modified geometry optimisation techniques, such as the synchronous-transit approach for searching reaction pathways, the saddle point in defect reactions can be determined. The maximum energy along the reaction pathway is referred to as the activation energy E_{a}, and the accompanying structure is referred to as the transition state. The obtained barriers energy can be then used to study the relation between the reaction rates under experimental conditions and the temperature. Using a simple Arrhenius equation, the lifetime t of a state can be calculated as:

$$\frac{1}{t} = A \exp\left(\frac{-E_{\mathrm{a}}}{k_{\mathrm{B}}T}\right) \tag{5.7}$$

where A is the characteristic optical phonon frequency, k_{B} is the Boltzmann constant and T is the deformation temperature. The pre-exponential A can be estimated using the Vineyard formula [249].

5.2.5 DFT calculations

5.2.5.1 Total energy, geometry optimisation and phonon calculations

Using the plane-wave-basis code CASTEP [128], DFT calculations were performed using the PBE generalised gradient approximation exchange-correlation functional [17]. Nuclei and core electrons were represented by ultrasoft pseudopotentials [129] in the calculations of total energy, geometry optimisation, and phonons. The plane-wave cutoff energies of 556 eV and 305 eV were used for graphene sheets and bulk silicon, respectively. The geometry structure for each defective graphene was optimised to a force tolerance of 0.0025 eV $\mathrm{Å}^{-1}$ using lattice vectors equivalent

to a pristine graphene carbon–carbon bond length of 1.42 Å [250, 251]. Using Monkhorst–Pack grids with about $(51/\sqrt{N}) \times (51/\sqrt{N})$ points, the total energies of defective graphene layers were computed for supercells of N primitive cells in a $\sqrt{N} \times \sqrt{N}$ arrangement including a single defect. All the 2D DFT calculations were performed using an out-of-plane artificial periodicity of 30 Bohr. Our bulk silicon calculations used $17 \times 17 \times 17$ Monkhorst–Pack **k**-point grids.

The vibrational contributions to the free energy were calculated using the DFT finite-displacement supercell method. All geometric structures were optimised to minimise the forces on atoms below 0.0005 eV Å^{-1} The phonon calculations were carried out with atomic displacements of 0.005, 0.01, 0.015, 0.02, and 0.025 bohr, and 5×5 Monkhorst–Pack supercell **k**-point grids were used. The final energies were obtained by extrapolating linearly to a zero atomic displacement.

5.2.5.2 QMC orbital generation

The used structures were fixed to the DFT-PBE geometries produced from ultrasoft pseudo-potentials and the fine **k**-point grid. The DFT orbitals were generated using PBE relaxed graphene supercells consisting of 3×3, 4×4 and 5×5 primitive cells with an artificial periodicity of 30 bohr. The plane-wave cutoff energy for the smaller two supercells is 3401 eV, and the plane-wave cutoff energy for the larger supercell is 2231 eV. These cutoff energies are such that the DFT energy per atom converges to within the chemical accuracy limits of 0.1 mHa and 1.59 mHa [60], respectively. Trail-Needs Dirac-Fock pseudopotentials [58, 59] were used to represent the nuclei and core electrons with the s channel being chosen to be the local component when the pseudopotentials are re-represented in Kleinman-Bylander form [61]. For bulk silicon, supercells of $2 \times 2 \times 2$, $3 \times 3 \times 3$ and $4 \times 4 \times 4$ primitive cells were used with a plane-wave cutoff energy of 2231 eV for all system sizes.

5.2.5.3 The SW transition state calculations

All the transition state calculations were performed using the plane-wave-basis code CASTEP [128]. The calculations were performed using the relaxed DFT-PBE geometries generated by ultra-soft pseudo-potentials, a fine **k**-point grid and an artificial periodicity of 30 Bohr. Using the same parameters, the SW transition

state calculations were performed using supercells consisting of $3 \times 3 \times 1$, $5 \times 5 \times 1$ and $6 \times 6 \times 1$ arrangements of primitive cells with a plane-wave cut-off energy of 348.31 eV and fine **k**-point grid. Starting from a fully optimised reactant (pure graphene) and product (SW) structures, we employed the linear synchronous transit maximum method (LST maximum) [252] to locate the initial intermediate image. A more refined saddle point search was performed using an iterative sequence of quadratic synchronous transit maximisations (QST) in conjunction with the conjugate gradient minimisations method [252] until the true transition state was located. Finally, the nudged elastic band technique (NEB) [253] was utilised to validate the transition state and evaluate the energy profile and structural images along the transformation pathway of the SW defect in the graphene sheets.

5.2.6 QMC calculations

5.2.6.1 Trial wave functions

The QMC calculations were performed using the trial wave functions of Slater-Jastrow (SJ) form. Using the TA method, different sets of orbitals were constructed for each twist. The plane-wave orbitals were re-represented on a blip (B-spline) basis [254] to improve the computational efficiency of the QMC calculations and to eliminate the undesirable periodicity in the out-of-plane direction. The Jastrow factor consisted of polynomial electron-electron, electron-nucleus and electron-electron-nucleus terms, in addition to a plane-wave electron-electron term [37]. The trial wave functions were optimised by first minimising the energy variance [47, 48] and subsequently the energy expectation value [52]. For each supercell size, the wave function optimisation was conducted at a single, randomly selected twist, and the resultant optimised Jastrow factor was then used for all twists. The Trail-Needs Dirac-Fock pseudopotentials [58, 59] were used with the d angular momentum channel chosen to be local.

5.2.6.2 DMC calculations

To remove the biases caused by using finite time steps and populations of configurations, the DMC calculations at each twist were performed using time

steps of $\tau = 0.04$ and 0.16 Ha^{-1}, with the corresponding target walker populations being varied inversely to the time step. The target population was at least 256 configurations in all cases. The DMC energies were then extrapolated linearly to a zero time step and infinite population. Concerning the DMC total energies of defective graphene, Fig. 5.1 shows that the usage time steps are not small enough to be in the linear-bias regime. Nevertheless, as shown in Fig. 5.2, the non-linear parts of the time-step bias cancel out in the calculation of the pure defect formation energy at each twist.

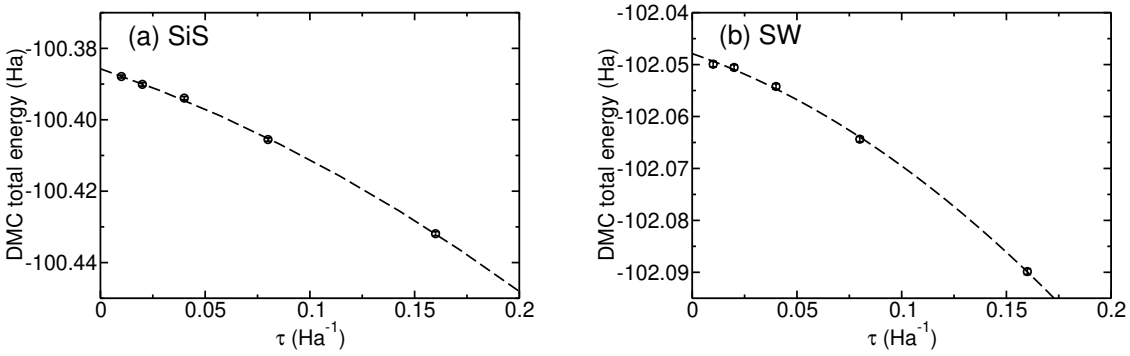

(a) (b)

Figure 5.1: DMC total energies per supercell of (a) SiS, and (b) SW defects in a 3×3 supercell of graphene against the DMC time step τ at a single, randomly chosen twist $\mathbf{k}_s$. The dashed lines show quadratic fits to the energy as a function of the time step.

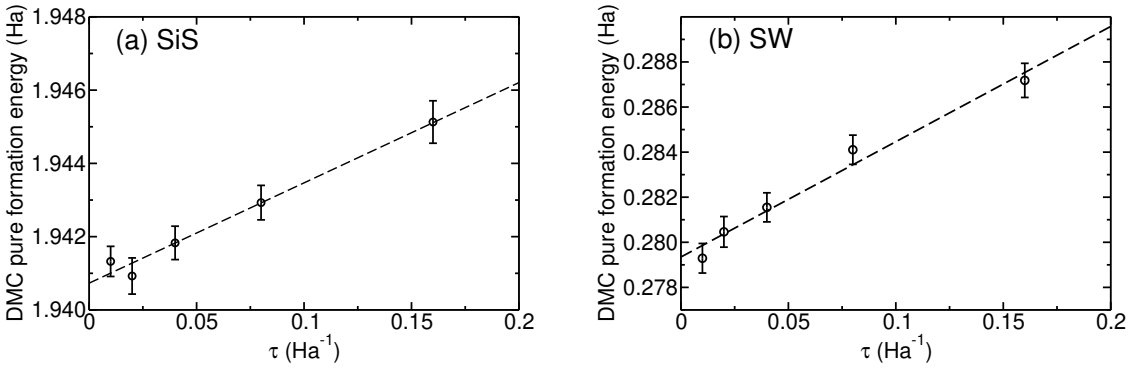

(a) (b)

Figure 5.2: DMC pure formation energies of (a) SiS and (b) SW defects in a 3×3 supercell of graphene against the DMC time step τ at the twist $\mathbf{k}_s$ used in Fig. 5.1. The dashed lines show linear fits to the pure formation energy as a function of the time step.

For bulk silicon calculations, the DMC energies per atom were calculated using the time steps of $\tau = 0.01$, 0.04 and 0.16 Ha^{-1}, enabling linear extrapolation to eliminate the time-step bias in the total energy per atom. Once again, the target walker population was altered inversely with the time step.

5.2.7 Finite-concentration and finite-size effects

5.2.7.1 Periodic supercells

The main source of uncertainty in our defect formation energy results is the need to use finite simulation cells subjected to periodic boundary conditions with a single point defect in the supercell in the DMC calculations. This results in many physical differences from the dilute limit of isolated point defects in a large graphene sheet. In the first place, the modelling of periodic supercells induces finite-size effects at a given defect concentration. These finite-size errors in DMC total energies include quasi-random, oscillatory, single-particle finite-size errors due to momentum quantisation. This issue can be resolved by using the canonical-ensemble TA method [62]. The leading-order long-range finite-size error in the kinetic energy per electron largely cancels out the pure defect formation energies. Second, there are finite-concentration effects resulting from the fact that we are modelling a periodic array of point defects rather than a single defect. The leading-order systematic finite-

concentration error in isolated defect-formation energy arises from unwanted elastic interactions between defects and screened electrostatic interactions between periodic images of defects [255]. Additional non-systematic finite-size errors result from the interactions between charge-density oscillations surrounding defects. Using an appropriate fitting function, we extrapolate the results to an infinite cell size to decrease systematic effects and average out non-systematic effects.

For the calculation of chemical potentials and atomisation energy, the ground-state energies per atom must be determined. In a finite supercell, these calculations suffer from finite-size errors including (i) quasi-random single-particle finite-size errors due to momentum quantisation effects and (ii) systematic finite-size errors due to the evaluation of the long-range interaction between each electron and the surrounding exchange-correlation hole using the Ewald interaction instead of $1/r$ [256], as well as the neglect for long-range two-body correlations [134, 257].

5.2.7.2 Single-particle finite-size effects

In the finite supercell subject to periodic boundary conditions, the replacement of the continuous integral over the first BZ by a sum over a discrete set of **k**-points induces fluctuations in the energy per particle as a function of system size due to single-particle finite-size effects. Similar energy oscillations are often seen in QMC simulations, albeit with a different amplitude. Because momentum quantisation is a single-particle effect, the fluctuations in the QMC energies as a function of twists are generally proportionally 'correlated' to the corresponding fluctuations in the DFT energies. DFT energies can therefore be utilised as a control variate (CV) for calculating the twist-averaged (TA) DMC energy.

The TA energy $E_{\mathrm{DMC}}^{\mathrm{TA}}$ was determined by fitting:

$$E_{\mathrm{DMC}}(\mathbf{k}_{\mathrm{s}}) = E_{\mathrm{DMC}}^{\mathrm{TA}} + b\left[E_{\mathrm{DFT}}(\mathbf{k}_{\mathrm{s}}) - E_{\mathrm{DFT}}^{\mathrm{fine}}\right] \tag{5.8}$$

to the DMC energy $E_{\mathrm{DMC}}(\mathbf{k}_{\mathrm{s}})$ at twist $\mathbf{k}_{\mathrm{s}}$, where b is a fitting parameter, $E_{\mathrm{DFT}}(\mathbf{k}_{\mathrm{s}})$ is the corresponding DFT energy and $E_{\mathrm{DFT}}^{\mathrm{fine}}$ is the DFT energy calculated using a fine **k**-point mesh. The use of DFT energy with the fine **k**-point as a covariate in Eq. (5.8) simultaneously eliminates the noise result from momentum quantisation due to using a finite number of twists and the residual errors in TA energy. Using this approach removes most of the quasirandom noise resulting from momentum

quantisation. The residual long-range errors are many-body effects that cannot be removed by TA method.

All our graphene and bulk silicon DMC calculations were performed using random twists of 24 each. In the calculations of defect formation energy, the total DMC and DFT energies $E(\mathbf{k}_s)$ in Eq. (5.8) were replaced with the DMC and DFT pure defect formation energies $\mathcal{E}^{\mathrm{pf}}(\mathbf{k}_s)$. The calculations of both pure and defective graphene were performed at identical twists; therefore, the twist-sampling error in the pure defect energy is far lower than the error in the total energies. There are two highly different sources of (quasi-)random error in the TA-DMC energy for a given supercell: the statistical error from the Monte Carlo simulation and the residual momentum quantisation error that is not fully removed by fitting Eq. (5.8) to $\mathcal{E}^{\mathrm{pf}}(\mathbf{k}_s)$. By utilising the same set of random twists for both defect and pristine graphene computations, it is more likely that momentum quantisation errors and statistical errors in pure defect formation energy will be significantly cancelled out than in the total energy. In our calculations, we also minimise the mean bias using Eq. (5.8) with all the twists to obtain the TA energy, and we only use twist-blocking method proposed in Ref. [213] to estimate the error bar for the TA formation energy.

5.2.7.3 Long-range finite-size effects

To account for the finite-size effects and long-range finite concentration, the DMC calculations have been performed at different supercell sizes and then the results were extrapolated to an infinite system size using scaling law. In the case of the SiS, there is some charge transfer from the silicon atom to the graphene sheet, giving the defect a dipole moment. Defects in neighbouring supercells lead to the inclusion of unwanted electrostatic dipole–dipole interactions. The screened interaction between charges in a 2D semiconductor is of Rytova-Keldysh form [198, 200], which is logarithmic at a short range, before crossing over to a $1/r$ interaction at a lengthscale typically of the order of many tens of Å. The supercell sizes that we study here are comparable to this length scale. Rytova-Keldysh dipole–dipole interaction energies go as r^{-3} at long range and as r^{-2} at a short range, which leads to finite-concentration errors that go as $O(N^{-1})$ in small supercells, then as $O(N^{-3/2})$ in very large supercells.

The SW defect, on the other hand, is a neutral defect with no dipole moment, as it does not require a charge transfer between atoms. However, these defects have a quadrupole moment, resulting in weak electrostatic interactions between periodic images that decay rapidly as $O(N^{-2}–N^{-5/2})$. Furthermore, elastic finite-concentration effects result from the interaction of periodic images of point defects through the long-range strain and stress field, which depend on the size and shape of the unit cell used [255]. In general, assuming the defects induce isotropic stress, the elastic finite-concentration effects on the energy scale as $O(N^{-1})$.

In summary, the scaling of the elastic finite-size error (and the electrostatic finite-size error in the case of the SiS) suggests that TA pure defect formation energies $\mathcal{E}^{\mathrm{pf}}$ should be extrapolated to the thermodynamic limit by fitting:

$$\mathcal{E}^{\mathrm{pf}}(N) = \mathcal{E}^{\mathrm{pf}}(\infty) + CN^{-1}, \tag{5.9}$$

where C and $\mathcal{E}^{\mathrm{pf}}(\infty)$ are fitting parameters. Using DFT calculations, we confirm in Fig. 5.3 that $O(N^{-1})$ systematic finite-concentration errors are dominant in SW and SiS defects in graphene.

For the bulk silicon results, the energy per atom was extrapolated to an infinite system size by fitting the TA energies per atom $\langle e_{\mathrm{P}}(N)\rangle_{\mathrm{TA}}$ to:

$$\langle e_{\mathrm{P}}(N)\rangle_{\mathrm{TA}} = e_{\mathrm{P}}(\infty) + c\, N^{-\gamma}, \tag{5.10}$$

where $e_{\mathrm{P}}(\infty)$ and c are fitting parameters, and $\gamma = 1$ for bulk silicon [257].

Graphene defect formation energies were computed using Eqs. (5.2)–(5.2) after dealing with the finite-size effects in the pure defect formation energy and chemical potentials separately.

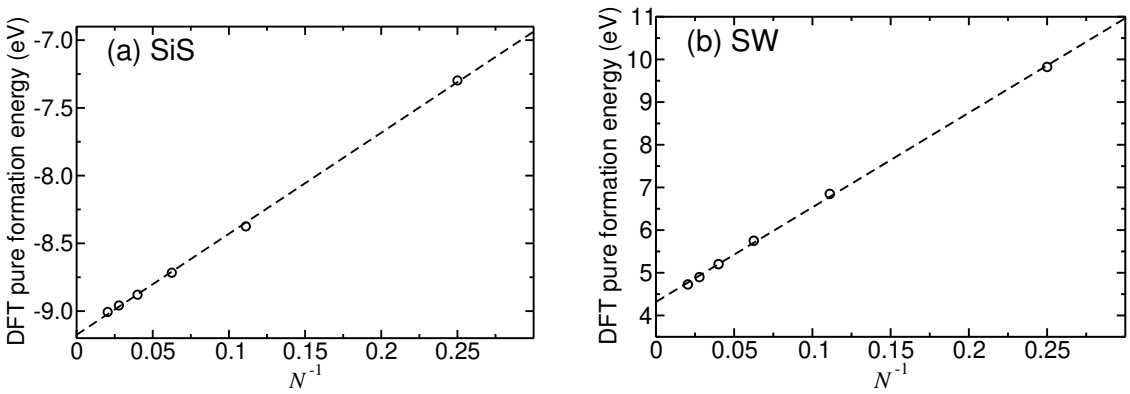

(a) (b)

Figure 5.3: DFT pure formation energies of (a) SiS, and (b) SW defects in graphene against the reciprocal of the supercell size N. Fine **k**-point grids were used in each supercell. Ultrasoft pseudopotentials were used. The dashed lines show fits of Eq. (5.9) to the data.

5.3 Results and discussion

5.3.1 Atomic structures

5.3.1.1 SiS

We used a carbon–carbon bond length of 1.42 Å in all our pristine graphene calculations [250, 251], and we used the exact same supercell lattice parameters for our pristine and defective graphene calculations. Replacing a single carbon atom using a silicon atom results in a defect of C_s point group, rather than D_{3h}, due to a Jahn-Teller distortion [231]. The DFT-PBE-relaxed geometry in Fig. 5.4 shows the silicon atom bonded with three carbon atoms and lying above the graphene plane due to partial sp^3 hybridisation.

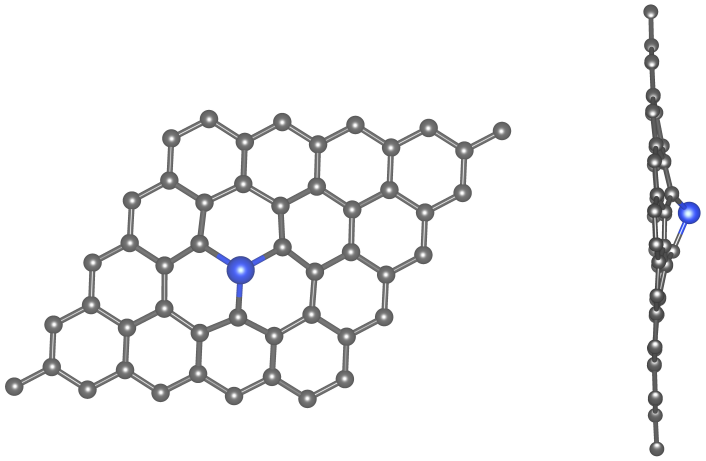

Figure 5.4: (a) Top-down and (b) in-plane views of the DFT-PBE-relaxed SiS structure in a 5×5 supercell. The silicon atom is shown in blue.

5.3.1.2 SW defect

In graphene, an SW defect is formed by an in-plane rotation of a single carbon–carbon bond 90° across its midpoint. This transforms four hexagonal unit cells into two pentagons and two heptagons, as shown in Fig. 5.8, with the same number of carbon atoms as pristine graphene and without any dangling bonds. The SW rotation compresses or stretches many bonds, resulting in a wave of significant vertical displacement of carbon atoms around the defect, as shown in Fig. 5.5. The relaxed lattice will adopt either a 'sine-like' buckled structure, in which the two rotated carbon atoms are slightly displaced in opposite out-of-plane directions, or a 'cosine-like' buckled structure, in which the two rotated carbon atoms are slightly displaced in the same out-of-plane direction. The 'sine-like' structure is the lower-energy configuration [258, 259] and is the structure studied in this work.

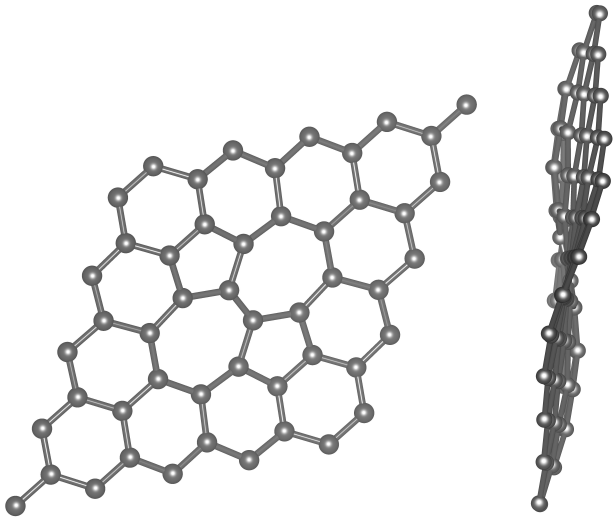

(a) (b)

Figure 5.5: (a) Top-down and (b) in-plane views of the DFT-PBE-relaxed "sine-like" SW defect structure in a 5×5 supercell.

5.3.2 Defect formation energies

Figure 5.6 shows the DMC and DFT defect formation energies as a function of the reciprocal of the system size with different methods to handle the quasirandom finite-size effects. Both the DFT and DMC calculations used Dirac-Fock pseudopotentials. The silicon and carbon chemical potentials were considered the energy per atom of bulk silicon and monolayer graphene, extrapolated to an infinite system size. Therefore, the variation in the results with system size that is shown in this figure only arises from the finite-concentration and finite-size effects in the pure formation energy. The DMC results obtained using the TA method are either performed directly without using a control variate (CV) or by using the DFT results as a CV by fitting to Eq. (5.8). The error bars on the 'TA-DMC with CV' data were obtained using Gaussian propagation of errors through the fit of Eq. (5.8) to the DMC results at all 24 twists. We also employed a twist-blocking technique [213] to get a standard error estimate that accounts for both Monte Carlo random errors and finite-twist-sampling random errors. The 'TB-DMC' data were obtained by grouping the data of 24 twists into six blocks of four twists. Figure 5.6 demonstrates that the use of a CV significantly reduces the random errors in the DMC energy data. However,

the use of a twist-blocking approach to account for the remaining twist-sampling errors does not affect the random error estimate significantly. The DFT results are obtained with a fine **k**-point mesh and the TA-DFT results were calculated in the same fashion as the TA-DMC results without a CV.

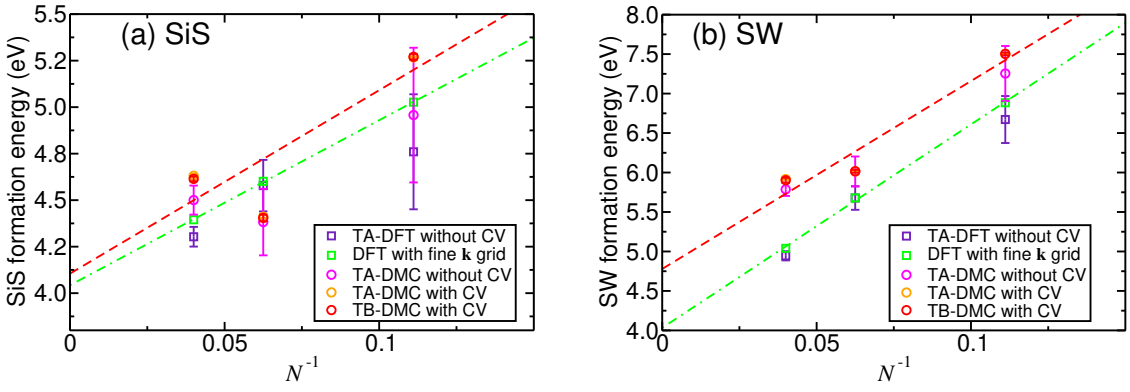

(a) (b)

Figure 5.6: DFT and DMC formation energies against reciprocal of supercell size N, using different methods for dealing with momentum quantisation errors, for (a) SiS, and (b) SW defects. The red dashed lines show an unweighted least-squares fit of Eq. (5.9) to the TB-DMC data.

In theory, the most accurate way to obtain the TA energy is to fit Eq. (5.8) to formation energies in a single block of all the twists and then to use TB to obtain the error bars. We found that the difference between the TA and TB mean energies is negligible in practice; thus, we only used the TB-DMC mean energies for the finite-size extrapolation. However, the TB errors are not large enough to quantify the quasirandom finite-size errors in the formation energies at different supercell sizes. This finite-size noise must thus originate from such effects as the enforced supercell commensurability of Ruderman-Kittel oscillations in the density and pair density rather than momentum quantisation. Quasirandom finite-size effects are larger in the DMC formation energies than in the DFT results, presumably because of the explicit treatment of correlation in QMC methods. Performing DMC calculations on a larger range of supercell sizes and presumably shapes would be straightforward but expensive method to decrease these errors. The error bars on our DMC results were obtained using the unweighted least-squares fit of the TB-DMC energy data.

Our final DFT and DMC defect formation energies are shown in Table 5.1, along

Table 5.1: Theoretical static-nucleus formation energies for various point defects in monolayer graphene. The carbon and silicon chemical potentials are the energies per atom of graphene and bulk silicon, respectively. Results without citations were obtained in the present work. 'NTBM' refers to a nonorthogonal tight-binding model. To compare with experimental results, the vibrational free energies reported in Table 5.3 should be added to the static-nucleus data reported in this table.

Method	Defect formation energy (eV)	
	SiS	SW
DFT-PBE	3.77 [237], 6.85 [260][1], 3.59	4.71 [259], 4.32
DFT-LDA		4.66 [261][2], 4.86 [262], 5.42 [259]
NTBM		4.60 [239]
DMC	4.0(5)	5.82(3) [259] , 5(1)
DMC-corrected DFT	4.4(1)	4.9(1)

[1] Reference [260] uses the ground-state energies of isolated atoms as chemical potentials; for comparison with the other defect formation energies reported in this table, the atomisation energies of graphene and bulk silicon should be, respectively, added to and subtracted from the formation energy of Ref. [260].

[2] This work extrapolates DFT energies at different system sizes in the same fashion we do here. All other cited DFT works are performed at finite supercell size.

with DFT results from the literature. At each system size, we evaluate a correction to the DFT formation energy as a difference between the TB-DMC result and the DFT result with a fine **k**-point grid. The DMC corrections to the defect formation energies in different supercells, including the chemical potentials extrapolated to the thermodynamic limit, are given in Table 5.2. The DMC-corrections to the DFT defect formation energy of the Si-substitution and SW defects were around 0.8(1) eV and 0.5(1) eV, respectively. In general, the difference between the DFT and DMC formation energies is expected to be dominated by short-range effects, with systematic finite-concentration errors (due to electrostatic and elastic effects) similar in DFT and DMC; this is confirmed by the similar gradients of the fitted lines in Fig. 5.6. However, the difference between DFT and DMC shows quasirandom fluctuations as a function of system size, which suggests that the best scheme for using DMC to evaluate defect formation energies is to average the difference between TB-DMC and fine-**k**-point DFT formation energies obtained in multiple supercells and then to apply the resulting correction to DFT results extrapolated to the diluted limit of infinite supercell size. Averaging over multiple supercells is clearly necessary, because the difference between the DMC and DFT results obtained in different cell sizes in Table 5.2 fluctuates randomly by an amount that is significantly larger than the error bars on the individual differences. This is congruent with the finding of Ma *et al.* [259] concerning the SW defect in the graphene sheet.

Table 5.2: DMC corrections to the static-nucleus formation energies for Si substitution and SW defects. Corrections were evaluated as the difference between defect-formation energies calculated with TB-DMC using Eq. (5.8) and DFT-PBE using a fine **k**-point grid. The DFT calculations use ultra-soft pseudopotentials rather than the Trail-Needs Dirac-Fock pseudopotentials used by the QMC calculations.

Supercell	DMC correction to formation energy (eV)	
	SiS	SW
3×3	1.07(9)	0.65(2)
4×4	0.54(9)	0.27(2)
5×5	0.91(9)	0.70(3)
Mean	0.8(1)	0.5(1)

The DMC literature result for the SW formation energy [259], which has a comparatively tiny standard error, was only calculated in a 5×5 supercell with no attempt to control finite-size effects; our standard error is larger because it accounts for quasirandom finite-size effects. DFT-PBE significantly underestimates the formation energy for both defects. The DFT-PBE differences in the zero-point vibrational energies and Helmholtz free energies at 298 K between defective and pristine graphene for the SiS and SW defects are shown in Table 5.3. These vibrational free-energy contributions should be added to the static-nucleus defect-formation energies in Table 5.1. The vibrationally corrected DMC defect-formation energies are 3.6(1) and 4.4(1) at 298 K for SiS and SW defects, respectively.

Table 5.3: DFT-PBE vibrational contributions to the Helmholtz free energies of the formation of various point defects in monolayer graphene. The contributions are extrapolated to the dilute limit.

Temperature (K)	Vib. contrib. to form. energy (eV)	
	SiS	SW
0	−0.44	−0.49
298	−0.41	−0.47

5.3.3 SW transition state

Our PBE-DFT calculations predict that the true transition state corresponds to the intermediate geometry, with two carbon atoms being displaced out of the plane in different directions and two broken carbon bonds, as shown in Fig. 5.8c. The NEB method has been used to generate a set of images between the reactant and product structures of the system and then to optimise them to the minimum energy pathway. The energy diagram in Fig. 5.7 illustrates the calculated energy barrier as a function of the bond rotation from 0 to 90. The PBE-DFT values for the formation and activation energies of the SW transformation are illustrated in Table 5.4. The high-barrier energy is a result of the extensive atomic rearrangements, including the breakage of two carbon bonds in the transition state. The high activation energy for the SW transition state indicates that the formed SW defect will remain stable under normal conditions and it is unlikely, even at high temperatures, to restore the graphene structure to its pristine state after the SW defect has formed [247].

Table 5.4: The PBE-DFT activation barrier energy E_a and defect formation energy for SW defects in graphene monolayer sheet E_{SW}. The DFT results in [6] were obtained using the DFT-PW91 functional.

Supercell	E_a (eV)	E_{SW} (eV)
3×3	9.68	6.84
5×5	9.2[6], 9.44	4.8[6], 5.2
6×6	9.394	4.898

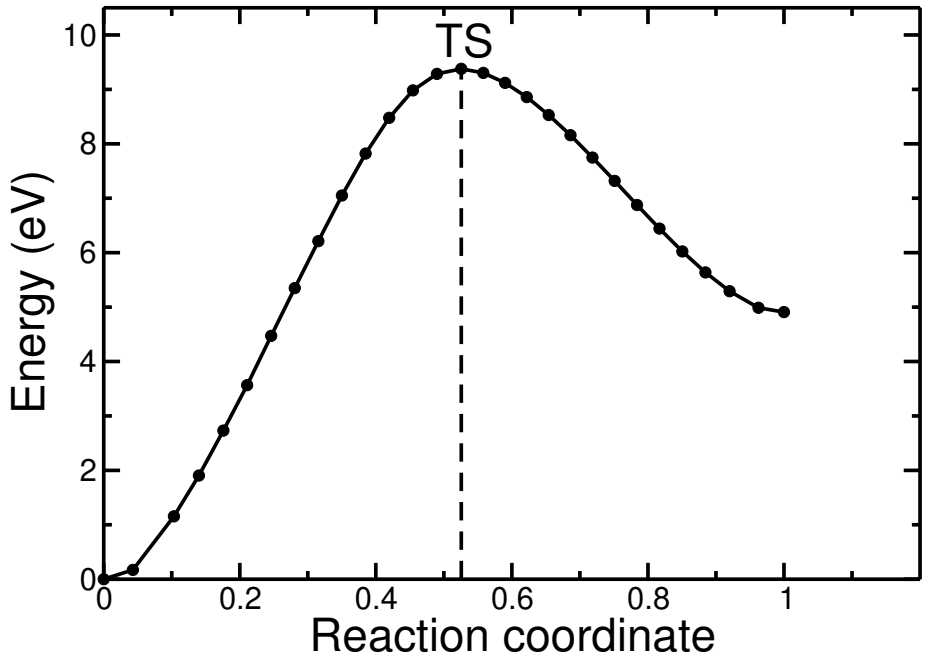

Figure 5.7: The energy barrier of the SW defect formation for a $6 \times 6 \times 1$ supercell as a function of reaction coordinates.

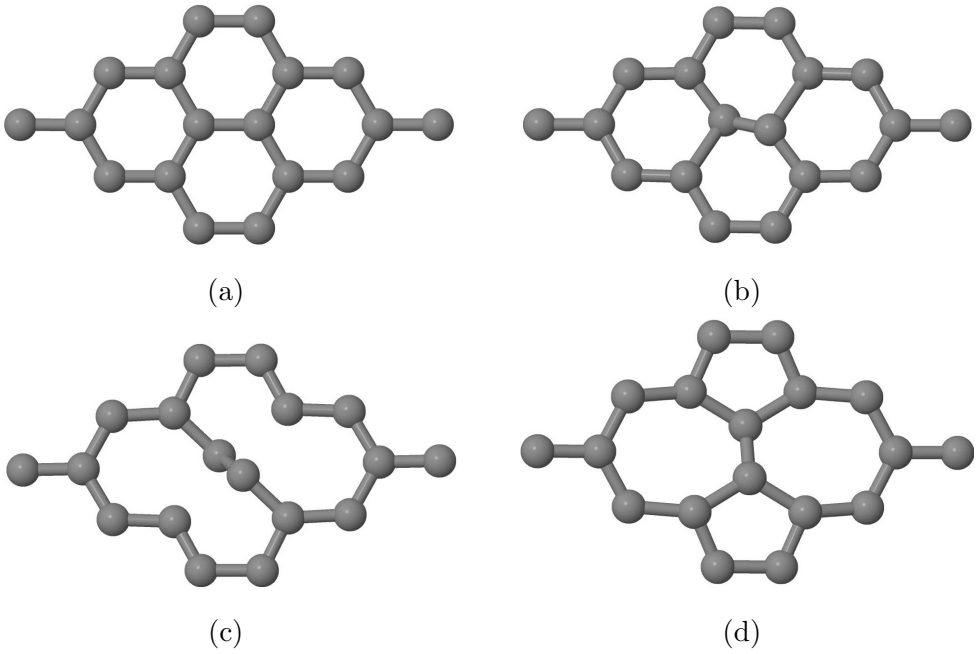

Figure 5.8: The Stone–Wales transformation: (a)-(d) show the intermediate images for the corresponding reaction coordinates at different rotation angles of the central bond from 0° to 90° with respect to the loading direction. (c) The atomic configurations of the SW transition state.

5.3.4 Bulk silicon atomisation energies

For bulk silicon, we used DFT-PBE lattice parameters of 5.469 Å. DMC atomisation energies are plotted against system size in Fig. 5.9 for bulk silicon, showing that finite-size effects are largely removed by extrapolation. The DFT-PBE vibrational Helmholtz free energies per atom at 0 K and 298 K were found to be 61.9 meV/atom and 36.1 meV/atom for silicon bulk, respectively. We also take this opportunity to compare the bulk diamond-structure silicon results to the silicene, the 2D allotrope of silicon. Silicene, the silicon counterpart of graphene, is a honeycomb structure of silicon atoms with slightly buckled hexagonal sublattices that result from mixing sp^2 and sp^3 hybridization. The dynamical stability of free-standing silicene has been demonstrated theoretically using DFT calculations [263, 264]; however, in practice it can only be synthesized experimentally on metal surfaces [265–267]. The fundamental issue for any attempt to use silicene in practical devices is its lack of thermodynamic stability. Our vibration results indicate that the vibrational effects stabilise silicene [213] more than bulk diamond-structure silicon at room temperature.

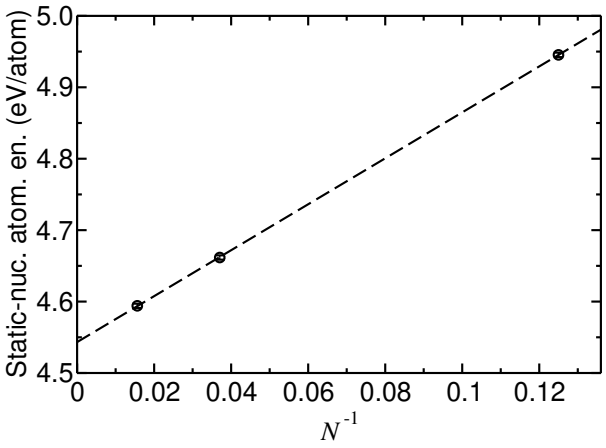

Figure 5.9: TA-DMC static-nucleus atomisation energies of bulk silicon against N^{-1}, where N is the number of primitive cells in the supercell. The atomisation energies are defined with respect to the DMC spin-polarised $^3P_0$ ground states of an isolated silicon atom.

The vibrational corrected DMC atomisation energies for bulk silicon extrapolated to infinite system size, are reported in Table 5.5, along with DFT results. We found the vibrationally corrected SJ-DMC atomisation energy to be 4.4815(6) eV and

4.5073(6) at 0K and 298 K, respectively. We evaluated our DFT and DMC results considering the results reported in the previous literature [268–271]. Both LDA-DFT and PBE-DFT calculations significantly overestimated the atomisation energy of bulk silicon in DFT compared with DMC. Compared to the earlier DMC works [268, 270], there is a small but statistically significant difference from our DMC result. This disagreement probably arises from the fact that the earlier works did not use TA. The DMC and DFT-PBE results are in reasonable agreement with the experimentally determined atomisation energy of bulk silicon. In comparison with the silicene's DMC atomization energies results, bulk silicon is energetically more stable than silicene by a huge margin of 0.7522(5) eV/atom [213]. This quantifies the significant thermodynamic challenge involved in producing free-standing silicene.

Table 5.5: Helmholtz free energies of THE atomisation of bulk silicon. The DFT-PBE vibrational free-energies reported in Sec. 5.3.4 have been subtracted from our static-nucleus atomisation energies. Results without citations were obtained in the present work.

Method	Atomisation energies (eV/atom) Bulk silicon	
Temperature	0 K	298 K
DFT-LDA	5.34 [268], 5.3 [269], 5.29	5.31
DFT-PW91	4.653 [268]	
DFT-PBE	4.55	4.58
GFMC	4.51(3) [269][1]	
DMC	4.62(1) [268], 4.63(2) [270], 4.4815(6)	4.5073(6)
Experiment	4.62(8) [271, 272]	

[1] Green's function Monte Carlo method.

5.4 Conclusion

In summary, we used the DMC method to investigate the accuracy of DFT in first-principles studies of point defect formations in monolayer graphene. The DMC and DFT calculations of defected graphene were performed for different simulation

cells. We found that DFT and QMC defect formation energies are affected by both systematic and quasirandom finite-concentration effects. Although the systematic finite-concentration effects in both QMC and DFT are similar, (so such that they can be eliminated by extrapolation using an appropriate scaling law), the residual quasi-random errors in our DMC formation energy are significant. These errors can be reduced by taking the difference between the TA QMC and DFT formation energy over different cell sizes, then applying that as a correction to DFT formation energies extrapolated to infinite system size.

Our results suggest that DFT-PBE underestimates the formation energies of isolated silicon substitutions and Stone–Wales defects by a significant margin of order 1 eV. Vibrational contributions to the free energies of the formation of point defects in graphene have also been found to be non-negligible. Thus, there are many factors to balance when evaluating defect formation energies in 2D materials from first principles. We have also investigated the SW defects' transition state and the associated activation barrier energy at different system sizes. We found that the energy barrier of SW transformation is as high as 9.3 eV due to the atomic rearrangement caused by the 90° rotation of a single carbon–carbon bond. We also calculated the DMC atomisation energies of bulk silicon to be in good agreement with experimental results. Our results indicate that the DFT-PBE calculations significantly overestimate the bulk silicon atomisation energy. We have also compared the QMC atomization energies of bulk silicon and monolayer silicene, finding that bulk silicon is more stable than silicene by 0.7522(5) eV per atom.

Chapter 6

Conclusions

QMC methods are accurate many-body approaches that can be applied to a wide range of extended condensed materials or molecules. In this thesis, we have studied the electronic, vibrational and optical properties of several materials using QMC methods. In Chapter 1, we briefly reviewed the electronic structure methods most commonly used in continuum condensed matter physics problems–namely, Hartree-Fock theory, density functional theory and variational and diffusion quantum Monte Carlo.

In Chapter 2, we developed a new methodology that accounts for the vibrational effects on electronic structure based on the random sampling of the vibrational normal coordinates from the nuclear wave functions within the BO approximation. We started with a brief summary of the current developments in this area and then outlined the vibrational renormalisation theory. We assumed that the atoms in a crystalline solid can be considered frozen but randomly displaced from their equilibrium lattice positions due to the quantum and thermal effects of lattice vibration, resulting in a distribution of electronic excitation energies with a mean value that differs from the static-nucleus gap. On the timescale of nuclear motion, electronic transitions are instantaneous; therefore, the vibrational renormalisations of optical gaps are obtained by averaging gap energies over a set of randomly sampled atomic configurations. The formal description of the proposed technique was then discussed in detail. We presented an efficient method to unfold the electronic band structure of crystalline systems with negligible computational expense, considering the electronic states' degeneracy.

In Chapter 3, we explored the application of our developed random sampling method and employed the unfolding algorithm for electronic band structures. Atomic configurations were randomly sampled based on quasiharmonic phonon calculations within density functional theory, and the excitation energy at each configuration was evaluated using QMC. The zero-point renormalisation and temperature dependent effects were calculated for a range of materials. Our presented method is based on supercell computations, which can be computationally expensive for a larger system size. Nevertheless, the number of needed atomic configurations sampled to reach convergence within QMC calculations is significantly reduced to a small number (24) of random configurations by using the DFT renormalised gaps as a control variate to reduce the statistical error bar of QMC gaps. Our results show that averaging the band gap over atomic configurations reduces statistical error bars, and the additional cost of vibrationally averaging QMC calculations is relatively small. The vibrational renormalisation of the benzene band gap shows a noticeable dependency on the DFT functionals used to produce the harmonic vibrational phonons and generate the geometry and the orbitals for the QMC calculations. The energy difference between the PBE and LDA functionals renormalised gaps was approximately $-0.119(5)$ eV, introducing a further source of error into our QMC gap calculations. The implementation of a superior wave function with a backflow function and multideterminant expansions in the benzene calculations substantially improved the agreement with the experimental results.

In the calculations of bulk Si and C-diamond renormalised band gaps, the phonon frequencies and bond lengths of semiconductors have been stated to be accurately described by the LDA-DFT functional [16]. Using the LDA structure and phonon frequencies, we reported the static-nucleus and vibrationally renormalised direct gaps of bulk Si and C-diamond. The SJ-DMC renormalised gap calculations of C-diamond gave the largest vibrational correction in our presented calculations by around $-1.0(1)$ eV, which indicates strong electron-phonon coupling effects. On the other hand, the SJ-DMC renormalisation calculations of bulk Si direct gap show small but not trivial vibrational corrections, which indicate the weak effect of electron-phonon coupling on the band gap. The vibrational correction of the direct optical gap of monolayer hBN was about $-0.60(4)$ eV, whereas the indirect optical

gap correction exhibited a small reduction. We also investigated the quantum effect of zero-point motion on optical gaps of the vdW system of bulk hBN. We calculated the quantum effect of zero-point motion on the optical gaps of bulk hBN. It is clear that the SJ-DMC renormalisation corrections for the bulk hBN band gaps are not negligible for the size of the studied system. In all our gap calculations, the DFT method significantly underestimated the band-gap energy.

In Chapter 4, we performed QMC calculations to simulate finite concentrations of charge carriers interacting through the Keldysh interaction in 2D materials. At the low density limit, the electron-hole relaxation energy, PCF and contact PCF were calculated. The calculated relaxation energy showed some consistency with earlier work using Coulomb interactions. For a range of density parameter r_s values larger than the size of an isolated trion, the results indicated the formation of the negative trion. Our results also showed that the electron-hole relaxation energy approached the isolated negative trion energy at extreme low densities. The findings of pair correlation functions, particularly the electron-hole contact PCF, will be of advantage in calculating the electron-hole recombination rate.

Finally, in Chapter 5, we considered the properties of point defect formations in monolayer graphene–namely, the silicon substitutions and Stone-Wales defects–to benchmark the accuracy of the widely used DFT method in the study of point defects in graphene sheet. The defect formation results showed that the residual quasi-random finite-size errors in our DMC formation energy were significant. Therefore, we suggested that the best way to calculate the defect formation energies is to use the difference between the TA QMC and DFT formation energy as a correction to DFT formation energies extrapolated to infinite system size. Our results showed that DFT-PBE underestimates the defect formation energies of isolated silicon substitutions and Stone-Wales defects by a significant margin (1 eV). Moreover, the PBE-DFT activation energy for the SW transformation was as high as 9.3 eV, in good agreement with earlier work. The DMC atomisation energy of bulk silicon was also estimated and found to be in excellent agreement with the experimental data.

Bibliography

[1] P. Lautenschlager, M. Garriga, L. Vina, and M. Cardona, "Temperature dependence of the dielectric function and interband critical points in silicon," *Phys. Rev. B*, vol. 36, pp. 4821–4830, Sep 1987.

[2] S. Logothetidis, J. Petalas, H. M. Polatoglou, and D. Fuchs, "Origin and temperature dependence of the first direct gap of diamond," *Phys. Rev. B*, vol. 46, pp. 4483–4494, Aug 1992.

[3] G. G. Spink, P. López Ríos, N. D. Drummond, and R. J. Needs, "Trion formation in a two-dimensional hole-doped electron gas," *Phys. Rev. B*, vol. 94, p. 041410, Jul 2016.

[4] R. J. Hunt, "Ab initio modelling of two-dimensional semiconductors," 2019.

[5] L. Viña, S. Logothetidis, and M. Cardona, "Temperature dependence of the dielectric function of germanium," *Phys. Rev. B*, vol. 30, pp. 1979–1991, Aug 1984.

[6] L. Li, S. Reich, and J. Robertson, "Defect energies of graphite: Density-functional calculations," *Phys. Rev. B*, vol. 72, p. 184109, Nov 2005.

[7] M. Born and J. R. Oppenheimer, "On the quantum theory of molecules," *Ann. Physik*, vol. 87, no. 457, 1927.

[8] N. W. Ashcroft, *Solid state physics*. New York : South Melbourne ; London: Holt, Rinehart and Winston, Brooks/Cole, Thomson Learning, 1976.

[9] A. Szabo and N. Ostlund, *Modern Quantum Chemistry: Introduction to Advanced Electronic Structure Theory*. Dover Books on Chemistry, Dover Publications, 2012.

[10] J. Kohanoff, *Electronic structure calculations for solids and molecules : theory and computational methods*. Cambridge: Cambridge University Press, 2006.

[11] J. A. Pople, "Nobel lecture: Quantum chemical models," *Rev. Mod. Phys.*, vol. 71, pp. 1267–1274, Oct 1999.

[12] R. G. Parr and Y. Weitao, *Density-Functional Theory of Atoms and Molecules*. International Series of Monographs on Chemistry, New York: Oxford University Press, Incorporated, 1989.

[13] R. M. Martin, *Electronic structure : basic theory and practical methods*. Cambridge: Cambridge University Press, 2004.

[14] P. Hohenberg and W. Kohn, "Inhomogeneous electron gas," *Phys. Rev.*, vol. 136, pp. B864–B871, Nov 1964.

[15] W. Kohn and L. J. Sham, "Self-consistent equations including exchange and correlation effects," *Phys. Rev.*, vol. 140, pp. A1133–A1138, Nov 1965.

[16] S. Baroni, S. De Gironcoli, A. Dal Corso, and P. Giannozzi, "Phonons and related crystal properties from density-functional perturbation theory," *Rev. Mod. Phys.*, vol. 73, no. 2, p. 515, 2001.

[17] J. P. Perdew, K. Burke, and M. Ernzerhof, "Generalized gradient approximation made simple," *Phys. Rev. Lett.*, vol. 77, pp. 3865–3868, Oct 1996.

[18] A. D. Becke, "Density-functional thermochemistry. III. the role of exact exchange," *J. Chem. Phys.*, vol. 98, no. 7, pp. 5648–5652, 1993.

[19] C. Lee, W. Yang, and R. G. Parr, "Development of the Colle-Salvetti correlation-energy formula into a functional of the electron density," *Phys. Rev. B*, vol. 37, pp. 785–789, Jan 1988.

[20] F. O. Kannemann and A. D. Becke, "van der Waals interactions in density-functional theory: Intermolecular complexes," *J. Chem. Theory Comput.*, vol. 6, no. 4, pp. 1081–1088, 2010.

[21] S. Grimm2011e, "Density functional theory with London dispersion corrections," *Comput. Mol. Sci.*, vol. 1, no. 2, pp. 211–228, 2011.

[22] A. Tkatchenko and M. Scheffler, "Accurate molecular van der Waals interactions from Ground-State Electron density and free-atom reference data," *Phys. Rev. Lett.*, vol. 102, p. 073005, Feb 2009.

[23] A. Tkatchenko, R. A. DiStasio, R. Car, and M. Scheffler, "Accurate and efficient method for many-body van der Waals interactions," *Phys. Rev. Lett.*, vol. 108, p. 236402, Jun 2012.

[24] W. M. C. Foulkes, L. Mitas, R. J. Needs, and G. Rajagopal, "Quantum Monte Carlo simulations of solids," *Rev. Mod. Phys.*, vol. 73, pp. 33–83, Jan 2001.

[25] R. J. Needs, M. D. Towler, N. D. Drummond, P. López Ríos, and J. R. Trail, "Variational and diffusion quantum Monte Carlo calculations with the CASINO code," *J. Chem. Phys.*, vol. 152, no. 15, p. 154106, 2020.

[26] G. Rajagopal, R. J. Needs, A. James, S. D. Kenny, and W. M. C. Foulkes, "Variational and diffusion quantum Monte Carlo calculations at nonzero wave vectors: Theory and application to diamond-structure germanium," *Phys. Rev. B*, vol. 51, pp. 10591–10600, Apr 1995.

[27] N. Metropolis, A. W. Rosenbluth, M. N. Rosenbluth, A. H. Teller, and E. Teller, "Equation of state calculations by fast computing machines," *J. Chem. Phys.*, vol. 21, no. 6, pp. 1087–1092, 1953.

[28] W. K. Hastings, "Monte Carlo sampling methods using Markov chains and their applications," *Biometrika*, vol. 57, pp. 97–109, 04 1970.

[29] R. J. Needs, M. D. Towler, N. D. Drummond, and P. López Ríos, "Continuum variational and diffusion quantum Monte Carlo calculations," *J. Condens. Matter Phys.*, vol. 22, p. 023201, Dec 2009.

[30] J. B. Anderson, "Quantum chemistry by random walk," *J. Chem. Phys.*, vol. 65, no. 10, pp. 4121–4127, 1976.

[31] G. Ortiz, D. M. Ceperley, and R. M. Martin, "New stochastic method for systems with broken time-reversal symmetry: 2D fermions in a magnetic field," *Phys. Rev. Lett.*, vol. 71, pp. 2777–2780, Oct 1993.

[32] B. Hammond, *Monte Carlo methods in ab initio quantum chemistry*. World Scientific lecture and course notes in chemistry ; vol. 1, Singapore ; River Edge, NJ: World Scientific, 1994.

[33] W. M. C. Foulkes, R. Q. Hood, and R. J. Needs, "Symmetry constraints and variational principles in diffusion quantum Monte Carlo calculations of excited-state energies," *Phys. Rev. B*, vol. 60, pp. 4558–4570, Aug 1999.

[34] M. Suzuki, "Generalized Trotter's formula and systematic approximants of exponential operators and inner derivations with applications to many-body problems," *Commun. Math. Phys.*, vol. 51, no. 2, pp. 183–190, 1976.

[35] R. M. Lee, G. J. Conduit, N. Nemec, P. López Ríos, and N. D. Drummond, "Erratum: Strategies for improving the efficiency of quantum Monte Carlo calculations," *Phys. Rev. E*, vol. 85, p. 029908, Feb 2012.

[36] D. M. Ceperley and M. H. Kalos, *Quantum Many-Body Problems*, pp. 145–194. Berlin, Heidelberg: Springer Berlin Heidelberg, 1986.

[37] N. D. Drummond, M. D. Towler, and R. J. Needs, "Jastrow correlation factor for atoms, molecules, and solids," *Phys. Rev. B*, vol. 70, p. 235119, Dec 2004.

[38] R. Needs, M. Towler, N. Drummond, and P. L. Rıos, "User's guide version 2.13 (2022)," 2019.

[39] T. Kato, "On the eigenfunctions of many-particle systems in quantum mechanics," *Commun. Pure Appl. Math.*, vol. 10, no. 2, pp. 151–177, 1957.

[40] M. Casula and S. Sorella, "Geminal wave functions with Jastrow correlation: A first application to atoms," *J. Chem. Phys.*, vol. 119, no. 13, pp. 6500–6511, 2003.

[41] M. Bajdich, L. Mitas, L. K. Wagner, and K. E. Schmidt, "Pfaffian pairing and backflow wavefunctions for electronic structure quantum Monte Carlo methods," *Phys. Rev. B*, vol. 77, p. 115112, Mar 2008.

[42] C. Filippi and C. J. Umrigar, "Multiconfiguration wave functions for quantum Monte Carlo calculations of first-row diatomic molecules," *J. Chem. Phys.*, vol. 105, no. 1, pp. 213–226, 1996.

[43] R. P. Feynman and M. Cohen, "Energy spectrum of the excitations in liquid helium," *Phys. Rev.*, vol. 102, pp. 1189–1204, Jun 1956.

[44] Y. Kwon, D. M. Ceperley, and R. M. Martin, "Effects of three-body and backflow correlations in the two-dimensional electron gas," *Phys. Rev. B*, vol. 48, pp. 12037–12046, Oct 1993.

[45] Y. Kwon, D. M. Ceperley, and R. M. Martin, "Effects of backflow correlation in the three-dimensional electron gas: Quantum Monte Carlo study," *Phys. Rev. B*, vol. 58, pp. 6800–6806, Sep 1998.

[46] P. López Ríos, A. Ma, N. D. Drummond, M. D. Towler, and R. J. Needs, "Inhomogeneous backflow transformations in quantum Monte Carlo calculations," *Phys. Rev. E*, vol. 74, p. 066701, December 2006.

[47] C. J. Umrigar, K. G. Wilson, and J. W. Wilkins, "Optimized trial wave functions for quantum Monte Carlo calculations," *Phys. Rev. Lett.*, vol. 60, pp. 1719–1722, April 1988.

[48] N. D. Drummond and R. J. Needs, "Variance-minimization scheme for optimizing Jastrow factors," *Phys. Rev. B*, vol. 72, p. 085124, Aug 2005.

[49] D. Bressanini, G. Morosi, and M. Mella, "Robust wave function optimization procedures in quantum Monte Carlo methods," *J. Chem. Phys.*, vol. 116, no. 13, pp. 5345–5350, 2002.

[50] M. P. Nightingale and V. Melik-Alaverdian, "Optimization of ground- and excited-state wave functions and van der Waals clusters," *Phys. Rev. Lett.*, vol. 87, p. 043401, Jul 2001.

[51] J. Toulouse and C. J. Umrigar, "Optimization of quantum Monte Carlo wave functions by energy minimization," *J. Chem. Phys.*, vol. 126, no. 8, p. 084102, 2007.

[52] C. J. Umrigar, J. Toulouse, C. Filippi, S. Sorella, and R. G. Hennig, "Alleviation of the fermion-sign problem by optimization of many-body wave functions," *Phys. Rev. Lett.*, vol. 98, p. 110201, Mar 2007.

[53] D. M. Ceperley, "The statistical error of Green's function Monte Carlo," *J. Stat. Phys.*, vol. 43, no. 5, pp. 815–826, 1986.

[54] H. Flyvbjerg and H. G. Petersen, "Error estimates on averages of correlated data," *J. Chem. Phys.*, vol. 91, no. 1, pp. 461–466, 1989.

[55] B. L. Hammond, P. J. Reynolds, and W. A. Lester, "Valence quantum Monte Carlo with ab initio effective core potentials," *J. Chem. Phys.*, vol. 87, no. 2, pp. 1130–1136, 1987.

[56] A. Ma, N. D. Drummond, M. D. Towler, and R. J. Needs, "All-electron quantum Monte Carlo calculations for the noble gas atoms He to Xe," *Phys. Rev. E*, vol. 71, p. 066704, Jun 2005.

[57] M. Casula, S. Moroni, S. Sorella, and C. Filippi, "Size-consistent variational approaches to nonlocal pseudopotentials: Standard and lattice regularized diffusion Monte Carlo methods revisited," *J. Chem. Phys.*, vol. 132, no. 15, p. 154113, 2010.

[58] J. R. Trail and R. J. Needs, "Norm-conserving Hartree-Fock pseudopotentials and their asymptotic behavior," *J. Chem. Phys.*, vol. 122, no. 1, p. 014112, 2005.

[59] J. R. Trail and R. J. Needs, "Smooth relativistic Hartree-Fock pseudopotentials for H to Ba and Lu to Hg," *J. Chem. Phys.*, vol. 122, no. 17, p. 174109, 2005.

[60] N. D. Drummond, J. R. Trail, and R. J. Needs, "Trail-Needs pseudopotentials in quantum Monte Carlo calculations with plane-wave/blip basis sets," *Phys. Rev. B*, vol. 94, p. 165170, October 2016.

[61] L. Kleinman and D. M. Bylander, "Efficacious form for model pseudopotentials," *Phys. Rev. Lett.*, vol. 48, pp. 1425–1428, May 1982.

[62] C. Lin, F. H. Zong, and D. M. Ceperley, "Twist-averaged boundary conditions in continuum quantum Monte Carlo algorithms," *Phys. Rev. E*, vol. 64, no. 1, p. 016702, 2001.

[63] J. Heyd, G. E. Scuseria, and M. Ernzerhof, "Hybrid functionals based on a screened Coulomb potential.," *J. Chem. Phys.*, vol. 118, no. 18, p. 8207, 2003.

[64] J. Muscat, A. Wander, and N. M. Harrison, "On the prediction of band gaps from hybrid functional theory," *Chem. Phys. Lett*, vol. 342, no. 3-4, pp. 397–401, 2001.

[65] L. Hedin, "New method for calculating the one-particle Green's function with application to the electron-gas problem," *Phys. Rev.*, vol. 139, pp. A796–A823, Aug 1965.

[66] F. Aryasetiawan and O. Gunnarsson, "The GW method," *Rep. Prog. Phys.*, vol. 61, pp. 237–312, Mar 1998.

[67] M. S. Hybertsen and S. G. Louie, "Electron correlation in semiconductors and insulators: Band gaps and quasiparticle energies," *Phys. Rev. B*, vol. 34, pp. 5390–5413, Oct 1986.

[68] G. Onida, L. Reining, and A. Rubio, "Electronic excitations: density-functional versus many-body Green's-function approaches," *Rev. Mod. Phys.*, vol. 74, pp. 601–659, Jun 2002.

[69] A. Grüneis, M. Marsman, and G. Kresse, "Second-order Møller-Plesset perturbation theory applied to extended systems. II. structural and energetic properties," *J. Chem. Phys.*, vol. 133, no. 7, p. 074107, 2010.

[70] A. Dittmer, R. Izsák, F. Neese, and D. Maganas, "Accurate band gap predictions of semiconductors in the framework of the similarity transformed equation of motion coupled cluster theory," *Inorg. Chem.*, vol. 58, pp. 9303–9315, Jul 2019.

[71] J. Kolorenč and L. Mitas, "Applications of quantum Monte Carlo methods in condensed systems," *Rep. Prog. Phys.*, vol. 74, p. 026502, Jan 2011.

[72] R. M. Grimes, B. L. Hammond, P. J. Reynolds, and W. A. Lester Jr, "Quantum Monte Carlo approach to electronically excited molecules," *J. Chem. Phys.*, vol. 85, no. 8, pp. 4749–4750, 1986.

[73] P. J. Reynolds, R. N. Barnett, B. L. Hammond, R. M. Grimes, and W. A. Lester, "Quantum chemistry by quantum Monte Carlo: Beyond ground-state energy calculations," *Int. J. Quantum Chem.*, vol. 29, no. 4, pp. 589–596, 1986.

[74] L. Mitáš and R. M. Martin, "Quantum Monte Carlo of nitrogen: atom, dimer, atomic, and molecular solids," *Phys. Rev. Lett.*, vol. 72, no. 15, p. 2438, 1994.

[75] R. J. Hunt, M. Szyniszewski, G. I. Prayogo, R. Maezono, and N. D. Drummond, "Quantum Monte Carlo calculations of energy gaps from first principles," *Phys. Rev. B*, vol. 98, p. 075122, Aug 2018.

[76] P. B. Allen and V. Heine, "Theory of the temperature dependence of electronic band structures," *J. Phys. C*, vol. 9, pp. 2305–2312, Jun 1976.

[77] P. B. Allen and M. Cardona, "Theory of the temperature dependence of the direct gap of germanium," *Phys. Rev. B*, vol. 23, pp. 1495–1505, Feb 1981.

[78] S. Poncé, G. Antonius, P. Boulanger, E. Cannuccia, A. Marini, M. Cote, and X. Gonze, "Verification of first-principles codes: Comparison of total energies, phonon frequencies, electron–phonon coupling and zero-point motion correction to the gap between ABINIT and QE/Yambo," *Comput. Mater. Sci.*, vol. 83, pp. 341–348, 2014.

[79] F. Giustino, S. G. Louie, and M. L. Cohen, "Electron–phonon renormalization of the direct band gap of diamond," *Phys. Rev. Lett.*, vol. 105, p. 265501, Dec 2010.

[80] E. Cannuccia and A. Marini, "Effect of the quantum zero-point atomic motion on the optical and electronic properties of diamond and trans-polyacetylene," *Phys. Rev. Lett.*, vol. 107, p. 255501, Dec 2011.

[81] G. Antonius, S. Poncé, P. Boulanger, M. Côté, and X. Gonze, "Many-body effects on the zero-point renormalization of the band structure," *Phys. Rev. Lett.*, vol. 112, p. 215501, May 2014.

[82] A. Marini, "Ab initio finite-temperature excitons," *Phys. Rev. Lett.*, vol. 101, p. 106405, Sep 2008.

[83] S. Poncé, G. Antonius, Y. Gillet, P. Boulanger, J. Laflamme Janssen, A. Marini, M. Côté, and X. Gonze, "Temperature dependence of electronic eigenenergies in the adiabatic harmonic approximation," *Phys. Rev. B*, vol. 90, p. 214304, Dec 2014.

[84] G. Antonius, S. Poncé, E. Lantagne-Hurtubise, G. Auclair, X. Gonze, and M. Côté, "Dynamical and anharmonic effects on the electron–phonon coupling and the zero-point renormalization of the electronic structure," *Phys. Rev. B*, vol. 92, p. 085137, Aug 2015.

[85] R. B. Capaz, C. D. Spataru, P. Tangney, M. L. Cohen, and S. G. Louie, "Temperature dependence of the band gap of semiconducting carbon nanotubes," *Phys. Rev. Lett.*, vol. 94, p. 036801, Jan 2005.

[86] B. Monserrat and R. J. Needs, "Comparing electron–phonon coupling strength in diamond, silicon, and silicon carbide: First-principles study," *Phys. Rev. B*, vol. 89, p. 214304, Jun 2014.

[87] C. E. Patrick, K. W. Jacobsen, and K. S. Thygesen, "Anharmonic stabilization and band gap renormalization in the perovskite $CsSnI_3$," *Phys. Rev. B*, vol. 92, p. 201205, Nov 2015.

[88] P. García-Risueño, P. Han, and G. Bester, "Frozen-phonon method for state anticrossing situations and its application to zero-point motion effects in diamondoids," *arXiv:1904.05385*, 2019.

[89] D. M. Ceperley, "Path integrals in the theory of condensed helium," *Rev. Mod. Phys.*, vol. 67, pp. 279–355, Apr 1995.

[90] R. Ramírez, C. P. Herrero, and E. R. Hernández, "Path-integral molecular dynamics simulation of diamond," *Phys. Rev. B*, vol. 73, p. 245202, Jun 2006.

[91] M. A. Morales, J. M. McMahon, C. Pierleoni, and D. M. Ceperley, "Towards a predictive first-principles description of solid molecular hydrogen with density functional theory," *Phys. Rev. B*, vol. 87, p. 184107, May 2013.

[92] C. E. Patrick and F. Giustino, "Quantum nuclear dynamics in the photophysics of diamondoids," *Nat. Commun.*, vol. 4, no. 1, pp. 1–7, 2013.

[93] B. Monserrat, N. D. Drummond, C. J. Pickard, and R. J. Needs, "Electron–phonon coupling and the metallization of solid helium at terapascal pressures," *Phys. Rev. Lett.*, vol. 112, p. 055504, Feb 2014.

[94] S. Azadi, B. Monserrat, W. M. C. Foulkes, and R. J. Needs, "Dissociation of high-pressure solid molecular hydrogen: A quantum Monte Carlo and anharmonic vibrational study," *Phys. Rev. Lett.*, vol. 112, p. 165501, Apr 2014.

[95] M. Zacharias, C. E. Patrick, and F. Giustino, "Stochastic approach to phonon-assisted optical absorption," *Phys. Rev. Lett.*, vol. 115, p. 177401, Oct 2015.

[96] N. D. Drummond, B. Monserrat, J. H. Lloyd-Williams, P. L. Ríos, C. J. Pickard, and R. J. Needs, "Quantum Monte Carlo study of the phase diagram of solid molecular hydrogen at extreme pressures," *Nat. Commun.*, vol. 6, no. 1, 2015.

[97] B. Monserrat, E. A. Engel, and R. J. Needs, "Giant electron–phonon interactions in molecular crystals and the importance of nonquadratic coupling," *Phys. Rev. B*, vol. 92, p. 140302, Oct 2015.

[98] E. Mostaani, B. Monserrat, N. D. Drummond, and C. J. Lambert, "Quasiparticle and excitonic gaps of one-dimensional carbon chains," *Phys. Chem. Chem. Phys.*, vol. 18, pp. 14810–14821, 2016.

[99] B. Monserrat, "Correlation effects on electron–phonon coupling in semiconductors: Many-body theory along thermal lines," *Phys. Rev. B*, vol. 93, p. 100301, Mar 2016.

[100] B. Monserrat, "Vibrational averages along thermal lines," *Phys. Rev. B*, vol. 93, p. 014302, Jan 2016.

[101] M. Zacharias and F. Giustino, "One-shot calculation of temperature-dependent optical spectra and phonon-induced band-gap renormalization," *Phys. Rev. B*, vol. 94, p. 075125, Aug 2016.

[102] B. Monserrat, G. J. Conduit, and R. J. Needs, "Extracting semiconductor band gap zero-point corrections from experimental data," *Phys. Rev. B*, vol. 90, p. 184302, Nov 2014.

[103] F. Giustino, "Electron–phonon interactions from first principles," *Rev. Mod. Phys.*, vol. 89, p. 015003, Feb 2017.

[104] P. Han and G. Bester, "Band gap renormalization of diamondoids: vibrational coupling and excitonic effects," *New J. Phys.*, vol. 18, p. 113052, Nov 2016.

[105] E. A. Engel, B. Monserrat, and R. J. Needs, "Vibrational renormalisation of the electronic band gap in hexagonal and cubic ice," *J. Chem. Phys.*, vol. 143, no. 24, pp. 244708–244708, 2015.

[106] E. A. Engel, B. Monserrat, and R. J. Needs, "Vibrational effects on surface energies and band gaps in hexagonal and cubic ice," *J. Chem. Phys.*, vol. 145, no. 4, pp. 044703–044703, 2016.

[107] R. J. Hunt, B. Monserrat, V. Zólyomi, and N. D. Drummond, "Diffusion quantum Monte Carlo and GW study of the electronic properties of monolayer and bulk hexagonal boron nitride," *Phys. Rev. B*, vol. 101, p. 205115, May 2020.

[108] J. C. Grossman and L. Mitas, "Efficient quantum Monte Carlo energies for molecular dynamics simulations," *Phys. Rev. Lett.*, vol. 94, p. 056403, Feb 2005.

[109] S. Azadi, R. Singh, and T. D. Kühne, "Nuclear quantum effects induce metallization of dense solid molecular hydrogen," *J. Comput. Chem.*, vol. 39, no. 5, pp. 262–268, 2018.

[110] D. Ceperley, M. Dewing, and C. Pierleoni, *The Coupled Electronic-Ionic Monte Carlo Simulation Method*, pp. 473–500. Berlin, Heidelberg: Springer Berlin Heidelberg, 2002.

[111] C. Pierleoni and D. Ceperley, *The coupled electron-ion Monte Carlo method*, pp. 641–683. Lecture Notes in Physics, 2006.

[112] V. Gorelov, M. Holzmann, D. M. Ceperley, and C. Pierleoni, "Energy gap closure of crystalline molecular hydrogen with pressure," *Phys. Rev. Lett.*, vol. 124, p. 116401, Mar 2020.

[113] V. Gorelov, D. M. Ceperley, M. Holzmann, and C. Pierleoni, "Electronic energy gap closure and metal-insulator transition in dense liquid hydrogen," *Phys. Rev. B*, vol. 102, p. 195133, Nov 2020.

[114] V. Gorelov, D. M. Ceperley, M. Holzmann, and C. Pierleoni, "Electronic structure and optical properties of quantum crystals from first principles calculations in the Born-Oppenheimer approximation," *J. Chem. Phys.*, vol. 153, no. 23, p. 234117, 2020.

[115] A. A. Maradudin, E. W. Montroll, and G. H. Weiss, *Theory of lattice dynamics in the harmonic approximation.* Solid State Physics, Supplement 3, Academic Press, New York, 1963.

[116] M. T. Dove, *Introduction to Lattice Dynamics.* Cambridge Topics in Mineral Physics and Chemistry, Cambridge University Press, 1993.

[117] W. Shockley and J. Bardeen, "Energy bands and mobilities in monatomic semiconductors," *Phys. Rev.*, vol. 77, pp. 407–408, Feb 1950.

[118] M. Lax, "The Franck-Condon principle and its application to crystals," *J. Chem. Phys.*, vol. 20, no. 11, pp. 1752–1760, 1952.

[119] S. Johnsen, Z. Liu, J. A. Peters, J.-H. Song, S. Nguyen, C. D. Malliakas, H. Jin, A. J. Freeman, B. W. Wessels, and M. G. Kanatzidis, "Thallium chalcohalides for X-ray and γ-ray detection," *J. Am. Chem. Soc.*, vol. 133, no. 26, pp. 10030–10033, 2011.

[120] P. D. Antunez, J. J. Buckley, and R. L. Brutchey, "Tin and germanium monochalcogenide IV–VI semiconductor nanocrystals for use in solar cells," *Nanoscale*, vol. 3, pp. 2399–2411, 2011.

[121] H. Shi, W. Ming, and M.-H. Du, "Bismuth chalcohalides and oxyhalides as optoelectronic materials," *Phys. Rev. B*, vol. 93, p. 104108, Mar 2016.

[122] H. Brooks, "Theory of the electrical properties of germanium and silicon," vol. 7 of *Advances in Electronics and Electron Physics*, pp. 85–182, Academic Press, 1955.

[123] C. O. Almbladh, "Statistical mechanics of band states and impurity states in semiconductors," *J. Phys. C: Solid State Phys.*, vol. 14, pp. 4575–4601, Nov 1981.

[124] P. B. Allen and J. C. K. Hui, "Thermodynamics of solids: Corrections from electron–phonon interactions," *Z. Phys. B*, vol. 37, no. 1, pp. 33–38, 1980.

[125] G. E. P. Box and M. E. Muller, "A Note on the Generation of Random Normal Deviates," *Ann. Math. Statist.*, vol. 29, no. 2, pp. 610 – 611, 1958.

[126] T. Koopmans, "Über die zuordnung von wellenfunktionen und eigenwerten zu den einzelnen elektronen eines atoms," *Physica*, vol. 1, no. 1, pp. 104–113, 1934.

[127] W. Yang, A. J. Cohen, and P. Mori-Sánchez, "Derivative discontinuity, bandgap and lowest unoccupied molecular orbital in density functional theory," *J. Chem. Phys.*, vol. 136, no. 20, p. 204111, 2012.

[128] S. J. Clark, M. D. Segall, C. J. Pickard, P. J. Hasnip, M. I. J. Probert, K. Refson, and M. C. Payne, "First principles methods using CASTEP," *Z. Kristallogr.*, vol. 220, pp. 567–570, 2005.

[129] D. Vanderbilt, "Soft self-consistent pseudopotentials in a generalized eigenvalue formalism," *Phys. Rev. B*, vol. 41, pp. 7892–7895, Apr 1990.

[130] K. Kunc and R. M. Martin, "Ab initio force constants of GaAs: A new approach to calculation of phonons and dielectric properties," *Phys. Rev. Lett.*, vol. 48, pp. 406–409, Feb 1982.

[131] K. Refson, P. R. Tulip, and S. J. Clark, "Variational density-functional perturbation theory for dielectrics and lattice dynamics," *Phys. Rev. B*, vol. 73, p. 155114, Apr 2006.

[132] R. W. Lynch and H. G. Drickamer, "Effect of high pressure on the lattice parameters of diamond, graphite, and hexagonal boron nitride," *J. Chem. Phys.*, vol. 44, no. 1, pp. 181–184, 1966.

[133] M. Casula, "Beyond the locality approximation in the standard diffusion Monte Carlo method," *Phys. Rev. B*, vol. 74, p. 161102, Oct 2006.

[134] N. D. Drummond, R. J. Needs, A. Sorouri, and W. M. C. Foulkes, "Finite-size errors in continuum quantum Monte Carlo calculations," *Phys. Rev. B*, vol. 78, p. 125106, Sep 2008.

[135] Y. Yang, V. Gorelov, C. Pierleoni, D. M. Ceperley, and M. Holzmann, "Electronic band gaps from quantum Monte Carlo methods," *Phys. Rev. B*, vol. 101, p. 085115, Feb 2020.

[136] B. Monserrat, "Electron–phonon coupling from finite differences," *J. Phys. Condens. Mater.*, vol. 30, p. 083001, Feb 2018.

[137] J. P. Doering, "Low-energy electron-impact study of the first, second, and third triplet states of benzene," *J. Chem. Phys.*, vol. 51, no. 7, pp. 2866–2870, 1969.

[138] R. W. Godby, M. Schlüter, and L. J. Sham, "Self-energy operators and exchange-correlation potentials in semiconductors," *Phys. Rev. B*, vol. 37, pp. 10159–10175, Jun 1988.

[139] S. Wang, "Intrinsic molecular vibration and rigorous vibrational assignment of benzene by first-principles molecular dynamics," *Sci. Rep.*, vol. 10, no. 1, pp. 1–14, 2020.

[140] K. S. Novoselov, D. Jiang, F. Schedin, T. J. Booth, V. V. Khotkevich, S. V. Morozov, and A. K. Geim, "Two-dimensional atomic crystals," *Proc. Natl. Acad. Sci. U.S.A.*, vol. 102, no. 30, pp. 10451–10453, 2005.

[141] A. K. Geim and I. V. Grigorieva, "Van der Waals heterostructures," *Nature*, vol. 499, no. 7459, pp. 419–425, 2013.

[142] E. Wang, X. Lu, S. Ding, W. Yao, M. Yan, G. Wan, K. Deng, S. Wang, G. Chen, L. Ma, *et al.*, "Gaps induced by inversion symmetry breaking and second-generation Dirac cones in graphene/hexagonal boron nitride," *Nat. Phys.*, vol. 12, no. 12, pp. 1111–1115, 2016.

[143] C. R. Dean, A. F. Young, I. Meric, C. Lee, L. Wang, S. Sorgenfrei, K. Watanabe, T. Taniguchi, P. Kim, K. L. Shepard, and J. Hone, "Boron nitride substrates for high-quality graphene electronics.," *Nat. Nanotechnol.*, vol. 5, no. 10, pp. 722 – 726, 2010.

[144] G. L. Yu, R. V. Gorbachev, J. S. Tu, A. V. Kretinin, Y. Cao, R. Jalil, F. Withers, L. A. Ponomarenko, B. A. Piot, M. Potemski, D. C. Elias, X. Chen, K. Watanabe, T. Taniguchi, I. V. Grigorieva, K. S. Novoselov, V. I. Fal'ko, A. K. Geim, and A. Mishchenko, "Hierarchy of Hofstadter states and replica quantum hall ferromagnetism in graphene superlattices.," *Nat. Phys.*, vol. 10, no. 7, pp. 525 – 529, 2014.

[145] B. Hunt, J. D. Sanchez-Yamagishi, A. F. Young, M. Yankowitz, B. J. LeRoy, K. Watanabe, T. Taniguchi, P. Moon, M. Koshino, P. Jarillo-Herrero, and R. C. Ashoori, "Massive Dirac fermions and Hofstadter butterfly in a van der Waals heterostructure," *Science*, vol. 340, no. 6139, pp. 1427–1430, 2013.

[146] B. Arnaud, S. Lebègue, P. Rabiller, and M. Alouani, "Huge excitonic effects in layered hexagonal boron nitride," *Phys. Rev. Lett.*, vol. 96, p. 026402, Jan 2006.

[147] L. Wirtz, A. Marini, and A. Rubio, "Excitons in boron nitride nanotubes: Dimensionality effects," *Phys. Rev. Lett.*, vol. 96, p. 126104, Mar 2006.

[148] G. Cassabois, P. Valvin, and B. Gil, "Hexagonal boron nitride is an indirect bandgap semiconductor," *Nat. Photonics*, vol. 10, pp. 262–266, Apr 2016.

[149] C. Elias, P. Valvin, T. Pelini, A. Summerfield, C. J. Mellor, T. S. Cheng, L. Eaves, C. T. Foxon, P. H. Beton, S. V. Novikov, B. Gil, and G. Cassabois, "Direct band-gap crossover in epitaxial monolayer boron nitride," *Nat. Commun.*, vol. 10, p. 2639, Jun 2019.

[150] J. Zupan and D. Kolar, "Optical properties of graphite and boron nitride," *J. Phys. C: Solid State Phys.*, vol. 5, pp. 3097–3100, Oct 1972.

[151] L. G. Carpenter and P. J. Kirby, "The electrical resistivity of boron nitride over the temperature range 700 degrees C to 1400 degrees C," *J. Phys. D: Appl. Phys.*, vol. 15, pp. 1143–1151, Jul 1982.

[152] D. M. Hoffman, G. L. Doll, and P. C. Eklund, "Optical properties of pyrolytic boron nitride in the energy range 0.05–10 eV," *Phys. Rev. B*, vol. 30, pp. 6051–6056, Nov 1984.

[153] K. Watanabe, T. Taniguchi, and H. Kanda, "Direct-bandgap properties and evidence for ultraviolet lasing of hexagonal boron nitride single crystal," *Nat. Mater.*, vol. 3, pp. 404–409, Jun 2004.

[154] P. Kumbhakar, A. K. Kole, C. S. Tiwary, S. Biswas, S. Vinod, J. Taha-Tijerina, U. Chatterjee, and P. M. Ajayan, "Nonlinear optical properties and temperature-dependent UV-Vis absorption and photoluminescence emission in 2D hexagonal boron nitride nanosheets," *Adv. Opt. Mater.*, vol. 3, no. 6, pp. 828–835, 2015.

[155] T. Shen, X.-W. Zhang, H. Shang, M.-Y. Zhang, X. Wang, E.-G. Wang, H. Jiang, and X.-Z. Li, "Influence of high-energy local orbitals and electron–phonon interactions on the band gaps and optical absorption spectra of hexagonal boron nitride," *Phys. Rev. B*, vol. 102, p. 045117, Jul 2020.

[156] V. Zólyomi, N. D. Drummond, and V. I. Fal'ko, "Electrons and phonons in single layers of hexagonal indium chalcogenides from ab initio calculations.," *Phys. Rev. B*, vol. 89, no. 20, pp. 205416–1 – 205416–8, 2014.

[157] R. J. P. Román, F. J. R. C. Costa, A. Zobelli, C. Elias, P. Valvin, G. Cassabois, B. Gil, A. Summerfield, T. S. Cheng, C. J. Mellor, P. H. Beton, S. V. Novikov, and L. F. Zagonel, "Band gap measurements of monolayer h-BN and insights into carbon-related point defects," *2D Mater.*, vol. 8, p. 044001, Jul 2021.

[158] W. Bludau, A. Onton, and W. Heinke, "Temperature dependence of the band gap of silicon," *J. Appl. Phys.*, vol. 45, no. 4, pp. 1846–1848, 1974.

[159] K. P. O'Donnell and X. Chen, "Temperature dependence of semiconductor band gaps," *Appl. Phys. Lett.*, vol. 58, no. 25, pp. 2924–2926, 1991.

[160] M. Cardona and M. L. W. Thewalt, "Isotope effects on the optical spectra of semiconductors," *Rev. Mod. Phys.*, vol. 77, pp. 1173–1224, Nov 2005.

[161] S. B. Cronin, Y. Yin, A. Walsh, R. B. Capaz, A. Stolyarov, P. Tangney, M. L. Cohen, S. G. Louie, A. K. Swan, M. S. Ünlü, B. B. Goldberg, and M. Tinkham, "Temperature dependence of the optical transition energies of carbon nanotubes: The role of electron–phonon coupling and thermal expansion," *Phys. Rev. Lett.*, vol. 96, p. 127403, Mar 2006.

[162] S. V. Faleev, M. van Schilfgaarde, and T. Kotani, "All-electron self-consistent GW approximation: Application to Si, MnO, and NiO," *Phys. Rev. Lett.*, vol. 93, p. 126406, Sep 2004.

[163] J. Derr, K. Dunn, D. Riabinina, F. Martin, M. Chaker, and F. Rosei, "Quantum confinement regime in silicon nanocrystals," *Phys. E: Low-Dimensional Syst. Nanostructures*, vol. 41, no. 4, pp. 668–670, 2009.

[164] A. M. Hartel, S. Gutsch, D. Hiller, and M. Zacharias, "Fundamental temperature-dependent properties of the Si nanocrystal band gap," *Phys. Rev. B*, vol. 85, p. 165306, Apr 2012.

[165] K. Ishii, J. Haruyama, and O. Sugino, "Optical representation of thermal nuclear fluctuation effect on band-gap renormalization," *Phys. Rev. B*, vol. 104, p. 245144, Dec 2021.

[166] T. Zhu, G. Yu, J. Xu, H. Wu, C. Fu, X. Liu, J. He, and X. Zhao, "The role of electron–phonon interaction in heavily doped fine-grained bulk silicons as thermoelectric materials," *Adv. Electron. Mater.*, vol. 2, no. 8, p. 1600171, 2016.

[167] Y. Quan, S. Yue, and B. Liao, "Impact of electron–phonon interaction on thermal transport: A review," *Nanoscale. Microscale. Thermophys. Eng.*, vol. 25, no. 2, pp. 73–90, 2021.

[168] M. Cardona, T. A. Meyer, and M. L. W. Thewalt, "Temperature dependence of the energy gap of semiconductors in the low-temperature limit," *Phys. Rev. Lett.*, vol. 92, p. 196403, May 2004.

[169] M. D. Towler, R. Q. Hood, and R. J. Needs, "Minimum principles and level splitting in quantum Monte Carlo excitation energies: Application to diamond," *Phys. Rev. B*, vol. 62, pp. 2330–2337, Jul 2000.

[170] X. Blase, A. Rubio, S. G. Louie, and M. L. Cohen, "Quasiparticle band structure of bulk hexagonal boron nitride and related systems," *Phys. Rev. B*, vol. 51, pp. 6868–6875, Mar 1995.

[171] P. Cudazzo, L. Sponza, C. Giorgetti, L. Reining, F. Sottile, and M. Gatti, "Exciton band structure in two-dimensional materials," *Phys. Rev. Lett.*, vol. 116, p. 066803, Feb 2016.

[172] D. Y. Qiu, F. H. da Jornada, and S. G. Louie, "Optical spectrum of MoS_2: Many-body effects and diversity of exciton states," *Phys. Rev. Lett.*, vol. 111, p. 216805, Nov 2013.

[173] V. Huard, R. T. Cox, K. Saminadayar, A. Arnoult, and S. Tatarenko, "Bound states in optical absorption of semiconductor quantum wells containing a two-dimensional electron gas," *Phys. Rev. Lett.*, vol. 84, pp. 187–190, Jan 2000.

[174] A. Splendiani, L. Sun, Y. Zhang, T. Li, J. Kim, C.-Y. Chim, G. Galli, and F. Wang, "Emerging photoluminescence in monolayer MoS_2," *Nano Lett.*, vol. 10, no. 4, pp. 1271–1275, 2010.

[175] Q. H. Wang, K. Kalantar-Zadeh, A. Kis, J. N. Coleman, and M. S. Strano, "Electronics and optoelectronics of two-dimensional transition metal dichalcogenides.," *Nat. Nanotechnol*, vol. 7, no. 11, pp. 699 – 712, 2012.

[176] X. Xu, W. Yao, D. Xiao, and T. F. Heinz, "Spin and pseudospins in layered transition metal dichalcogenides.," *Nat. Phys.*, vol. 10, no. 5, pp. 343 – 350, 2014.

[177] G. Sallen, L. Bouet, X. Marie, G. Wang, C. R. Zhu, W. P. Han, Y. Lu, P. H. Tan, T. Amand, B. L. Liu, and B. Urbaszek, "Robust optical emission

polarization in MoS_2 monolayers through selective valley excitation," *Phys. Rev. B*, vol. 86, p. 081301, Aug 2012.

[178] A. Srivastava, M. Sidler, A. V. Allain, D. S. Lembke, A. Kis, and A. Imamoğlu, "Valley zeeman effect in elementary optical excitations of monolayer WSe2," *Nat. Phys.*, vol. 11, pp. 141–147, Jan 2015.

[179] C. Zhang, H. Wang, W. Chan, C. Manolatou, and F. Rana, "Absorption of light by excitons and trions in monolayers of metal dichalcogenide MoS_2: Experiments and theory," *Phys. Rev. B*, vol. 89, p. 205436, May 2014.

[180] K. F. Mak, K. He, C. Lee, G. H. Lee, J. Hone, T. F. Heinz, and J. Shan, "Tightly bound trions in monolayer MoS_2.," *Nat. Mater.*, vol. 12, no. 3, pp. 207 – 211, 2013.

[181] I. Kylänpää and H.-P. Komsa, "Binding energies of exciton complexes in transition metal dichalcogenide monolayers and effect of dielectric environment," *Phys. Rev. B*, vol. 92, p. 205418, Nov 2015.

[182] B. Ganchev, N. Drummond, I. Aleiner, and V. Fal'ko, "Three-particle complexes in two-dimensional semiconductors," *Phys. Rev. Lett.*, vol. 114, p. 107401, Mar 2015.

[183] M. Z. Mayers, T. C. Berkelbach, M. S. Hybertsen, and D. R. Reichman, "Binding energies and spatial structures of small carrier complexes in monolayer transition-metal dichalcogenides via diffusion Monte Carlo," *Phys. Rev. B*, vol. 92, p. 161404, Oct 2015.

[184] T. C. Berkelbach, M. S. Hybertsen, and D. R. Reichman, "Theory of neutral and charged excitons in monolayer transition metal dichalcogenides," *Phys. Rev. B*, vol. 88, p. 045318, Jul 2013.

[185] E. Mostaani, M. Szyniszewski, C. H. Price, R. Maezono, M. Danovich, R. J. Hunt, N. D. Drummond, and V. I. Fal'ko, "Diffusion quantum Monte Carlo study of excitonic complexes in two-dimensional transition-metal dichalcogenides," *Phys. Rev. B*, vol. 96, p. 075431, Aug 2017.

[186] M. Szyniszewski, E. Mostaani, N. D. Drummond, and V. I. Fal'ko, "Binding energies of trions and biexcitons in two-dimensional semiconductors from diffusion quantum Monte Carlo calculations," *Phys. Rev. B*, vol. 95, p. 081301, Feb 2017.

[187] J. S. Ross, P. Klement, A. M. Jones, N. J. Ghimire, J. Yan, D. G. Mandrus, T. Taniguchi, K. Watanabe, K. Kitamura, W. Yao, D. H. Cobden, and X. Xu, "Electrically tunable excitonic light-emitting diodes based on monolayer WSe_2 p-n junctions.," *Nat. Nanotechnol*, vol. 9, no. 4, pp. 268 – 272, 2014.

[188] C. H. Lui, A. J. Frenzel, D. V. Pilon, Y.-H. Lee, X. Ling, G. M. Akselrod, J. Kong, and N. Gedik, "Trion-induced negative photoconductivity in monolayer MoS_2," *Phys. Rev. Lett.*, vol. 113, p. 166801, Oct 2014.

[189] N. Scheuschner, O. Ochedowski, A.-M. Kaulitz, R. Gillen, M. Schleberger, and J. Maultzsch, "Photoluminescence of freestanding single- and few-layer MoS_2," *Phys. Rev. B*, vol. 89, p. 125406, Mar 2014.

[190] Y. Zhang, H. Li, H. Wang, R. Liu, S.-L. Zhang, and Z.-J. Qiu, "On valence-band splitting in layered MoS_2," *ACS Nano*, vol. 9, no. 8, pp. 8514–8519, 2015.

[191] M. Zinkiewicz, T. Woźniak, T. Kazimierczuk, P. Kapuscinski, K. Oreszczuk, M. Grzeszczyk, M. Bartoš, K. Nogajewski, K. Watanabe, T. Taniguchi, C. Faugeras, P. Kossacki, M. Potemski, A. Babiński, and M. R. Molas, "Excitonic complexes in n-doped WS_2 monolayer," *Nano Lett.*, vol. 21, no. 6, pp. 2519–2525, 2021.

[192] M. Yang, L. Ren, C. Robert, D. Van Tuan, L. Lombez, B. Urbaszek, X. Marie, and H. Dery, "Relaxation and darkening of excitonic complexes in electrostatically doped monolayer WSe_2: Roles of exciton-electron and trion-electron interactions," *Phys. Rev. B*, vol. 105, p. 085302, Feb 2022.

[193] O. A. Ajayi, J. V. Ardelean, G. D. Shepard, J. Wang, A. Antony, T. Taniguchi, K. Watanabe, T. F. Heinz, S. Strauf, X.-Y. Zhu, and J. C. Hone, "Approaching the intrinsic photoluminescence linewidth in transition metal dichalcogenide monolayers," *2D Mater.*, vol. 4, p. 031011, Jul 2017.

[194] F. Cadiz, E. Courtade, C. Robert, G. Wang, Y. Shen, H. Cai, T. Taniguchi, K. Watanabe, H. Carrere, D. Lagarde, M. Manca, T. Amand, P. Renucci, S. Tongay, X. Marie, and B. Urbaszek, "Excitonic linewidth approaching the homogeneous limit in MoS_2-based van der Waals heterostructures," *Phys. Rev. X*, vol. 7, p. 021026, May 2017.

[195] E. Courtade, M. Semina, M. Manca, M. M. Glazov, C. Robert, F. Cadiz, G. Wang, T. Taniguchi, K. Watanabe, M. Pierre, W. Escoffier, E. L. Ivchenko, P. Renucci, X. Marie, T. Amand, and B. Urbaszek, "Charged excitons in monolayer WSe_2: Experiment and theory," *Phys. Rev. B*, vol. 96, p. 085302, Aug 2017.

[196] S. Latini, T. Olsen, and K. S. Thygesen, "Excitons in van der Waals heterostructures: The important role of dielectric screening," *Phys. Rev. B*, vol. 92, p. 245123, Dec 2015.

[197] A. Raja, L. Waldecker, J. Zipfel, Y. Cho, S. Brem, J. D. Ziegler, M. Kulig, T. Taniguchi, K. Watanabe, E. Malic, T. F. Heinz, T. C. Berkelbach, and A. Chernikov, "Dielectric disorder in two-dimensional materials," *Nat. Nanotechnol*, vol. 14, no. 9, pp. 832–837, 2019.

[198] N. S. Rytova, "Coulomb interaction of electrons in a thin film," *Dokl. Akad. Nauk. SSSR*, vol. 163, pp. 1118–1120, 1965.

[199] N. S. Rytova, "Screened potential of a point charge in the thin film," *Vestn. Mosk. Univ. Fiz. Astron.*, vol. 3, pp. 30–37, 1967.

[200] L. V. Keldysh, "Coulomb interaction in thin semiconductor and semimetal films," *J. Exp. Theor. Phys.*, vol. 29, no. 11, p. 658, 1979.

[201] K. A. Velizhanin and A. Saxena, "Excitonic effects in two-dimensional semiconductors: Path integral Monte Carlo approach," *Phys. Rev. B*, vol. 92, p. 195305, Nov 2015.

[202] P. P. Ewald, "Die berechnung optischer und elektrostatischer gitterpotentiale," *Annalen der Physik*, vol. 369, no. 3, pp. 253–287, 1921.

[203] D. Parry, "The electrostatic potential in the surface region of an ionic crystal," *Surf. Sci.*, vol. 49, no. 2, pp. 433–440, 1975.

[204] H. Shi, H. Pan, Y.-W. Zhang, and B. I. Yakobson, "Quasiparticle band structures and optical properties of strained monolayer MoS_2 and WS_2," *Phys. Rev. B*, vol. 87, p. 155304, Apr 2013.

[205] A. Kumar and P. Ahluwalia, "Tunable dielectric response of transition metals dichalcogenides MX2 (M=Mo, W; X=S, Se, Te): Effect of quantum confinement," *Phys. B*, vol. 407, no. 24, pp. 4627–4634, 2012.

[206] R. Geick, C. H. Perry, and G. Rupprecht, "Normal modes in hexagonal boron nitride," *Phys. Rev.*, vol. 146, pp. 543–547, Jun 1966.

[207] N. D. Drummond, P. López Ríos, R. J. Needs, and C. J. Pickard, "Quantum Monte Carlo study of a Positron in an electron gas," *Phys. Rev. Lett.*, vol. 107, p. 207402, Nov 2011.

[208] G. G. Spink, R. J. Needs, and N. D. Drummond, "Quantum Monte Carlo study of the three-dimensional spin-polarized homogeneous electron gas," *Phys. Rev. B*, vol. 88, p. 085121, Aug 2013.

[209] S. A. Bonev and N. W. Ashcroft, "Hydrogen in jellium: First-principles pair interactions," *Phys. Rev. B*, vol. 64, p. 224112, Nov 2001.

[210] N. D. Drummond, P. López Ríos, C. J. Pickard, and R. J. Needs, "First-principles method for impurities in quantum fluids: Positron in an electron gas," *Phys. Rev. B*, vol. 82, p. 035107, Jul 2010.

[211] M. Ernzerhof, J. P. Perdew, and K. Burke, *Density functionals: Where do they come from, why do they work?*, pp. 1–30. Berlin, Heidelberg: Springer Berlin Heidelberg, 1996.

[212] K. Burke, J. P. Perdew, and M. Ernzerhof, "Why semilocal functionals work: Accuracy of the on-top pair density and importance of system averaging," *J. Chem. Phys.*, vol. 109, no. 10, pp. 3760–3771, 1998.

[213] D. M. Thomas, Y. Asiri, and N. D. Drummond, "Point defect formation energies in graphene from diffusion quantum Monte Carlo and density functional theory," *Phys. Rev. B*, vol. 105, p. 184114, May 2022.

[214] K. S. Novoselov, A. K. Geim, S. V. Morozov, D. Jiang, Y. Zhang, S. V. Dubonos, I. V. Grigorieva, and A. A. Firsov, "Electric field effect in atomically thin carbon films," *Science*, vol. 306, no. 5696, pp. 666–669, 2004.

[215] A. H. Castro Neto, F. Guinea, N. M. R. Peres, K. S. Novoselov, and A. K. Geim, "The electronic properties of graphene," *Rev. Mod. Phys.*, vol. 81, pp. 109–162, Jan 2009.

[216] S. Das Sarma, S. Adam, E. H. Hwang, and E. Rossi, "Electronic transport in two-dimensional graphene," *Rev. Mod. Phys.*, vol. 83, pp. 407–470, May 2011.

[217] R. Muñoz and C. Gómez-Aleixandre, "Review of CVD synthesis of graphene," *Chem. Vap. Depos.*, vol. 19, no. 10-11-12, pp. 297–322, 2013.

[218] L. Vicarelli, S. J. Heerema, C. Dekker, and H. W. Zandbergen, "Controlling defects in graphene for optimizing the electrical properties of graphene nanodevices," *ACS Nano*, vol. 9, no. 4, pp. 3428–3435, 2015.

[219] P. Y. Huang, J. C. Meyer, and D. A. Muller, "From atoms to grains: Transmission electron microscopy of graphene," *MRS bulletin*, vol. 37, no. 12, pp. 1214–1221, 2012.

[220] S. J. Zhang, S. S. Lin, X. Q. Li, X. Y. Liu, H. A. Wu, W. L. Xu, P. Wang, Z. Q. Wu, H. K. Zhong, and Z. J. Xu, "Opening the band gap of graphene through silicon doping for the improved performance of graphene/GaAs heterojunction solar cells," *Nanoscale*, vol. 8, pp. 226–232, 2016.

[221] A. Hashimoto, K. Suenaga, A. Gloter, K. Urita, and S. Iijima, "Direct evidence for atomic defects in graphene layers," *Nature*, vol. 430, pp. 870–873, Aug 2004.

[222] A. W. Robertson and J. H. Warner, "Atomic resolution imaging of graphene by transmission electron microscopy," *Nanoscale*, vol. 5, pp. 4079–4093, 2013.

[223] M. T. Lusk and L. D. Carr, "Nanoengineering defect structures on graphene," *Phys. Rev. Lett.*, vol. 100, p. 175503, Apr 2008.

[224] G. M. Yang, H. Z. Zhang, X. F. Fan, and W. T. Zheng, "Density functional theory calculations for the quantum capacitance performance of graphene-based electrode material," *J. Phys. Chem. C*, vol. 119, no. 12, pp. 6464–6470, 2015.

[225] Y. Okamoto, "Density functional theory calculations of lithium adsorption and insertion to defect-free and defective graphene," *J. Phys. Chem. C*, vol. 120, no. 26, pp. 14009–14014, 2016.

[226] E. Kaxiras and K. C. Pandey, "Energetics of defects and diffusion mechanisms in graphite," *Phys. Rev. Lett.*, vol. 61, pp. 2693–2696, Dec 1988.

[227] A. A. El-Barbary, R. H. Telling, C. P. Ewels, M. I. Heggie, and P. R. Briddon, "Structure and energetics of the vacancy in graphite," *Phys. Rev. B*, vol. 68, p. 144107, Oct 2003.

[228] S. Azevedo, J. R. Kaschny, C. M. C. de Castilho, and F. de Brito Mota, "A theoretical investigation of defects in a boron nitride monolayer," *Nanotechnology*, vol. 18, p. 495707, Nov 2007.

[229] J. R. Reimers, A. Sajid, R. Kobayashi, and M. J. Ford, "Understanding and calibrating density-functional-theory calculations describing the energy and spectroscopy of defect sites in hexagonal boron nitride," *J. Chem. Theory Comput.*, vol. 14, no. 3, pp. 1602–1613, 2018.

[230] W. H. Blades, N. J. Frady, P. M. Litwin, S. J. McDonnell, and P. Reinke, "Thermally induced defects on WSe_2," *J. Phys. Chem. C*, vol. 124, no. 28, pp. 15337–15346, 2020.

[231] F. Banhart, J. Kotakoski, and A. V. Krasheninnikov, "Structural defects in graphene," *ACS Nano*, vol. 5, pp. 26–41, Jan 2011.

[232] J. D. Wadey, A. Markevich, A. Robertson, J. Warner, A. Kirkland, and E. Besley, "Mechanisms of monovacancy diffusion in graphene," *Chem. Phys. Lett.*, vol. 648, pp. 161 – 165, 2016.

[233] C. Lijie, S. Li, C. Jin, D. Jariwala, W. Dangxin, L. Yongjie, A. Srivastava, Z. F. Wang, K. Storr, L. Balicas, L. Feng, and P. M. Ajayan, "Atomic layers of hybridized boron nitride and graphene domains.," *Nat. Mater.*, vol. 9, no. 5, pp. 430 – 435, 2010.

[234] P. Lazar, R. Zbořil, M. Pumera, and M. Otyepka, "Chemical nature of boron and nitrogen dopant atoms in graphene strongly influences its electronic properties," *Phys. Chem. Chem. Phys.*, vol. 16, pp. 14231–14235, 2014.

[235] P. Rani and V. K. Jindal, "Stability and electronic properties of isomers of B/N co-doped graphene," *Appl. Nanosci.*, vol. 4, no. 8, pp. 989–996, 2014.

[236] A. Kheyri, Z. Nourbakhsh, and E. Darabi, "The electronic and magnetic properties and the topological phase graphene sheet with Fe, Co, Si, and Ge impurities.," *J. Supercond. Nov. Magn.*, vol. 29, no. 4, pp. 985 – 993, 2016.

[237] M. M. Ervasti, Z. Fan, A. Uppstu, A. V. Krasheninnikov, and A. Harju, "Silicon and silicon-nitrogen impurities in graphene: Structure, energetics, and effects on electronic transport," *Phys. Rev. B*, vol. 92, p. 235412, Dec 2015.

[238] J. Kang, J. Bang, B. Ryu, and K. J. Chang, "Effect of atomic-scale defects on the low-energy electronic structure of graphene: Perturbation theory and local-density-functional calculations," *Phys. Rev. B*, vol. 77, p. 115453, Mar 2008.

[239] A. Podlivaev and L. Openov, "Out-of-plane path of the Stone-Wales transformation in graphene," *Phys. Lett. A*, vol. 379, no. 30, pp. 1757–1761, 2015.

[240] J. M. Carlsson and M. Scheffler, "Structural, electronic, and chemical properties of nanoporous carbon," *Phys. Rev. Lett.*, vol. 96, p. 046806, Feb 2006.

[241] D. W. Boukhvalov and M. I. Katsnelson, "Chemical functionalization of graphene with defects," *Nano Lett.*, vol. 8, pp. 4373–4379, Dec 2008.

[242] A. Juneja and G. Rajasekaran, "Anomalous strength characteristics of Stone-Thrower-Wales defects in graphene sheets-a molecular dynamics study," *Phys. Chem. Chem. Phys.*, vol. 20, no. 22, pp. 15203–15215, 2018.

[243] T. C. Sagar, V. Chinthapenta, and M. F. Horstemeyer, "Effect of defect guided out-of-plane deformations on the mechanical properties of graphene," *Fuller. Nanotub. Carbon Nanostructures*, vol. 29, no. 2, pp. 83–99, 2021.

[244] L. A. Openov and A. I. Podlivaev, "Interaction of the Stone-Wales defects in graphene," *Phys. Solid State*, vol. 57, pp. 1477–1481, Jul 2015.

[245] A. I. Podlivaev and L. A. Openov, "Attraction between topological defects in graphene," *JETP Lett.*, vol. 101, pp. 173–176, Feb 2015.

[246] K. V. Zakharchenko, A. Fasolino, J. H. Los, and M. I. Katsnelson, "Melting of graphene: from two to one dimension," *J. Phys. Condens. Mater.*, vol. 23, p. 202202, May 2011.

[247] S. T. Skowron, I. V. Lebedeva, A. M. Popov, and E. Bichoutskaia, "Energetics of atomic scale structure changes in graphene," *Chem. Soc. Rev.*, vol. 44, no. 1, pp. 3143–3176, 2015.

[248] H. J. Monkhorst and J. D. Pack, "Special points for brillouin-zone integrations," *Phys. Rev. B*, vol. 13, pp. 5188–5192, Jun 1976.

[249] G. H. Vineyard, "Frequency factors and isotope effects in solid state rate processes," *J. Phys. Chem. Solids*, vol. 3, no. 1, pp. 121–127, 1957.

[250] B. T. Kelly, *Physics of graphite*. Applied Science, 1981.

[251] M. S. Dresselhaus, G. Dresselhaus, K. Sugihara, I. L. Spain, and H. A. Goldberg, *Graphite Fibers and Filaments*. Springer-Verlag, 1988.

[252] N. Govind, M. Petersen, G. Fitzgerald, D. King-Smith, and J. Andzelm, "A generalized synchronous transit method for transition state location," *Comput. Mater. Sci.*, vol. 28, no. 2, pp. 250–258, 2003.

[253] G. Henkelman and H. Jónsson, "Improved tangent estimate in the nudged elastic band method for finding minimum energy paths and saddle points," *J. Chem. Phys.*, vol. 113, no. 22, pp. 9978–9985, 2000.

[254] D. Alfè and M. J. Gillan, "Efficient localized basis set for quantum Monte Carlo calculations on condensed matter," *Phys. Rev. B*, vol. 70, p. 161101, October 2004.

[255] C. W. M. Castleton and S. Mirbt, "Finite-size scaling as a cure for supercell approximation errors in calculations of neutral native defects in InP," *Phys. Rev. B*, vol. 70, p. 195202, Nov 2004.

[256] L. M. Fraser, W. M. C. Foulkes, G. Rajagopal, R. J. Needs, S. D. Kenny, and A. J. Williamson, "Finite-size effects and Coulomb interactions in quantum Monte Carlo calculations for homogeneous systems with periodic boundary conditions," *Phys. Rev. B*, vol. 53, no. 4, p. 1814, 1996.

[257] S. Chiesa, D. M. Ceperley, R. M. Martin, and M. Holzmann, "Finite-size error in many-body simulations with long-range interactions," *Phys. Rev. Lett.*, vol. 97, p. 076404, Aug 2006.

[258] C. Guedj, L. Jaillet, F. Rousse, and S. Redon, "Atomistic modelling and simulation of transmission electron microscopy images: Application to intrinsic defects of graphene," in *International Conference on Simulation and Modeling Methodologies, Technologies and Applications*, pp. 1–19, Springer, 2018.

[259] J. Ma, D. Alfè, A. Michaelides, and E. Wang, "Stone-Wales defects in graphene and other planar sp^2-bonded materials," *Phys. Rev. B*, vol. 80, p. 033407, Jul 2009.

[260] P. A. Denis, "Band gap opening of monolayer and bilayer graphene doped with aluminium, silicon, phosphorus, and sulfur," *Chem. Phys. Lett.*, vol. 492, p. 251, 2010.

[261] S. N. Shirodkar and U. V. Waghmare, "Electronic and vibrational signatures of Stone-Wales defects in graphene: First-principles analysis," *Phys. Rev. B*, vol. 86, p. 165401, Oct 2012.

[262] A. Zobelli, V. Ivanovskaya, P. Wagner, I. Suarez-Martinez, A. Yaya, and C. P. Ewels, "A comparative study of density functional and density functional tight binding calculations of defects in graphene," *Phys. Status Solidi B*, vol. 249, no. 2, pp. 276–282, 2012.

[263] N. J. Roome and J. D. Carey, "Beyond graphene: Stable elemental monolayers of silicene and germanene," *ACS Appl. Mater. Interfaces*, vol. 6, pp. 7743–7750, May 2014.

[264] S. Cahangirov, M. Topsakal, E. Aktürk, H. Şahin, and S. Ciraci, "Two-and one-dimensional honeycomb structures of silicon and germanium," *Phys. Rev. Lett.*, vol. 102, p. 236804, Jun 2009.

[265] P. Vogt, P. De Padova, C. Quaresima, J. Avila, E. Frantzeskakis, M. C. Asensio, A. Resta, B. Ealet, and G. Le Lay, "Silicene: Compelling experimental evidence for graphenelike two-dimensional silicon," *Phys. Rev. Lett.*, vol. 108, p. 155501, Apr 2012.

[266] E. Cinquanta, E. Scalise, D. Chiappe, C. Grazianetti, B. van den Broek, M. Houssa, M. Fanciulli, and A. Molle, "Getting through the nature of silicene: An sp^2-sp^3 two-dimensional silicon nanosheet," *J. Phys. Chem. C*, vol. 117, pp. 16719–16724, Aug 2013.

[267] L. Meng, Y. Wang, L. Zhang, S. Du, R. Wu, L. Li, Y. Zhang, G. Li, H. Zhou, W. A. Hofer, and H.-J. Gao, "Buckled silicene formation on Ir(111)," *Nano Lett.*, vol. 13, no. 2, pp. 685–690, 2013.

[268] D. Alfè, M. J. Gillan, M. D. Towler, and R. J. Needs, "Diamond and β-tin structures of Si studied with quantum Monte Carlo calculations," *Phys. Rev. B*, vol. 70, p. 214102, Dec 2004.

[269] X.-P. Li, D. M. Ceperley, and R. M. Martin, "Cohesive energy of silicon by the Green's-function Monte Carlo method," *Phys. Rev. B*, vol. 44, pp. 10929–10932, Nov 1991.

[270] W.-K. Leung, R. J. Needs, G. Rajagopal, S. Itoh, and S. Ihara, "Calculations

of silicon self-interstitial defects," *Phys. Rev. Lett.*, vol. 83, pp. 2351–2354, Sep 1999.

[271] "NIST-JANAF thermochemical tables." `https://janaf.nist.gov/tables/Si-index.html`, 1985.

[272] B. Farid and R. W. Godby, "Cohesive energies of crystals," *Phys. Rev. B*, vol. 43, pp. 14248–14250, Jun 1991.